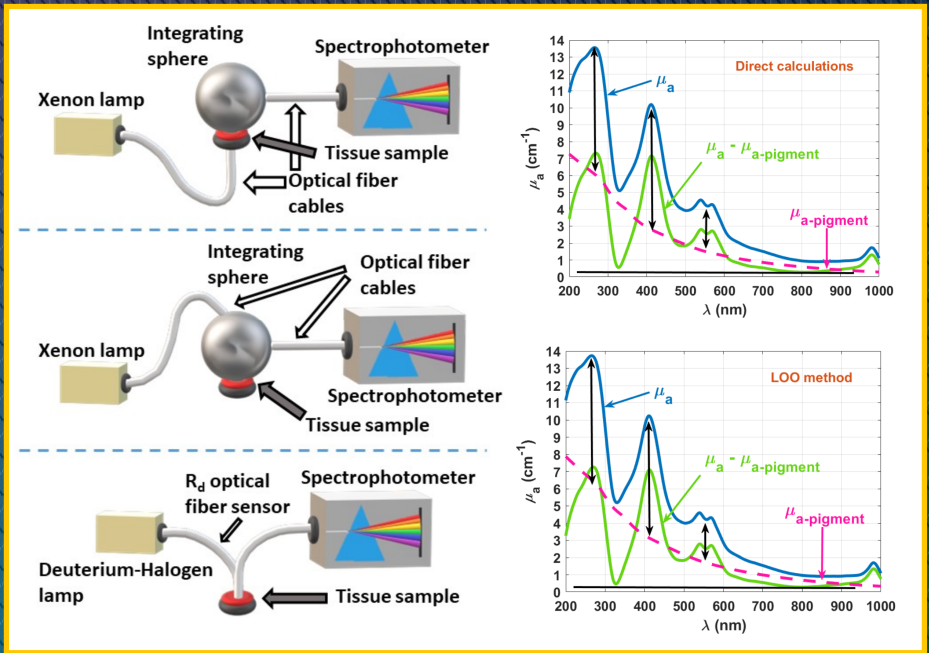
Volume 8, Issue 1, 2022

Journal of Biomedical Photonics & Engineering

Special Issue
"Biophotonics Technologies (dedicated to the memory of Dr. Alexey N. Bashkatov)"



Special issue Editors:
Ivan A. Bratchenko, Luís Oliveira, Elina A. Genina

© 2022 J-BPE

Journal of Biomedical Photonics & Engineering
by Samara National Research University

Volume 8, Issue 1 (March 2022)

Special Issue "Biophotonics Technologies (dedicated to the memory of Dr. Alexey N. Bashkatov)"

Special Issue Editors

Ivan A. Bratchenko
Samara National Research University, Russia

Luís Oliveira
Polytechnic of Porto, Portugal

Elina A. Genina
Saratov State University, Russia

Valery P. Zakharov
Samara National Research University, Russia

Valery V. Tuchin
Saratov State University, Russia
National Research Tomsk State University, Russia
Institute of Precision Mechanics and Control of the RAS, Saratov, Russia

© 2022 J-BPE

Editor-In-Chief

Valery V. Tuchin - Saratov National Research State University, Russian Federation;
Institute of Precision Mechanics and Control RAS, Russian Federation; a corr.-member of RAS

Deputy Editor-In-Chief

Valery P. Zakharov - Samara National Research University, Russian Federation

Postal address:
39B Lukacheva st., room #301
Samara 443086, Russian Federation

Used Figure from this issue on the Cover

Luís R. Oliveira et al. Invasive and minimally invasive optical detection of pigment accumulation in brain cortex, 010304, Figs. 1 and 11.

© 2022 J-BPE

Contents

Introduction

Foreword to Biophotonics Technologies (dedicated to the memory of Dr. Alexey N. Bashkatov) 010101

Review

Types of Optical Coherence Tomography for Cancer Diagnosis: A Systematic Review 010201
Neha Acharya, Sindhoora K. Melanthota, Manoj Khokhar, Shweta Chakrabarti, Dharshini Gopal, Dhyeya S. Mallya, and Nirmal Mazumder

Articles

Silver Nanoparticles-Based Substrate for Blood Serum Analysis under 785 nm Laser Excitation 010301
Sahar Z. Al-Sammarraie, Lyudmila A. Bratchenko, Elena N. Typikova, Peter A. Lebedev, Valery P. Zakharov, and Ivan A. Bratchenko

Mathematical Modelling of the Influence of Different Concentrations of Oxaloacetate to Glycerol-3-Phosphate Dehydrogenase Structure 010302
Nataliya A. Kolotyeva, Frida N. Gilmiyarova, Oksana A. Gusyakova, Marina V. Komarova, Nikita V. Remizov, and Elena A. Ryskina

Endofluorescence Imaging of Murine Hepatocellular Carcinoma Cell Culture by Fluorescence Lifetime Microscopy with Modulated CMOS Camera 010303
Elena Potapova, Evgeny Zherebtsov, Ksenia Kandurova, Alexander Palalov, Viktor Dremin, and Andrey Dunaev

Invasive and minimally invasive optical detection of pigment accumulation in brain cortex 010304
Luís R. Oliveira, Tânia M. Gonçalves, Maria R. Pinheiro, Luís E. Fernandes, Inês S. Martins, Hugo F. Silva, Hélder P. Oliveira, Valery V. Tuchin, and Luís M. Oliveira

Theoretical and Experimental Study of the Water-Based Drug Delivery under the Nail Plate by Er-Laser Radiation 010305
Andrey V. Belikov, Anastasia D. Kozlova, and Sergey N. Smirnov

 © 2022 J-BPE

 doi: 10.18287/JBPE21.08.010101

Foreword to Biophotonics Technologies (dedicated to the memory of Dr. Alexey N. Bashkatov)

Dear Colleagues,

This special issue is dedicated to a brilliant scientist Associate Professor of the Department of Optics and Biophotonics of Saratov State University, **Dr. Alexey N. Bashkatov**. Regretfully, because of his sudden demise, Alexey is no longer amongst us.

Biophotonics community suffered a heavy loss. His scientific interests included diverse scientific fields as theoretical and experimental research in the optics of biological tissues, biological and medical physics, biophotonics, biomedical optics, and control of optical parameters of biological tissues, etc. His publications are well known all over the world. One of them on the optical properties of tissues is included in the list of the 50 best publications of the entire Journal of Physics (IOP) series for 50 years of its existence and has been cited more than 1600 times. His papers were also included into J. Nano Research Top Papers (2016) and most cited papers of J. Innovative Optical Health Sciences. He has a great publication impact as co-author of 16 book chapters, more than 350 articles in peer-review journals and full texts conference reports, and 12 patents in the field of biophotonics. He has about 5,000 citations and an h-index of 32 (Scopus, March 2022).

Dr. Bashkatov had many students and followers in Russia, China, Portugal, the United States, and other countries, whom he willingly helped to master the complex problems of tissue optics. He devoted his time to doing a great job for the biophotonics community as a guest editor of dozens of journals and reviewed numerous articles from leading journals, trying to instill in the authors a culture of presenting scientific results. His professionalism and devotion to science was recognized with inclusion in the editorial board of the **J. Biomedical Photonics & Engineering**. **Dr. Bashkatov** has made a great contribution to the development of the J-BPE since its foundation in 2014, participating as an author, special editor of several issues of and co-editor of special sections related to tissue optics and spectroscopy.

Alexey has always been open to cooperation. Among his co-authors were specialists in the field of ophthalmology, gastroenterology, dentistry, and oncology.

We will always remember **Alexey** as a wise, kind, cheerful and decent person. All authors would like to express deepest condolences and sincere support to his relatives, friends, and colleagues!

Special Issue Editors:

Ivan A. Bratchenko, PhD
Department of Laser and Biotechnical Systems
Samara National Research University
E-mail: iabratchenko@gmail.com

Luís Oliveira, PhD
Physics Department,
Polytechnic of Porto
E-mail: lmo@isep.ipp.pt

 doi: 10.18287/JBPE21.08.010101

Elina A. Genina, PhD, DSc
Department of Optics and Biophotonics
Saratov State University
E-mail: eagenina@yandex.ru

Valery P. Zakharov, PhD, DSc
Department of Laser and Biotechnical Systems,
Samara National Research University, Russia
E-mail: zakharov@ssau.ru

Valery V. Tuchin, DSc, corr.-member of the RAS
Saratov State University, Russia
National Research Tomsk State University, Russia
Institute of Precision Mechanics and Control of the RAS,
Saratov, Russia
E-mail: tuchinvv@mail.ru

Types of Optical Coherence Tomography for Cancer Diagnosis: A Systematic Review

Neha Acharya[1], Sindhoora K. Melanthota[1], Manoj Khokhar[2], Shweta Chakrabarti[3], Dharshini Gopal[3], Dhyeya S. Mallya[1], and Nirmal Mazumder[1*]

[1] Department of Biophysics, Manipal School of Life Sciences, Manipal Academy of Higher Education, Manipal, Karnataka 576104, India

[2] Department of Biochemistry, All India Institute of Medical Sciences, Jodhpur, Rajasthan 342005, India

[3] Department of Bioinformatics, Manipal School of Life Sciences, Manipal Academy of Higher Education, Manipal, Karnataka 576104, India

*** e-mail:** nirmaluva@gmail.com

Abstract. Optical coherence tomography (OCT) is an emerging imaging technique that produces high contrast images that help distinguish different tissue layers by detecting the back-reflected near-infrared light. The technique is used to diagnose various diseases due to high contrast, three-dimensional imaging capability with high resolution, and a fast acquisition speed. The meta-analysis study was performed by the systematic review of literature in PubMed, Web of Science, Scopus, Google Scholar, Embase, and Cochrane Library using search terms relevant to "OCT", "Carcinoma", and "cancers". The various applications of different types of OCT are discussed in the detection and diagnosis of various cancers like colorectal cancer, breast cancer, skin cancer, brain cancer, prostate cancer, ovarian cancer and lung cancer. © 2022 Journal of Biomedical Photonics & Engineering.

Keywords: optical coherence tomography; cancer; tissue imaging.

Paper #3440 received 28 Jun 2021; revised manuscript received 01 Dec 2021; accepted for publication 21 Dec 2021; published online 4 Feb 2022. doi: 10.18287/JBPE22.08.010201.

1 Introduction

Optical coherence tomography (OCT) is a non-invasive, label-free optical imaging technique used for obtaining high-resolution images of biological tissues and other objects in real-time [1]. It was initially reported in 1991 as having a similar working principle as ultrasonic imaging where the reflected sound waves are detected, but OCT detects a back-reflected near-infrared light source (wavelength range of 700–1300 nm) [2, 3]. The resolution, however, is 10–50 times greater than ultrasound. Since OCT uses a longer wavelength, it can image at high resolution (2 to 15 μm), and profound imaging depth of up to 2 mm as scattering decreases with an increase in wavelength. OCT is used in imaging highly scattering tissues, where backscattered light is selected interferometrically from a defined depth, allowing two- and three-dimensional imaging wherein the source of endogenous contrast used is the local backscattering coefficient [4]. It is applied to the living cortex for refractive index measurements when a transmission measurement is infeasible. The light scattering ability of several tissues is responsible for the contrast generated. The technique is regarded as non-invasive imaging, having both *in vivo* and *ex vivo* applications. Optical fibre-based OCT can be combined with a great variety of instruments such as laparoscopes, endoscopes, catheters and surgical probes for real-time internal site imaging [5]. It is also a propitious technique for guidance during the abscission of tumours. The reflectance at the boundaries between multiple structural layers is measured within the sample. OCT is a non-contact optical helpful technique in imaging organs that cannot be biopsied, like the retina. The reflection delay of the targeted waves is calculated to obtain the depth of reflection. The dislocation of the beam is measured to obtain the cross-sectional image (tomography). Since the measurement of the delay in the reflection is tricky, a reference of measurement is utilized where one part of the light is given to sample and another to a reference with a known length [6]. Hence, it can provide information about the internal structure of the tissues and organs within seconds as it has a higher image acquisition speed. The speed is usually determined based on the rate

at which the depth of tissue is scanned per second, which is referred to as A-scans [7]. Therefore, the technique is used in various biomedical applications, including ophthalmology, dermatology, cardiology, cancer, neuroscience, dentistry, etc. [1]. In this review, we discuss the various types of OCT in the diagnosis of cancers associated with colon, skin, breast, brain, ovary, prostate and lungs.

2 Methodology

With a simple search of the MEDLINE database in PubMed, we have found a large number of literature on various applications of OCT in the field mentioned above. The graphical representation of the collection of publications in the last 10 years with search items as "type of technique" and "application" is illustrated (Fig. 1). Since most of the publications are in the field of ophthalmology, followed by cancer, cardiology, and neuroscience, there is tremendous room for further research in cancer.

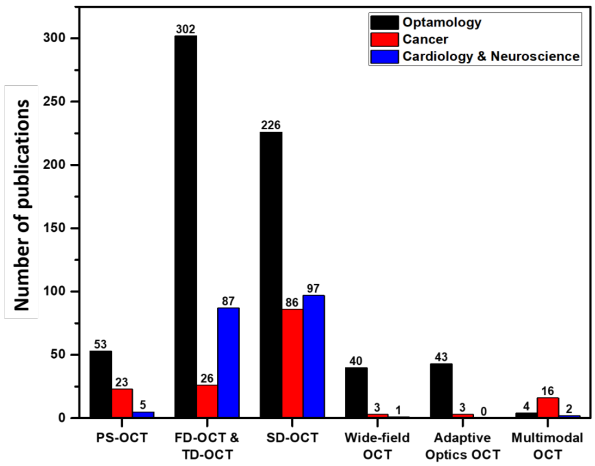


Fig. 1 The total number of publications in PubMed on applications for various types of OCT in last 10 years.

2.1 Search Strategy

Since no ethical regulation was required for meta-analysis studies, we searched electronic databases such as PubMed, Web of Science, Scopus, Google Scholar, Embase and Cochrane Library for the last 10 years, i.e., 2010 to 2020. The search queries used include "Optical coherence tomography and cancer or carcinoma", "Optical coherence tomography and Prostate cancer or carcinoma", "Optical coherence tomography and lung cancer or carcinoma", "Optical coherence tomography and skin cancer or carcinoma", "Optical coherence tomography and colorectal cancer or carcinoma", "Optical coherence tomography and ovarian cancer or carcinoma", "Optical coherence tomography and breast cancer or carcinoma", and "Optical coherence tomography and brain cancer or carcinoma". A total of 1018 papers was identified. Reviewing of papers were performed by two reviewers, and a third reviewer solved any conflicts.

2.2 Inclusion and Exclusion Criteria

The criteria applied to include the studies for the meta-analysis were as follows: (i) studies including the application of OCT to detect and diagnose cancer or malignant cells or tissues, (ii) articles from which adequate data could be extracted such as true and false negatives and true and false positives values, and (iii) relevant articles published in the past decade (2010 – 2020). The criteria based on which papers were excluded as follows: (i) reviews, animal studies, book chapters, and conference proceedings, (ii) articles for which abstracts were not available, (iii) papers where OCT was not used for the diagnosis of cancer, (iv) papers in other languages except English, (v) articles including OCT for retinal imaging, and (vi) studies without any sufficient data. With inclusion and exclusion criteria, 36 papers are shortlisted in this review. Table 1 summarizes the types of optical coherence tomography for the diagnosis of different cancers, Table 2 compares different types of OCT for cancer diagnosis, and Table 3 provides the diagnostic summary of each paper groped by various cancer type.

3 Instrumentation

The OCT has shown remarkable outcomes in detecting changes in pathology of stratified tissues such as the eye. There are various types of OCT developed to visualize the tissue structure. Fig. 2 describes various types of OCT in investigating types of cancer. Tissue-specific contrast can be generated by changing the input polarization state of light in polarization sensitive OCT (PS-OCT) [8]. Another variant of PS-OCT is cross-polarization OCT (CP-OCT), wherein parallel and orthogonal images are acquired by imaging the variations in the initial polarization caused by cross-scattering and birefringence in the tissues [9]. OCT-based angiography (OCTA) is also an OCT adjunct for non-invasive angiography, where circulation in functional vessels are envisioned without any exogenous contrast agents. In time-domain OCT (TD-OCT), the first-ever OCT, the light was divided into two beams – the central beam and the reference beam, as mentioned previously. For each depth profile (A-scan), the reference length was altered to that depth, and the combined light intensity was measured, and the sample reflectance profile is obtained. The path-length must be similar for the light from each path to interfere. The image of the cross-section is obtained by scanning the sample laterally (B-scan). Fourier-domain OCT (FD-OCT) is another type of OCT that directly encrypts the delayed time echoes in spectral interferogram. In FD-OCT, the A-scans are obtained from the spectral information present [10]. The availability of additional spectral information ensuring mechanical scanning is not necessary, unlike TD-OCT. It is classified into two forms based on configurations of the system – spectral-domain OCT (SD-OCT) and swept-source OCT (SS-OCT). SD-OCT is designed with a broad bandwidth light source, one-dimensional linear

Table 1 Types of optical coherence tomography for the diagnosis of different cancers.

Author	Year	Country	Design	Type of OCT	Type of Cancer	Number of Patients	Age (mean or median)
Li et al. [13]	2019	USA	Multimodal	Co registered OCT with near infrared (NIR) fluorescence imaging	Colorectal	NA	NA
Ashok et al. [14]	2013	UK	Multimodal	Multimodal Fourier Domain (FD) OCT with Raman spectroscopy	Colonic adenocarcinoma	66	NA
Yuan et al. [18]	2010	USA	Multimodal	Co-registered OCT and fluorescence molecular imaging (FMI) system	Colon	4	NA
Erickson-Bhatt et al. [20]	2015	Illinois	Surgical probe	Handheld surgical OCT imaging probe	Breast	35	NA
Kennedy et al. [25]	2015	Australia	NA	Needle-based OCT	Breast	1	70
Gubarkova et al. [26]	2019	Russia	Multimodal	Spectral domain (SD) multimodal OCT	Breast	33	30–80
Yang et al. [27]	2020	China	Pro	Full-field (FF) OCT	Breast	158	NA
Wang et al. [28]	2018	USA	NA	Polarization-sensitive (PS) OCT	Breast	9	NA
Butola et al. [29]	2019	India	NA	Swept-source (SS) OCT	Breast	22	NA
Zhou et al. [30]	2010	USA	Integrated	OCT and optical coherence microscopy (OCM)	Breast	44	NA
Dubey et al. [31]	2019	India	NA	OCT	Breast	24	NA
Lindner et al. [32]	2012	Germany	Pro	OCT	Breast	34	29–68
Assayag et al. [49]	2014	France	NA	FF-OCT	Breast	22	58 (mean)
Mogensen et al. [33]	2009	Denmark	NA	OCT and PS-OCT	Skin	100	NA
Adabi et al. [34]	2017	USA	NA	OCT	Skin	21	NA

Batz et al. [35]	2018	Germany	NA	OCT	Skin	25	69 (mean)
Turani et al. [36]	2019	Brazil	NA	SS-OCT	Skin	69	20–80
Tes et al. [37]	2018	USA	NA	SS-FD OCT	Skin	1	25
Coleman et al. [40]	2013	UK	NA	OCT	Skin	78	59 ± 13
Banzhaf et al. [41]	2014	Denmark	Pro	OCT	Skin	16	52–82
Ulrich et al. [42]	2015	UK	Pro	OCT	Skin	155	≥18
Marvdashti et al. [43]	2016	USA	NA	PS-OCT	Skin	42	NA
Holmes et al. [44]	2018	Germany	Pro	OCT	Skin	NA	≥18
Braunmühl et al. [45]	2016	Germany	NA	Frequency domain (FD) OCT	Skin	32	68 (mean)
Wessels et al. [71]	2015	Netherlands	NA	OCT	Skin	18	47–88
Yashin et al. [52]	2019	Russia	NA	Cross-polarization (CP) OCT	Brain	30	NA
Assayag et al. [53]	2013	France	Pro	FF-time domain (TD) – SD-OCT	Brain	18	19–81
Kut et al. [54]	2015	USA	NA	SS-OCT	Brain	37	NA
Yashin et al. [55]	2019	Russia	NA	CP-OCT	Brain	17	NA
Wang et al. [58]	2013	USA	NA	FD-PS OCT	Ovarian	18	NA
Yang et al. [59]	2012	USA	NA	PS-OCT	Ovarian	18	61
Swaan et al. [63]	2018	Netherlands	Pro	Needle-based	Prostate	4	≥18
Muller et al. [64]	2018	Netherlands	Pro	Needle-based	Prostate	20	≥18
Gardecki et al. [65]	2019	Boston	NA	Micro	Prostate	11	NA
Lopater et al. [66]	2016	France	NA	FF-OCT	Prostate	38	NA
Wei et al. [72]	2012	China	NA	FD-OCT	Lung	48	≥18

Hariri et al. [73]	2019	United States	Retro	PS-OCT	Lung	26	≥18

NA: Not applicable

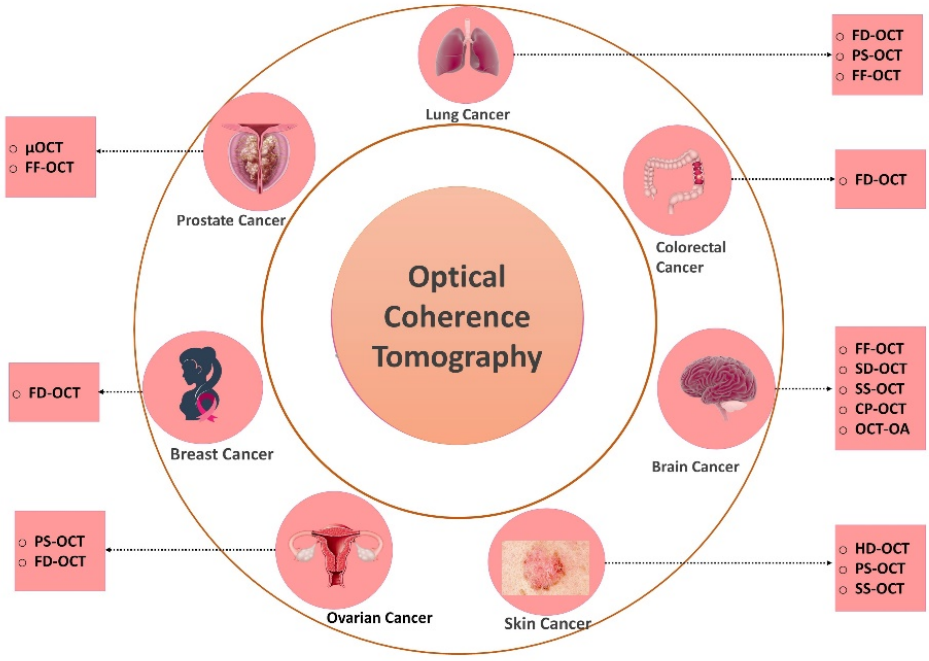


Fig. 2 Different types of optical coherence Tomography (OCT) techniques used in the diagnosis and medical treatment of various types of cancers. (Polarization-sensitive OCT (PS-OCT; cross-polarization OCT (CP-OCT); OCT-based angiography (OCTA); time-domain OCT (TD-OCT); Fourier-domain OCT (FD-OCT); spectral-domain OCT (SD-OCT); swept-source OCT (SS-OCT); Full-field OCT (FF-OCT); micro-optical coherence tomography (μOCT)).

array sensor and a spectrometer that captures the interferogram encrypting the echoes in wavelength. The spectral interferogram is captured using a single detector in SS-OCT, where the laser source frequency is swept through a range of optical frequencies [11]. FD-OCT is more sensitive than TD-OCT due to the high scanning speed and signal-to-noise ratio. The lower speed of TD-OCT is due to the reference mirror that is in motion and its cycle time, whereas in FD-OCT, it is stagnant, and multiple points can be sampled at once [12]. Full-field OCT (FF-OCT) is a recently developed method that allows a high-resolution wide-field view over the entire field and is used in cancer diagnostics [9]. A light-emitting diode (LED) or halogen is used as a light source to illuminate a full field. FF-OCT provides the 3D resolution on tissue samples that are label-free (up to a depth of 200–300 μm). The image acquisition time is less than 5 min, and imaging performance is almost the same in fresh or fixed tissue. Short pulse lasers like Cr^{4+}: Forsterite lasers are used in OCT imaging for research studies. They have a very high resolution due to their short coherence lengths and more extraordinary output powers. Cr^{4+}: Forsterite laser generates output powers of 100 mW giving pulses of 1300 nm wavelength resulting in a resolution of 5–10 μm. Ti: AI2O3 laser, another short-pulse laser, can provide resolutions of 1 μm at 800 nm. Semiconductor-based light sources or superluminescent diodes are used instead of short pulse lasers. They can have resolutions up to 15 μm and power of 10–15 mW at 1300 nm. In the following section, the applications of OCT are discussed in selected types of cancer (Fig. 3).

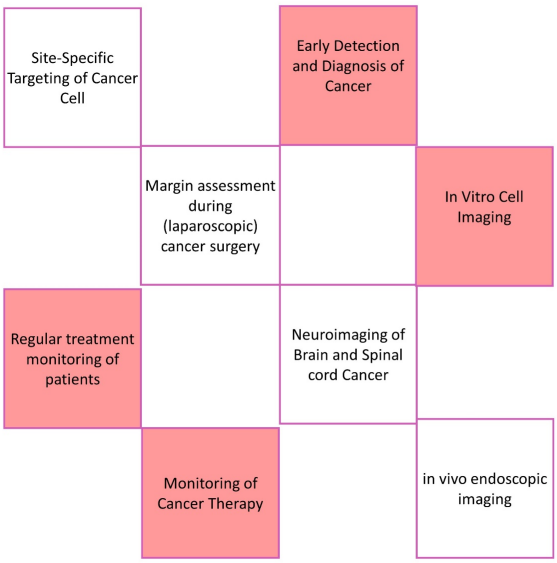


Fig. 3 The application of the OCT technique to various types of cancer.

Table 2 Compares the different types of OCT for cancer diagnosis.

Types of OCT	Principle and information	Applications	Advantages	Limitations	Cancer Type	References
Polarization sensitive (PS) OCT and cross-polarization (CP) OCT	Based on a newer contrast mechanism (backscattered light). Detects images when polarization state is orthogonal to the incident state	Intraoperative margin detection, collagen protein detection	To obtain 3-D information for analysing B-scan images and confirming the origin of the signal. Transverse resolution of ∼10 μm in the focal plane and an axial resolution of 7.6 μm in air	The rather shallow image depth that can be used to cover images and image depth is limited to ~0.5mm due high sensitivity	Lung, Skin, Breast, Ovary, Brain	[8, 9, 30]
Time-domain OCT (TD-OCT)	Based on examining the mechanical length of the path followed by light	Tumour detection	Axial resolution of 10 μm	Random property of tissue could limit its imaging resolution	Brain, Skin	[10, 12]
Fourier domain OCT (FD-OCT)	Fourier transform of the spatial correlation function of the refractive index	FD-OCT helps in understanding the structure information	Higher sensitivity due to axial locations are recorded throughout the entire A-scan duration. Resolution limit of 1–15 μm. Utilized in the clinical diagnostic screening of large tissue areas	Inadequate resolution for visualizing fine morphological details. Random property of tissue could limit its imaging resolution	Brain, Ovary, Lung, Colorectal	[10, 12, 14]
Spectral domain OCT (SD-OCT)	1-D linear array sensor, broad bandwidth light source, and a spectrometer capturing the interferogram encrypting the echoes in wavelength	Obtain tissue morphology	No pupil dilation required, higher machine speed the speed of the machines is higher, minimized motion artefacts, better image quality, and comfortable patient examination. It is used in clinical *in vivo* imaging and screening of cancer	Large file sizes and high cost. Axial resolution up to 3.8 μm	Brain	[11]
Wide-field optical coherence microscopy	Based on spectral-domain and swept-source technology	Intraoperative neurosurgical setting was demonstrated to assess tumorous glial and epileptic margins	Active eye tracking improves image stability. Spatial resolution of 1.8 μm × 0.9 μm (transverse × axial). Used for *in vivo* imaging of lesions	Lower resolution and requires artifacts minimization	Skin, Brain, Breast	[9, 20]

Multimodal OCT	OCT with a combination of ultrasound, photoacoustic/ ultrasound, near-infrared imaging (NIR), fluorescence molecular imaging (FMI) and Raman spectroscopy	Diagnostic Imaging and Treatment Monitoring	Allows cross-sectional envision of tissue morphology and vasculature with high sensitivity and spatial resolution	Limited clinical impact compared to pure OCT systems, microscopic techniques with small FOVs allow only tunnel vision in clinical diagnosis	Breast, Colorectal	[13, 14, 16, 18]

4 Applications of OCT

4.1 Colorectal cancer

Colonoscopy, considered the best technique for colorectal cancer (CRC) diagnosis, helps detect abnormal tissue growth on colon or rectum mucous membrane known as colorectal polyps. Though the technique is considered as a standard procedure, colonoscopy detects only the surface morphology of the rectal wall; also, the technique cannot determine the abnormal subsurface microvasculature, which is highly linked to CRC. Thus, a biopsy, an invasive and time-consuming method with limited accuracy, is required for cancer staging. Passing the OCT probe through the endoscope accessory channel will help the endoscope to visualise the mucosal tissue at a resolution of 2–10 μm. However, different probes have different penetration depth and resolution, and there is a need for uniformity and standardisation of endoscopic OCT techniques. To improve diagnostic accuracy, multimodal imaging systems such as OCT combined with ultrasound, photoacoustic, and near-infrared imaging (NIR) are developed. Out of these, combining OCT and NIR fluorescence is effective as it allows cross-sectional envision of tissue morphology along with the vasculature with high sensitivity and spatial resolution. The microanatomy of the structures can be visualised with much more detail with OCT, and the NIR fluorescence can help in lesion studies. Multimodality serves to improve the ability to observe the morphology and the molecular composition, and biochemistry simultaneously. Hence, it is considered an essential tool for the observation of hallmarks of colorectal cancer. Also, OCT/NIR fluorescence imaging reduces the cost of the procedure and time as data from OCT and NIR fluorescence can be acquired with a single probe in one session [13].

In a study, OCT/NIR fluorescence was combined for imaging probe into a miniature endoscope. Imaging with both components was processed simultaneously with high resolution and speed. The multimodal system was validated using food and drug administration (FDA) approved contrast agent ICG (indocyanine green) with a rat model having the CRC. The NIR fluorescence could show the changes in morphology and areas occupied by blood vessels using OCT images placed parallel (co-polarized) to each other. The tumorous region is identified due to the accumulation of ICG in a more considerable amount when compared to normal tissues hence, ICG can be used for describing the tumour border and angiogram. The amount of ICG and the distance from the probe was used to determine the signal intensity in NIR fluorescence imaging. 2D images from NIR fluorescence and corresponding OCT images placed collateral to each other indicated that polyps could be identified using 2D NIR images but not the types of polyps. Thus, for better cross-sectional visualization, OCT images were used. 3D OCT and NIR can be used for the clear identification of polyp types. Therefore, the technique is minimally invasive, and it is easier to integrate into clinical practice. Clinical studies show that the spectra obtained using fluorescence spectroscopy cannot distinguish between the cancerous tissues of the colon and non-cancerous tissues [13]. Studies showed that Raman spectroscopy was an efficient tool to distinguish between normal and cancerous tissues. However, it cannot be used as a disease diagnostic tool because the classification efficiency is very low when interpatient variability is considered [14]. Therefore, a multimodal approach where Raman spectroscopy is interfaced with methods like FD-OCT provides additional information about the tissue. Raman spectroscopy helps in understanding the biochemical nature while OCT helps in understanding the structure, information from both tools is combined to examine the capability of the multimodal system as they act as an efficient tool for non-invasive optical biopsy [15]. The study comprised normal tissue samples and tumorous samples, and images were captured using both devices for each sample [16]. A quantification algorithm must be implemented because a spectroscopic technique which is analysed numerically (quantitative) is combined with an imaging technique which is analysed categorically (qualitative), for the imaging technique. For both feature selection and parameter reduction in Raman and OCT data principle component analysis (PCA) was used.

Fig. 4 indicates that differences exist in the morphology of the two tissue types. Yet, the investigation of obtained images was insufficient for diagnosis when interpatient variability is considered. When the

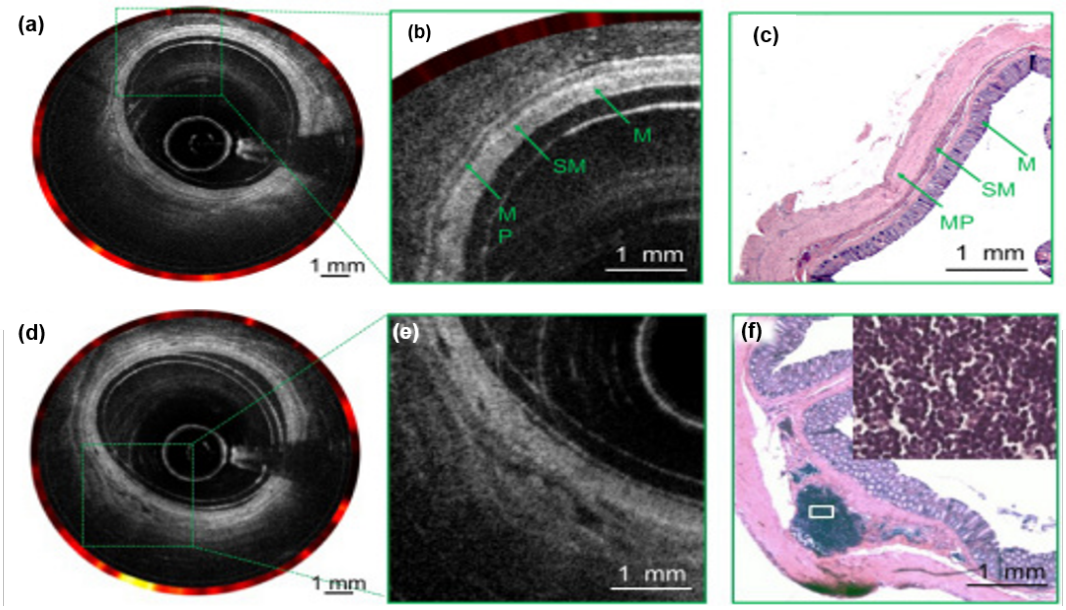


Fig. 4 (a) The combined OCT and NIR fluorescence image of normal rectum, (b) enlarged view of the dashed box in (a), (c) histology; (d) the combined OCT and NIR fluorescence image of adenocarcinoma; (e) enlarged view of the dashed box in (d); (f) histology. M: mucosa; SM: submucosa; MP: muscularis propria. Adapted with permission from [13] © The Optical Society.

multimodal approach was used in the analysis, both specificity and sensitivity were increased significantly. Though histology and excisional biopsy based on white light are considered as the standard for the detection of cancer in the gastrointestinal tract (GI), the chances of obtaining negative results are more because of sampling errors [17]. FD-OCT imaging system utilized a light source emitting with a broad spectral range. The images obtained from OCT combined with FLOT (Fluorescence-based Laminar Optical Tomography) distinguish between cancerous lesions and non-cancerous. This information was used as a criterion to estimate the dimensions of tumours, and it was observed that FLOT gives a more accurate estimation of the diameter of the tumour. In contrast, the thickness of the tumour was determined from OCT images when placed orthogonally [18].

4.2 Breast cancer

Breast-conserving surgery (BCS) is a method used to treat early-stage breast cancer, which when followed by radiotherapy shows lower mortality over mastectomy [19]. Thus, the necessity of identification and complete resection of the tumour has been increased significantly. Since all these methods are time-consuming and have high sampling errors, developing a technique that allows live imaging and detection of tumour margins is crucial. Among different methods developed, OCT was a very effective tool for intraoperative margin assessment of breast tumour [20, 21]. Explicitly, it is observed that scattering was more in the case of breast cancer samples when compared to non-cancerous tissues. Thus, it is possible to distinguish the cancerous and healthy tissues. A portable intraoperative SD-OCT system, where image contrast was based on backscattered light (polarization-sensitive) was developed [20]. Human subjects undergoing reduction mammoplasty (breast reduction surgery) or mastectomy were recruited for the study. Correlation coefficient analysis was performed to classify the closely correlated images based on their location. The adipocytes were recognizable due to their shape and lipid content in the OCT image of the tissue, which shows that conventional OCT on itself can distinguish between the fibro-adipose tissue and Invasive Ductal Carcinoma (IDC). Tumour cells and the healthy breast tissue in IDC result in disruption of the collagen structure, which is less delayed compared to the normal stroma. Significant differences between stroma and IDC were observed from delayed (retardation), and Degree of Polarization Uniformity (DOPU) derived OCT analysis based on backscattered light. The measurements use metrics, CV, DOPU and retardation the capacity of the OCT to diagnose the disease was assessed.

Breast cancer is a collective disease that exhibits a wide range of clinical, structural and molecular attributes among tumours and within a tumour. Breast cancer is classified into non-invasive (Ductal cancer in situ- DCIS) and invasive types (Luminal A, Luminal B, HER2-positive) and basal-like (triple-negative) subtypes [22]. The study of structural and molecular breast cancer features helps in detection of tumour margin vividly. Imaging methods of breast cancer such as X-ray computed tomography, ultrasound, positron emission tomography (PET), and magnetic resonance imaging (MRI) are used to determine the dimension of tumour or lymph node, the general structural information or morphology [23], however, tissue having less than a few

mm and false (negative) surgical margin cannot be determined using these methods due to the low resolution. To overcome this, a technique with a high optical resolution which can approach the histopathology level in providing details in nearly real-time to detect the margins of lumpectomy. The conventional OCT images do not provide information about the rigidity of the tissue, hence Optical Coherence of Elastography (OCE) images of the reference tissue can be compared with the deformed states tissue to obtain such information [24, 25]. The study shows that the OCE-based approach can assess the morphology, malignancy degree of tumours, and categorization of cancer subtypes. Samples of freshly resected breast tissues obtained from patients were used. The specimens included both the tumorous region and peritumoral area and were studied within a short duration of time after the resection. The samples were categorized into benign and malignant breast tissues based on the histopathology results. Real-time polarization-sensitive images of the tissue are obtained using a customized multimodal SD-OCT system. The images were used to detect the state of connective tissue component when the OCT images are placed orthogonally (cross-polarized). The OCT-based findings were compared with results of the histopathology. The results indicated the differences between various types of tissues [25]. OCE images in Fig. 5 showed the details of the ducts filled with tumour cells for breast cancer Ductal Carcinoma in Situ (DCIS) and Luminal A with highly increased stiffness. Thus, the technique can be used to distinguish the different cancer subtypes. Also, the images obtained showed a higher contrast than the images obtained from standard and PS-OCT images [26].

Normal, cancerous tissues, benign breast lesions, and resected axillary lymph nodes were examined using FF-OCT. The minimum sensitivity and high specificity were observed in breast cancer diagnosis, and they diverged in nodal assessments. These tissue-sparing approaches proved highly efficient in breast cancer and nodal metastasis diagnosis compared to histology [27]. The implementation of PS-OCT for enhancing breast cancer detection was reported. The standard OCT and PS-OCT-based metrics obtained were complementary for the differentiation of healthy fibro-adipose tissue, stroma, and IDC, differentiated with an accuracy of 89.4%, illustrating the potential of PS-OCT for intraoperative differentiation of human breast cancer [28]. A machine learning (ML) algorithm performed the volumetric analysis of normal and breast cancer tissue and their classification based on a support vector machine (SVM) by the SS-OCT images. This algorithm classifies the cancerous tissue with 91.56% sensitivity, 93.86% specificity, and 92.71% accuracy and extracts features from the whole volume of the tissue. Therefore, breast cancer diagnosis by extracting quantitative features from various types of OCT images could be a potential approach and a key tool for a fine-needle-guided biopsy [29].

The entire tumour, along with the surrounding healthy tissue is removed using breast-conserving surgery (BCS). Tumour margins are assessed based on histopathological analysis. It is found to be a not so efficient tool that leads to the re-excision to remove additional tissue, hence tools enabling effective removal of tumorous tissue is used to reduce re-excision rates. Despite several advantages, conventional OCT cannot differentiate tumour from uninvolved stroma [29–31]. Hence, OCT integrated with OCE is used to measure the tissue deformation, and an image of tissue elasticity is acquired. Optical coherence micro-elastography (OCME) is a type of OCE capable of detecting the difference in phase and compressibility of tissue. It was found to clearly distinguish between a malignant tumour and uninvolved stroma resected human breast tissue. For tissues with dimensions of ~50 × 50 mm, a wide-field imaging system is used.

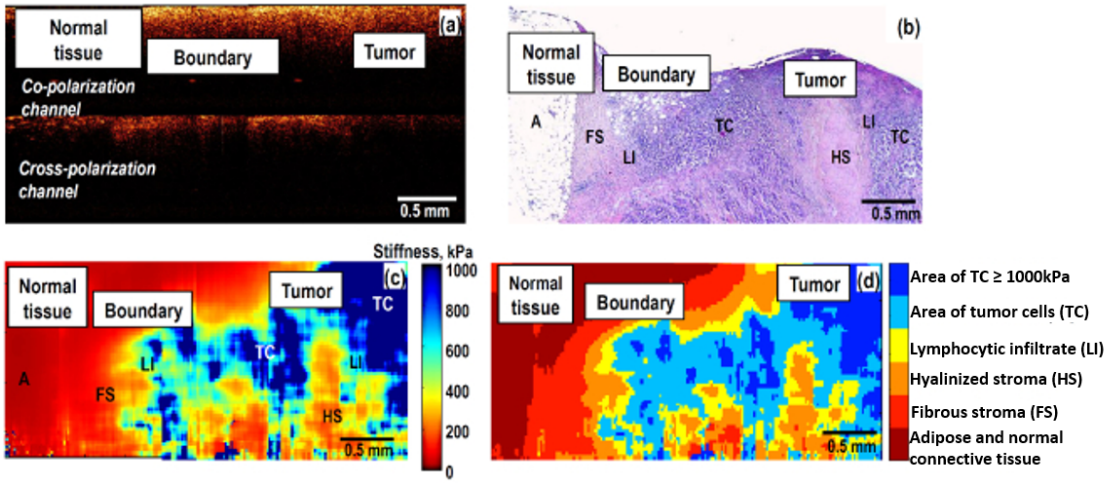


Fig. 5 Visualization of a transitional zone between normal breast tissue and tumour region with (a) the CP OCT image; (b) H&E-histological slice; (c) stiffness map; (d) morphological segmentation of the OCE image into areas corresponding to various tissue components. Adapted with permission from [26] © The Optical Society.

The study based on an FD-OCT system-generated OCT images by creating a network of images to image a larger area. The results showed wide-field elastograms had strain only in denser tissues. OCT images and elastograms obtained from patients undergoing either mastectomy or BCS are used. In both the benign tumour images, papilloma appeared to have a highly fibrous structure, while the orientation of the fibres appeared to be more organized in malignant tumours [26]. Images were obtained from a dissected tumour and a lumpectomy also. Thus, it was observed that the wide-field OCME could be used as a tool to assess the margins of resected breast tissue. Features extracted from OCT images are used to classify normal, and cancer breast tissues with the help of a multi-level ensemble model. The measurement can be used as a biomarker for removal of whole tumour tissue without any special tissue preparation [31]. Evaluation of hair shaft alterations using OCT in chemotherapy-induced alopecia was performed by Lindner et al. [32]. After chemotherapy, significant changes were observed in hair structure may be due to reduction of hair shaft calibre which could be studied by OCT imaging to gain more insight into induced changes [32]. The ability of OCT is to allow surgeons observe the morphological characteristics of the tissues, at a greater surface area also while ensuring the tissue is not damaged makes it an attractive tool in studying breast cancer [5].

4.3 Skin cancer

Studies reveal that OCT can be used for the detection of skin cancer because of its ability to envision features beneath the dermal layers, which are prominent areas for the initial appearance of skin cancer. It is found that the collagen alignment and distribution are altered due to the development of skin cancer which results in a change in the optical anisotropic nature (birefringence) of skin [31, 32]. Differentiation of different skin cancer types using OCT imaging was evaluated, and correlations between various tumour types and recurring tumour characteristics were observed [33]. The basal cell carcinoma (BCC) is commonly observed in Caucasians [34]. The disease is found to be multifactorial, and excess exposure to the sun plays a significant pathogenic role. Clinical diagnosis of BCC is usually performed using dermoscopy [35]. Non-invasive techniques such as reflectance confocal microscopy (RCM) [36], conventional OCT and multiphoton tomography (MPT) are also available for *in vivo* diagnosis. High-definition optical coherence tomography (HD-OCT) is a technique that helps in a non-invasive diagnosis with real-time 3D imaging capability and at a cellular resolution. A pilot study including HD-OCT images of superficial BCC, nodular BCC and infiltrative BCC was conducted and the lesions were fully excised and examined histopathologically for confirmation. This technique could distinguish between the subtypes, and further development in the technique could explore the skin up to micrometre level depth [37, 38].

BCC lesions depth can be determined using OCT. An OCT signal of low strength at the periphery of the cell nests was identified as corresponding to cellular palisading. The optical attenuation coefficient on OCT and the nuclear-cytoplasmic ratio of cells from histology were correlated with weak inverse linearity. OCT provides accurate measurement of BCC, along with identifying the presence of peripheral palisading [39, 40]. Banzhaf et al. [41] reported the lesions studied BCC imaging using OCT throughout imiquimod treatment in 20 biopsy-verified patients were identified both clinically and using OCT. It was observed that OCT identified all the lesions. The quality of the images was reduced due to crusting, ulceration and active treatment. OCT showed thinning of acute keratosis (AK), indicating the treatment effect. All treated BCCs were cleared, but residual tissues in 4 cases were observed clinically, this could be ruled out by OCT. OCT imaging along with clinical evaluation and dermoscopy improved the diagnostic accuracy of BCC from 65.8% to 87.4% [42]. Extraction of features such as intensity and phase retardation from polarization-sensitive OCT (PS-OCT) images for the classification of normal and cancer tissues was reported by Marvdashti et al. [43] achieved 95.4% sensitivity and specificity in detecting BCC. In another study, the impact of diagnostic parameters such as image quality, lesions, observer and inter observer variability on the diagnostic performance of OCT for the assessment of diagnostic potency of BCC subtypes in 234 patients was studied. It was observed that lesion location had no impact on OCT diagnostic performance, whereas the image quality, observer confidence had a direct correlation. Overall, BCC subtype could be determined with moderate accuracy [44]. FD-OCT imaging was used to extract and evaluate morphological features of BCC with horizontal and vertical imaging modes, which provides information required for the diagnosis, especially in nodular BCC [45].

Granular cell tumour (GCT), also called Abrikossoff tumour, is a rare soft tissue neoplasm that is usually benign. The occurrence is more in women and dark-skinned individuals and less in children. It is mainly known to occur in the oral cavity, and malignancy is less (1–2%). Surgical excision is the only treatment of GCT. Therefore, a technique that accurately evaluates the morphology and extension of the tumour is required [46]. SS-OCT system was used with a high-speed tuneable laser source. An axial scan (A-scan) obtained from the reflectivity profile was grouped for different transversal positions to generate a cross-sectional image and is referred to as B-scan. The object's top view was depicted in the C-scan. The results demonstrated that the OCT images of GCT show verrucous epidermal hyperplasia, which appears as the hyperreflective, uneven surface of the tissue. Also, the dermo-epidermal junction is visible in the healthy skin but is not distinct in the GCT region. Thus, the abnormal skin can be delineated using this technique to differentiate healthy tissue from tumorous tissue.

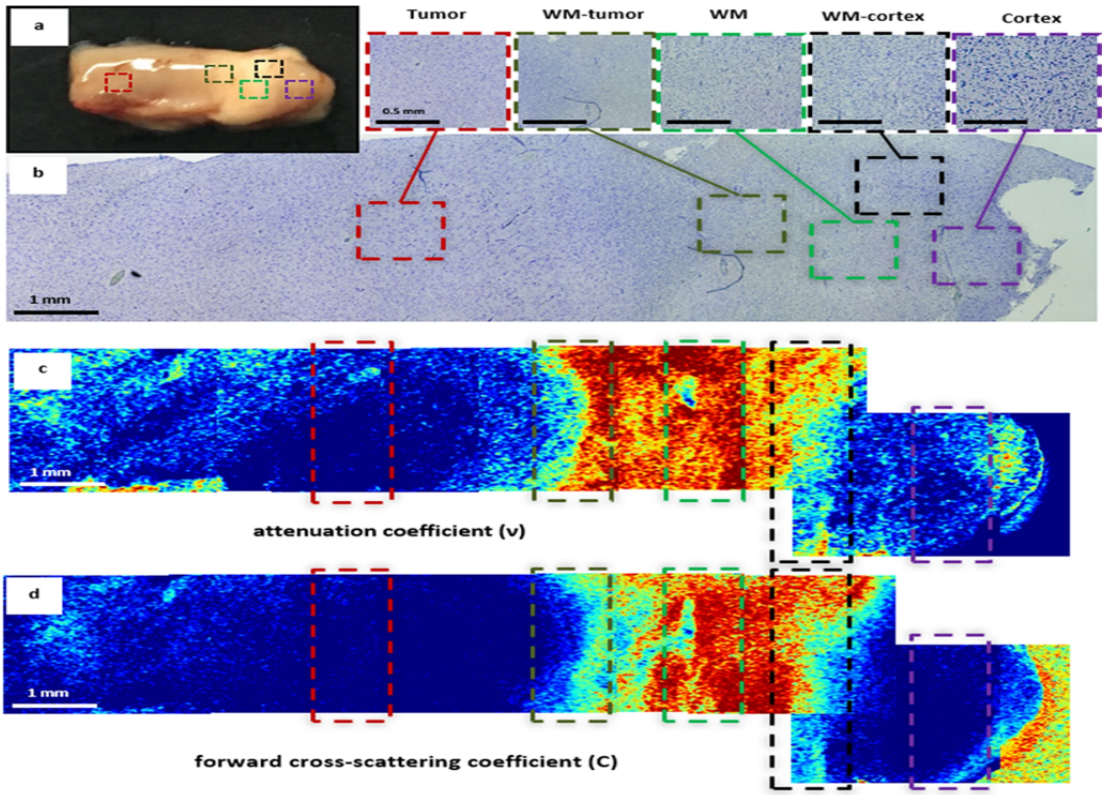


Fig. 6 (a) Brain specimen marked with different areas of interest by different colours; (b) with corresponding histology; (c) colour-coded maps based on attenuation coefficients; (d) colour-coded maps based on forward cross-scattering coefficients. WM-white matter. The Figure is adapted with kind permission from [52].

4.4 Brain cancer

Brain cancer patients have finite survival time as it recurs and later leads to death. Surgery is considered the only best treatment. The extent of resection is a significant risk factor linked to delayed tumour reappearance and, thus, longevity of the patient [46, 47]. Tissues from patients with grade II, grade IV brain cancers were obtained from surgery navigated by MRI and SS-OCT cross-sectional images. The precise identification of high-grade and low-grade human brain cancer was performed based on the established attenuation threshold. Microscopic structures that add to attenuation data in categorizing cancer from non-cancer white matter were identified using OCT images. High-grade cancer appeared as heterogeneous regions in which hyper-intense signals surrounded hypo-intense signals. Thus, OCT images enabled the identification of necrosis and hyper-cellularity [47].

A collection of tumours, including benign, malignant and slow-growing, are observed in the primary central nervous system (CNS). Patients with brain tumour survive only on complete resection of tumour mass, which is identified through postoperative imaging. Full-field OCT (FF-OCT) is a recently developed method that allows a high-resolution wide-field view [48]. A light-emitting diode (LED) or halogen is used as a light source to illuminate the full field. FF-OCT provides the highest OCT 3D resolution on tissue samples that are label-free (up to a depth of 200–300 μm). The image acquisition time is less than 5 min, and imaging performance is almost the same in fresh or fixed tissue [49]. Studies show that TD- or SD-OCT systems have an inadequate resolution for visualizing fine morphological details in CNS studies. The myelinated axon cell fibres, cyton of neurons and vasculature in the human epileptic brain and cerebellum were studied using the FF-OCT images. The images distinguished between meningiomas and hemangiopericytoma in meningeal tumours. The modifications in the architecture of brain tissue generated by infiltrative gliomas were detected.

Medulloblastoma is the most prominent malignant paediatric brain tumour with the highest ability to spread across the tissues (metastasize). The flow of cerebrospinal fluid is blocked due to the proliferation of the tumour, causing hydrocephalus. Surgical resection, chemotherapy and high-dose radiation are the treatment options used commonly, but most paediatric patients suffer from impaired intelligence and neurocognitive dysfunction due to the radiation treatment [9, 50]. Since it provides microstructural resolution and has an association with histology, OCT is considered a significant biomedical imaging modality for detecting brain tumours. The optical coefficient was measured for glioma specimens obtained *in vivo* and *ex vivo*. OCT optical attenuation (OCT-OA) images, as depicted in Fig. 6, have shown a significant correlation with histological images and provide enhanced distinction compared to structural OCT images using the local attenuation [51, 52].

Diagnosis of brain tumour was carried out using FF-OCT, a non-invasive technique that does not even

need contrast agent and tissue preparation. Imaging of brain tumours including low-grade and high-grade gliomas, meningiomas, and choroid plexus papilloma was performed. A neuron, CNS vasculature, and myelin fibres subpopulations were detected. Cortex could also be identified, but glial cells including astrocytes were not observed. The first application of label-free and real-time FF-OCT for brain cancer imaging was reported by Assayag et al. [53]. The feasibility of label-free, quantitative OCT for differentiating cancerous from non-cancerous human brain tissues was tested by Kut et al. [54] based on volumetric OCT imaging data. Lower optical attenuations of both cancerous core and infiltrated zones were compared with non-cancerous white matter, OCT achieved high sensitivity and specificity. This attenuation threshold was used to confirm the intraoperative feasibility, and it was observed that the OCT system displays a colour-coded map in real-time, thus providing direct visual cues for cancer versus non-cancer regions. In the study conducted by Yashin et al. [55], CP-OCT was performed on the brain to distinguish between cancerous and non-cancerous cells. CP-OCT scans were compared with the histology of specimens. The method showed 87–88% accuracy in diagnosis. *In vivo* CP-OCT images of brain tumour displayed vertical striations due to blood vessels. The distinctive feature of CP-OCT was its single intensity. The neuro-navigation feature of CP-OCT could help neurosurgeons with valuable information.

4.5 Ovarian cancer

Ovarian cancer is the form of cancer that has the highest death rates of all the gynaecologic cancers. The survivability is less due to the early metastasis and absence of effective techniques for disease screening and diagnosis [56]. Prophylactic oophorectomy (PO) is considered the standard treatment found to reduce the risk of ovarian cancer [56]. Also, new intraoperative devices that could diagnose ovarian cancer in earlier stages reduce the use of PO and decrease the high death rate, particularly in women with a higher chance of acquiring the disease [56]. OCT combined with techniques like ultrasound, photoacoustic imaging enhances optical absorption of tissue, scattering information and structures of tissues present at deeper sites. FD-OCT system for which swept source is based on the bandwidth (110 nm) was used. Ovaries from different species, both human and porcine species were used. The boundary indicating the presence of a cyst or follicle beneath and tissue features were visualized using OCT images [57].

A logistic prediction model employing the phase retardation rate, obtained from phase images of polarization-sensitive OCT (PS-OCT), as a parameter to characterize the malignant and normal ovarian tissue with 100% sensitivity and specificity was introduced, which could be an effective tool for the detection and diagnosis ovarian cancer [58]. A mathematical descriptor reducing the dimensions of a classifier's input data while preserving essential features was presented by St-Pierre et al. [57] that allowed exploring the features space leading to optimal classification. Multiple statistical models were presented with < 70% accuracy for the detection of cancer tissue. The approach reduces the resources required to achieve accurate classification, enabling intraoperative surgical guidance. The studies showed that PS-OCT is an adequate device to detect ovarian cancers, as the phase retardation and optical scattering co-efficient are obtained from benign and malignant ovaries, respectively. Sirius Red staining was also used to assess the properties. The results show that PS-OCT parameters such as phase retardation and scattering coefficients are significant in detecting ovarian cancer. The phase retardation images of normal and cancerous ovarian tissue from conventional OCT and phase retardation is given in Fig. 7. Since the phase retardation of normal and malignant express varying features, combining it with the calculated scattering coefficient is expected to be an efficient method in determining the disease [58]. These parameters extracted from ovarian samples are fed into the logistic model for training to achieve the automated classification of ovarian tissues as benign and malignant. Hence, a multiple parameter approach used for ovarian tissue characterization was more efficient [59].

4.6 Prostate Cancer

Prostate cancer is one of the most common organ cancers diagnosed in males by prostate-specific antigen (PSA) testing. Over diagnosis and treatment of the patients could be caused by PSA testing [60]. Prostate biopsy procedures are a potential source for diagnosis, however, challenges such as lack of standard isolation and purification techniques, labour-intensive, contamination risks and sampling errors may lead to misdiagnosis [61, 62]. Therefore, adapting to an alternative approach is essential to treat prostate cancer, and one such technique involves employing OCT for imaging of tissues. Swaan et al. [63] presented a study to assess the feasibility of focal imaging with confocal laser endomicroscopy (CLE) and needle-based OCT for differentiating normal and cancerous prostate tissues on both qualitative and quantitative basis, which includes visualization and analysis of tissues, tumour grade, and real-time architecture. This approach provided high-resolution imaging in real-time and characteristics of prostate cancer in association with transrectal ultrasound fusion-guided biopsy processes providing keen insight into the feasibility and of CLE and OCT for real-time analysis of prostate cancer.

Mullar et al. [64] acquired datasets of 106 needle-based 3D-OCT from 20 prostates, and the OCT images were grouped based on histology and precise matching, blind assessment of the same was carried out by two reviewers calculating the sensitivity and specificity of the detected malignancy, which was found to be significantly different based on quality. It was observed that needle-based OCT was reliable in discriminating between benign glands and regular, fat or cystic atrophy (Fig. 8). Quantitative assessment by Kruskal-Wallis test also

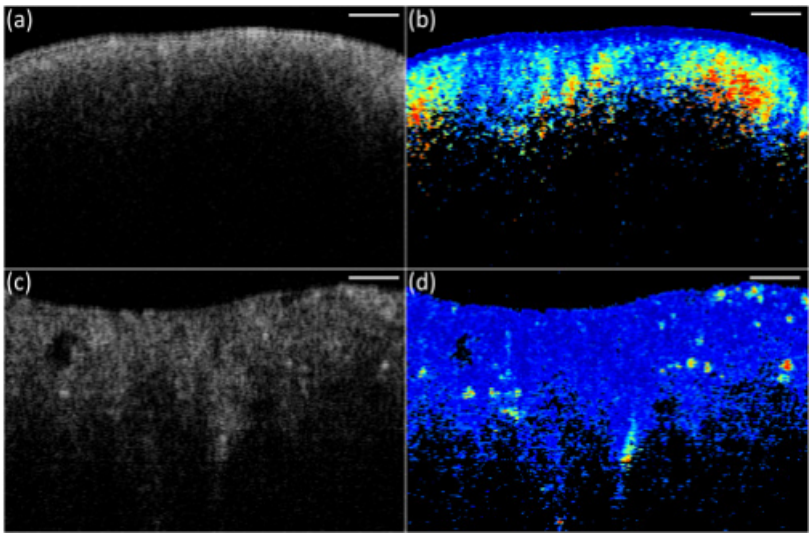


Fig. 7 (a, c) Conventional OCT and (b, d) phase retardation images from (a, b) normal and (c, d) malignant ovarian tissue. Scale bar: 0.5 mm. Adapted with permission from [59] © The Optical Society.

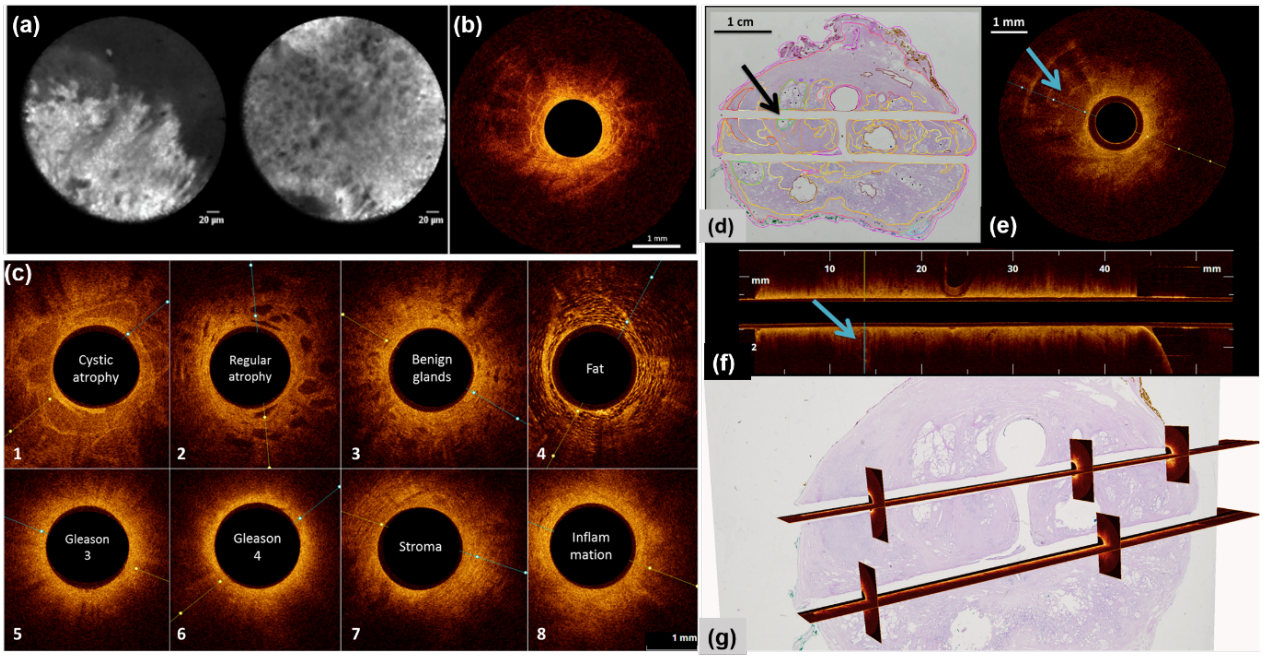


Fig. 8 (a) CLE images of *ex vivo* prostate tissue with probe soaked in fluorescein solution, (b) OCT image of the fixated *ex vivo* prostate tissue, (c) histological features seen in the OCT images, (d-g) correlation of OCT and histology where (d) depicts the tissue types in different colours indicating atrophic cyst by a black arrow, (e) OCT scan of the atrophic cyst, (f) longitudinal cross-section of the OCT scan and (g) one-to-one correlation of OCT images and histopathology. The Figures are adapted with kind permission from [63, 64].

produced a significant difference between stroma, inflammation, Gleason 3, and Gleason 4 confirming the correlation of histopathology and OCT (Fig. 8). Precise matching of the images enabled differentiating the most histological tissues in the prostate by their unique pattern obtained by OCT. Recent advancements of micro-optical coherence tomography (μOCT) can generate depth-resolved tissue images with 1 μm resolution. Cellular-level contrast in prostate specimens was presented by the μOCT optical images, which helps in differentiating and diagnosing the pathologies. Specimens obtained from surgical resections were subjected μOCT imaging *ex vivo* and observed features correlated with the histological findings, suggesting that μOCT could resolve benign and neoplastic prostate associated cellular characteristics. μOCT can be implemented in a small-diameter probe which suggests that μOCT imaging may be used for needle-based virtual biopsy of the prostate [65].

Three pathologists carried out the pathological evaluation of full-field OCT (FF-OCT) diagnostic accuracy in the detection of cancer on prostate biopsy of 38 patients by determining sensitivity, specificity,

positive and negative prediction values. The observations of pathologists were on substantial agreement with over 72% accuracy. It was concluded that FF-OCT imaging of prostate biopsy would provide over 80% diagnostic accuracy with good reliability [66]. A customized tool was developed to validate OCT in the differentiation of prostate cancer by processing radical prostatectomy specimens to improve OCT pullback measurements. This is essential in the critical validation of OCT imaging studies by correlating histology and studying solid tissues such as lung, breast, ovary, kidney, and liver. Improvement in the efficacy of OCT in cancer detection and staging in solid organs was achieved [67]. Therefore, this non-invasive, real-time imaging approach has proven effective in detecting and differentiation cancerous prostate.

Table 3 Diagnostic summary.

Cancer types	**Types of OCT**	**Diagnostic summary**	**Reference**
Colorectal cancer	Integrated multimodal OCT and NIR fluorescence imaging system	OCT endoscopy helps visualize the microanatomy of the subsurface layer structures with microscopic detail and NIR fluorescence imaging can be used to identify the suspect lesions rapidly	[13]
	Multimodal FD-OCT with Raman spectroscopy	The multimodal optical approach discriminated between colonic adenocarcinoma and normal colon with 97% sensitivity and specificity	[14]
	Co-registered OCT and fluorescence molecular imaging (FMI) system	This system enables simultaneous imaging of tissue morphology and molecular information at high resolution over 2–3 mm field-of-view, and will have potential applications in small animal imaging and clinical imaging	[18]
Breast cancer	Handheld surgical OCT imaging probe	The *ex vivo* images were compared with standard post-operative histopathology to yield sensitivity of 91.7% [95% confidence interval (CI), 62.5%–100%] and specificity of 92.1% (95% CI, 78.4%–98%)	[20]
	Optical coherence microelastography (OCME)	OCT readily distinguishes mature stroma and tumour from adipose in tissue, microelastograms exhibit high contrast between tissues with similar optical backscattering properties. Together, OCME is shown to enable ready visualization of features such as ducts, lobules, microcysts, blood vessels, and arterioles and to identify invasive tumour through distinctive patterns	[25]
	Optical coherence elastography (OCE)	OCE imaging ensures much higher contrast between different tissue types in comparison with both structural OCT images (including PS-OCT) and conventionally used elastographic techniques	[26]
	FF-OCT and dynamic cell imaging (DCI)	FFOCT has been used to differentiate benign and malignant breast tissues and provides a platform for diagnostic decision making. Its sensitivity and specificity both are roughly over 90%. DCI is used to visualize tissues on a cellular scale with metabolic features coupled with the morphologic imaging of FFOCT	[27]
	PS-OCT	In the study, healthy fibro-adipose tissue, healthy stroma, and invasive ductal carcinoma can be differentiated with an accuracy of 89.4%	[28]

	SS-OCT	The SVM based automated volumetric analysis of normal and breast cancer tissue classifies the cancerous tissue with sensitivity, specificity, and accuracy of 91.56%, 93.86%, and 92.71% respectively	[29]
	OCT and OCM	The system enabled 4-μm axial resolution (OCT and OCM) with 14-μm (OCT) and 2-μm (OCM) transverse resolutions, respectively. OCT and OCM provide complimentary information about tissue microstructure, thus showing distinctive patterns for adipose tissue, fibrous stroma, breast lobules and ducts, cysts and micro-cysts, as well as in situ and invasive carcinomas	[30]
	OCT	The developed multi-level ensemble classifier attained the average sensitivity, specificity, accuracy and Mathew correlation coefficient is 0.954%, 0.93%, 94.35%, and 0.887% in classifying normal and cancerous breast tissue	[31]
		The *ex vivo* study with OCT showed significant difference in the hair structure before and after chemotherapy due to reduction of hair shaft calibre and increase of form factor in regrowing hair	[32]
	FF-OCT	Using FF-OCT images, two breast pathologists were able to distinguish normal/benign tissue from lesion with a sensitivity of 94% and 90%, and specificity of 75% and 79% respectively	[49]
Skin cancer	OCT and PS-OCT	OCT and PS-OCT analysis showed 79% to 94% sensitivity and 85% to 96% specificity in differentiating normal skin from non-melanoma skin cancer lesions	[33]
	SS-OCT	Among the classifiers, Linear SVM (LSVM) yielded the optimum result with an accuracy rate of 80.9%, specificity of 80.5% and sensitivity of 81.9% for BCC classification. With quadratic SVM (QSVM) an accuracy rate of 87.2%, specificity of 87.3% and sensitivity of 87% were obtained for SCC classifications. QSVM also provided satisfying results, 80.5% accuracy for BCC classification	[34]
		In the study, clinically identified melanoma to non-melanoma area showed a meaningful difference. Further, classification of sample using Gaussian SVM provided highest classification accuracy of 98% with other evaluation matrix	[36]
	Multi-beam OCT	This study showed that it is possible to distinguish between the different non melanoma skin cancers by using OCT	[35]
	Multi-beam-FD-SS OCT	Abrupt changes in architectures of the dermal and epidermal layers in the GCT lesion were observed. These architectural changes were not observed in healthy skin	[37]
	Vivosight OCT Scanner	The depth of superficial basal cell carcinoma (BCC) lesions (<1 mm) can be measured accurately using OCT. A low-strength OCT signal at the periphery of the cell nests seen in superficial and nodular BCC is identified as corresponding to cellular palisading. A weak inverse linear correlation (r^2=0.3) is found between the optical attenuation coefficient measured on OCT and the nuclear-cytoplasmic ratio (N/C) of cells determined from histology	[40]

		The specificity increased significantly from 28.6% by clinical assessment to 54.3% using dermoscopy and to 75.3% with the addition of OCT. The accuracy of diagnosis for all lesions increased from 65.8% with clinical evaluation to 76.2% following additional dermoscopy and to 87.4% with the addition of OCT	[42]
	OCT	OCT could identify superficial BCC and acute keratosis before treatment. Monitoring during imiquimod treatment revealed impaired image quality most likely caused by inflammation, crusting and ulceration	[41]
	PS-OCT	The SVM classifier achieved 95.4% sensitivity in the classification of basal cell carcinoma (BCC) from normal samples	[43]
	FD-OCT	Diagnostic performance of OCT did not depend on the lesion's anatomical location. Good OCT image quality was correlated with improved diagnostic performance, but diagnostic performance for lesions with mediocre image quality was still better than by clinical and dermoscopic examination	[44]
		FD-OCT with a new depiction for horizontal and vertical imaging modes offers additional information in the diagnosis of BCC, especially in nodular BCC, and enhances the possibility of the evaluation of morphologic tumour features	[45]
Brain cancer	CP-OCT	The diagnostic threshold of attenuation coefficient was 8.2 mm^{-1} for patients of all grades (sensitivity/specificity: 95.6%/81.3%, respectively) and 6.1 mm^{-1} for low-grade patients (sensitivity/specificity: 100%/100%, respectively)	[52]
		Visual assessment of CP OCT images enables tumorous and non-tumorous tissues is distinguished based on differentiation between tumorous tissue and white matter. The diagnostic accuracy for the same is 87–88%	[55]
	FF-OCT	FF-OCT captures slices of tissue samples at 1 μm axial and lateral resolution in 3D to a penetration depth of around 200 μm	[53]
	SS-OCT	The technique exhibited comparable 100% sensitivity and 40–50% greater specificity in detecting the cancer	[54]
Ovarian cancer	FD-PS OCT	Linear regression analysis showed that this parameter was positively correlated (R = 0.74) with collagen content, which was associated with the development of ovarian tissue malignancy. With 33 ovaries training dataset the logistic model produced 100% sensitivity and specificity whereas, model validation with new dataset showed 100% sensitivity and 83.3% specificity	[58]
	PS-OCT	A specificity of 100% and a sensitivity of 86% were achieved by using estimated scattering coefficient alone; and a specificity of 100% and a sensitivity of 43% were obtained by using phase retardation alone. However, a superior specificity of 100% and sensitivity of 100% were achieved if these two parameters were used together for classifying normal and malignant ovaries	[59]

Prostate cancer	Needle based OCT	This study will provide insight into the feasibility and tissue-specific characteristics of confocal laser endomicroscopy and optical coherence tomography for real-time optical analysis of prostate cancer	[63]
		OCT can reliably differentiate between fat, cystic, and regular atrophy and benign glands. In blind assessment of OCT images, the overall sensitivity and specificity for malignancy detection was 79% and 88% for Reviewer 1 and 88% and 81% for Reviewer 2	[64]
	μOCT	From the system, high-quality image data were obtained at a penetration depth up to 500 μm. This technique is capable of resolving many of the architectural and cellular features associated with benign and neoplastic prostate	[65]
	FF-OCT	FF-OCT of prostate biopsy cores may provide a diagnostic accuracy greater than 80%, with a good reliability and high negative predictive values.	[66]
Lung cancer	FD-OCT	Permeability coefficients showed statistically significant differences between benign lung granulomatosis and normal tissues	[72]
	PS-OCT	The sensitivity and specificity of using OCT in diagnosing different types of lung cancer were in the range of 80–100%	[73]

4.7 Lung Cancer

Lung cancer is the most common cause of cancer-related deaths in men and women around the globe. High-resolution imaging technology is required to have an insight into pathophysiology and diagnose lung cancer and other pulmonary related diseases. Currently, the two imaging techniques available are OCT and CLE. OCT can be used to detect malignant cells in the lung parenchyma, central airways, pleura, and lymph nodes. By evaluating the malignant area in airway walls using OCT, the treatment including airway remodelling is possible [68]. *In vivo* endoscopic OCT can be used to produce real-time cross-sectional images of living tissues [69]. Michel et al. [70] was the first to report the use of OCT to differentiate malignant endobronchial from normal endobronchial mucosa. OCT scans were obtained after the performance on both malignant and normal endobronchial mucosa. The whole procedure was completed in around 30 min. OCT scan of endobronchial mucosa displayed malignancy along with loss of microstructures and optical fractures of tissues. The diagnostic accuracy of OCT provided a sensitivity of 100% and specificity of 80%, 70% when considering layer thickness and the attenuation coefficient, respectively. Wessels et al. [71] presented that qualitative and quantitative OCT imaging can distinguish between benign and (pre)malignant vulvar tissue.

Wei et al. [72] evaluated the effects of diffusion of analyte mediated by ultrasound on the permeability of benign, normal, and malignant lung tissues *in vitro*. It was also used to determine effective sonophoretic (SP) delivery combined with optical clearing agents (OCAs) to distinguish between normal and diseased tissues. FD-OCT was used to determine the permeability coefficient of SP combined OCAs method. The result of permeability coefficients showed statistically significant differences between benign lung granulomatosis and normal tissues. Ultrasound mediated OCAs method combined with FD-OCT suggested a potential diagnosis and detection of microstructure change in human lung tissues. Hariri et al. [73] proved that OCT could not replace histopathology but could be used in place of biopsies to diagnose lung cancer. The sensitivity and specificity of using OCT in diagnosing different types of lung cancer were in the range of 80–100% (as represented in Figs. 1–3 of Ref. [73]). Biopsies must include enough tumour for the diagnosis with the advancement in personalized medicine. However, diagnosis may delay due to unplanned biopsy of tumour-associated fibrosis, also affecting the tumour yield. Differentiating tumour from tumour-associated fibrosis during biopsy could remarkably elevate tumour yield. Hariri et al. [74] demonstrated that PS-OCT could effectively be used to identify tumours from fibrosis taken from lung sample and thus can be used for *in vivo* intraprocedural tissue sampling or *ex vivo* rapid biopsy assessment to obtain increased tumour yield for the diagnosis of cancer.

Jain et al. [75] presented a study in which FF-OCT was used to produce high-resolution lung tissue images. It showed to have potential in identifying tumours from non-neoplastic lung tissue. Distinguishing features such as lung collapse and smoker's macrophages were also identified in the sample tissues. Another study conducted by d'Hooghe et al. [76] reported OCT-based imaging of airway walls layers both *in vivo* and *ex vivo*. It was an

accurate imaging technique for quantifying and identifying airway wall layers and has a potential airway remodelling in lung diseases. This intraoperative, non-invasive, and real-time imaging technique has the potential in detecting different types of lung cancer such as poorly differentiated carcinoma, squamous cell carcinoma and adenocarcinoma.

5 Conclusion

OCT is an effective and convenient tool for various bio-clinical fields, including the characterization and diagnosis of different diseases. The various studies indicate that the technique, when combined with other imaging modalities, show an enhanced effect. Simultaneous assessment of images in PS-OCT is more effective in a detailed understanding of the molecule orientation [10]. In this review, we discuss the importance of detection of several cancers. However, this technique can also be used in investigating other diseases. The integration of adaptive optics in OCT can image deeper regions in tissue by overcoming the wavefront distortion of the sample as well as optics used.

Cancer cell growth in the tissue causes variation in tissue features such as shape and size of microstructures, density, etc. And OCT is one such technique to identify such minute changes associated with tissue microstructures. However, they may fail to differentiate similar morphological structures, which in turn decreases the output accuracy. In this regard, the incorporation of a proper post-processing and quantitative analysis technique plays an important role in differentiating benign and malignant tissue with high classification accuracy [32, 34]. The quality of images obtained by OCT can be enriched by deducing the properties of the object numerically with signal processing. Further analysis will enhance the details obtained depending on the data quality. Signal processing ensures maximum use of the data available by decreasing the noise and confirming accurate image formation. It can be beneficial in reducing noise, improving resolution through deconvolution, reducing speckle, correcting for material dispersion and OCT system imperfections, and de-blurring the defocusing effects outside of the depth-of-field of the OCT instrument [48]. Later, different optical, textural features extracted from these pre-processed images are used in training the statistical algorithms to achieve tissue classification [32, 34].

6 Future prospects of OCT in oncological diagnosis and treatment

The use of OCT at every step in oncology appears to be very promising, which will bring a major change in medical practice in the best way in the future. Obtaining optical access to the tissue site is currently a major challenge, yet the use of OCT appears to greater potentials with higher resolutions than other techniques currently used in oncological imaging. Where conventional biopsy is not effective, OCT can be used for guided biopsy, in many situations, biopsy is associated with many complications, so we can play the role of OCT as a tissue specific differentiation guide. OCT is among the best techniques that can assist in intraoperative imaging of various kind of cancer and other disease in the operation room by providing specific and real-time feedback to surgeons during specialized and complex surgeries. OCT can be used to monitor tumour responses to various types of cancer treatments such as photodynamic therapy, radiotherapy, thermotherapy, cryotherapy, and chemotherapy and the tissue changes that occur in them. OCT in oncopathology will be presented with strong demonstrations, with an emphasis on *ex vivo* and *in vivo* cancer diagnosis applications, given the development and broad potential. Currently, the utility of this technology can be seen in the criteria-based market, given the availability of various commercial OCT imaging systems and OCT probes, OCT in the field of oncology appears to be full of immense potential which proves to be an important milestone.

Compliance with ethical standards

The cited reference papers have ethical clearance for conducting the experiments.

Disclosures

All authors declare that there is no conflict of interests in this paper.

Acknowledgments

We thank the Department of Science and Technology (DST), Government of India, for the financial support (project number: DST/INT/Thai/P-10/2019 and DST/INT/BLG/P-3/2019). The authors thank Manipal School of Life Sciences (MSLS), Manipal Academy of Higher Education (MAHE), Manipal, Karnataka, India for providing the infrastructure and facilities.

References

1. M. E. Brezinski, G. J. Tearney, B. E. Bouma, J. A. Izatt, M. R. Hee, E. A. Swanson, J. F. Southern, and F. G. Fujimoto, "Optical coherence tomography for optical biopsy: properties and demonstration of vascular pathology," Circulation 93(6), 1206–1213 (1996).

2. P. A. Valdés, D. W. Roberts, F. K. Lu, and A. Golby, "Optical technologies for intraoperative neurosurgical guidance," Neurosurgical Focus 40(3), E8 (2016).
3. W. Drexler, U. Morgner, F. X. Kärtner, C. Pitris, S. A. Boppart, X. D. Li, E. P. Ippen, and J. G. Fujimoto, "In vivo ultrahigh-resolution optical coherence tomography," Optics Letters 24(17), 1221–1223 (1999).
4. J. G. Fujimoto, M. E. Brezinski, G. J. Tearney, S. A. Boppart, B. Bouma, M. R. Hee, J. F. Southern, and E. A. Swanson, "Optical biopsy and imaging using optical coherence tomography," Nature Medicine 1(9), 970–972 (1995).
5. J. G. Fujimoto, C. Pitris, S. A. Boppart, and M. E. Brezinski, "Optical coherence tomography: an emerging technology for biomedical imaging and optical biopsy," Neoplasia 2(1-2), 9–25 (2000).
6. W. Drexler, J. G. Fujimoto, "State-of-the-art retinal optical coherence tomography," Progress in Retinal and Eye Research 27(1), 45–88 (2008).
7. T. Klein, R. Huber, "High-speed OCT light sources and systems," Biomedical Optics Express 8(2), 828–859 (2017).
8. J. F. de Boer, C. K. Hitzenberger, and Y. Yasuno, "Polarization sensitive optical coherence tomography - a review," Biomedical Optics Express 8(3), 1838–1873 (2017).
9. A. Dubois, L. Vabre, A. C. Boccara, and E. Beaurepaire, "High-resolution full-field optical coherence tomography with a Linnik microscope," Applied Optics 41(4), 805–812 (2002).
10. S. R. Chinn, E. A. Swanson, and J. G. Fujimoto, "Optical coherence tomography using a frequency-tunable optical source," Optics Letters 22(5), 340–342 (1997).
11. J. P. Kolb, T. Pfeiffer, M. Eibl, H. Hakert, and R. Huber, "High-resolution retinal swept source optical coherence tomography with an ultra-wideband Fourier-domain mode-locked laser at MHz A-scan rates," Biomedical Optics Express 9(1), 120–130 (2017).
12. S. Yun, G. Tearney, J. de Boer, N. Iftimia, and B. Bouma, "High-speed optical frequency-domain imaging," Optics Express 11(22), 2953–2963 (2003).
13. Y. Li, Z. Zhu, J. J. Chen, J. C. Jing, C. H. Sun, S. Kim, P. S. Chung, and Z. Chen, "Multimodal endoscopy for colorectal cancer detection by optical coherence tomography and near-infrared fluorescence imaging," Biomedical Optics Express 10(5), 2419–2429 (2019).
14. P. C. Ashok, B. B. Praveen, N. Bellini, A. Riches, K. Dholakia, and C. S. Herrington, "Multi-modal approach using Raman spectroscopy and optical coherence tomography for the discrimination of colonic adenocarcinoma from normal colon," Biomedical Optics Express 4(10), 2179–2186 (2013).
15. N. Stone, C. Kendall, J. Smith, P. Crow, and H. Barr, "Raman spectroscopy for identification of epithelial cancers," Faraday Discuss 126, 141–157 (2004).
16. N. Krstajić, C. T. Brown, K. Dholakia, and M. E. Giardini, "Tissue surface as the reference arm in Fourier domain optical coherence tomography," Journal of Biomedical Optics 17(7), 071305 (2012).
17. D. E. Fleischer, B. F. Overholt, V. K. Sharma, A. Reymunde, M. B. Kimmey, R. Chuttani, K. J. Chang, R. Muthasamy, C. J. Lightdale, N. Santiago, and D. K. Pleskow, "Endoscopic radiofrequency ablation for Barrett's esophagus: 5-year outcomes from a prospective multicenter trial," Endoscopy 42(10), 781–789 (2010).
18. S. Yuan, C. A. Roney, J. Wierwille, C. W. Chen, B. Xu, G. Griffiths, J. Jiang, H. Ma, A. Cable, R. M. Summers, and Y. Chen, "Co-registered optical coherence tomography and fluorescence molecular imaging for simultaneous morphological and molecular imaging," Physics in Medicine & Biology 55(1), 191 (2010).
19. E. S. Hwang, D. Y. Lichtensztajn, S. L. Gomez, B. Fowble, and C. A. Clarke, "Survival after lumpectomy and mastectomy for early stage invasive breast cancer: the effect of age and hormone receptor status," Cancer 119(7), 1402–1411 (2013).
20. S. J. Erickson-Bhatt, R. M. Nolan, N. D. Shemonski, S. G. Adie, J. Putney, D. Darga, D. T. McCormick, A. J. Cittadine, A. M. Zysk, M. Marjanovic, and E. J. Chaney, "Real-time imaging of the resection bed using a handheld probe to reduce incidence of microscopic positive margins in cancer surgery," Cancer Research 75(18), 3706–3712 (2015).
21. J. Wang, Y. Xu, and S. A. Boppart, "Review of optical coherence tomography in oncology," Journal of Biomedical Optics 22(12), 121711 (2017).
22. K. H. Allison, "Molecular pathology of breast cancer: what a pathologist needs to know," American Journal of Clinical pathology 138(6), 770–780 (2012).
23. O. A. Catalano, G. L. Horn, A. Signore, C. Iannace, M. Lepore, M. Vangel, A. Luongo, M. Catalano, C. Lehman, M. Salvatore, and A. Soricelli, "PET/MR in invasive ductal breast cancer: correlation between imaging markers and histological phenotype," British Journal of Cancer 116(7), 893–902 (2017).
24. B. F. Kennedy, S. H. Koh, R. A. McLaughlin, K. M. Kennedy, P. R. Munro, and D. D. Sampson, "Strain estimation in phase-sensitive optical coherence elastography," Biomedical Optics Express 3(8), 1865–1879 (2012).
25. B. F. Kennedy, R. A. McLaughlin, K. M. Kennedy, L. Chin, P. Wijesinghe, A. Curatolo, A. Tien, M. Ronald, B. Latham, C. M. Saunders, and D. D. Sampson, "Investigation of optical coherence microelastography as a method to visualize cancers in human breast tissue," Cancer Research 75(16), 3236–3245 (2015).
26. E. V. Gubarkova, A. A. Sovetsky, V. Y. Zaitsev, A. L. Matveyev, D. A. Vorontsov, M. A. Sirotkina, L. A. Matveev, A. A. Plekhanov, N. P. Pavlova, S. S. Kuznetsov, and A. Y. Vorontsov, "OCT-elastography-based optical biopsy for

breast cancer delineation and express assessment of morphological/molecular subtypes," Biomedical Optics Express 10(5), 2244–2263 (2019).
27. H. Yang, S. Zhang, P. Liu, L. Cheng, F. Tong, H. Liu, S. Wang, M. Liu, C. Wang, Y. Peng, and F. Xie "Use of high-resolution full-field optical coherence tomography and dynamic cell imaging for rapid intraoperative diagnosis during breast cancer surgery," Cancer 126, 3847–3856 (2020).
28. J. Wang, Y. Xu, K. J. Mesa, F. A. South, E. J. Chaney, D. R. Spillman, R. Barkalifa, M. Marjanovic, P. S. Carney, A. M. Higham, and Z. G. Liu, "Complementary use of polarization-sensitive and standard OCT metrics for enhanced intraoperative differentiation of breast cancer," Biomedical Optics Express 9(12), 6519–6528 (2018).
29. A. Butola, A. Ahmad, V. Dubey, V. Srivastava, D. Qaiser, A. Srivastava, P. Senthilkumaran, and D. S. Mehta, "Volumetric analysis of breast cancer tissues using machine learning and swept-source optical coherence tomography," Applied Optics 58(5), A135–A141 (2019).
30. C. Zhou, D. W. Cohen, Y. Wang, H. C. Lee, A. E. Mondelblatt, T. H. Tsai, A. D. Aguirre, J. G. Fujimoto, and J. L. Connolly, "Integrated optical coherence tomography and microscopy for ex vivo multiscale evaluation of human breast tissues," Cancer Research 70(24), 10071–10079 (2010).
31. K. Dubey, N. Singla, A. Butola, A. Lathe, D. Quaiser, A. Srivastava, D.S. Mehta, and V. Srivastava, "Ensemble classifier for improve diagnosis of the breast cancer using optical coherence tomography and machine learning," Laser Physics Letters 16(2), 025602 (2019).
32. J. Lindner, K. Hillmann, U. Blume-Peytavi, J. Lademann, A. Lux, A. Stroux, A. Schneider, and N. Garcia Bartels, "Hair shaft abnormalities after chemotherapy and tamoxifen therapy in patients with breast cancer evaluated by optical coherence tomography," British Journal of Dermatology 167(6), 1272–1278 (2012).
33. M. Mogensen, T. M. Joergensen, B. M. Nürnberg, H. A. Morsy, J. B. Thomsen, L. Thrane, and G. B. Jemec, "Assessment of optical coherence tomography imaging in the diagnosis of non-melanoma skin cancer and benign lesions versus normal skin: observer-blinded evaluation by dermatologists and pathologists," Dermatologic Surgery 35(6), 965–972 (2009).
34. S. Adabi, M. Hosseinzadeh, S. Noei, S. Conforto, S. Daveluy, A. Clayton, D. Mehregan, and M. Nasiriavanaki, "Universal in vivo textural model for human skin based on optical coherence tomograms," Scientific Reports 7(1), 17912 (2017).
35. S. Batz, C. Wahrlich, A. Alawi, M. Ulrich, and J. Lademann, "Differentiation of different nonmelanoma skin cancer types using OCT," Skin Pharmacology and Physiology 31(6), 238–245 (2018).
36. Z. Turani, E. Fatemizadeh, T. Blumetti, S. Daveluy, A. F. Moraes, W. Chen, D. Mehregan, P. E. Andersen, and M. Nasiriavanaki, "Optical radiomic signatures derived from optical coherence tomography images improve identification of melanoma," Cancer Research 79(8), 2021–2030 (2019).
37. D. Tes, A. Aber, M. Zafar, L. Horton, A. Fotouhi, Q. Xu, A. Moiin, A. D. Thompson, T. C. Moraes Pinto Blumetti, S. Daveluy, and W. Chen, "Granular cell tumor imaging using optical coherence tomography," Biomedical Engineering and Computational Biology 9, 1179597218790250 (2018).
38. A. L. Agero, K. J. Busam, C. Benvenuto-Andrade, A. Scope, M. Gill, A. A Marghoob, S. González, and A. C. Halpern, "Reflectance confocal microscopy of pigmented basal cell carcinoma," Journal of the American Academy of Dermatology 54(4), 638–643 (2006).
39. S. Seidenari, F. Arginelli, S. Bassoli, J. Cautela, A.M. Cesinaro, M. Guanti, D. Guardoli, C. Magnoni, M. Manfredini, G. Ponti, and K. König, "Diagnosis of BCC by multiphoton laser tomography," Skin Research and Technology 19(1), e297–e304 (2013).
40. A. J. Coleman, T. J. Richardson, G. Orchard, A. Uddin, M. J. Choi, and K. E. Lacy, "Histological correlates of optical coherence tomography in non-melanoma skin cancer," Skin Research and Technology 19(1), e10–e19 (2013).
41. C. A. Banzhaf, L. Themstrup, H. C. Ring, M. Mogensen, and G. B. Jemec, "Optical coherence tomography imaging of non-melanoma skin cancer undergoing imiquimod therapy," Skin Research and Technology 20(2), 170–176 (2014).
42. M. Ulrich, T. von Braunmuehl, H. Kurzen, T. Dirschka, C. Kellner, E. Sattler, C. Berking, J. Welzel, and U. Reinhold, "The sensitivity and specificity of optical coherence tomography for the assisted diagnosis of nonpigmented basal cell carcinoma: an observational study," British Journal of Dermatology 173(2), 428–435 (2015).
43. T. Marvdashti, L. Duan, S. Z. Aasi, J. Y. Tang, and A. K. Bowden, "Classification of basal cell carcinoma in human skin using machine learning and quantitative features captured by polarization sensitive optical coherence tomography," Biomedical Optics Express 7(9), 3721–3735 (2016).
44. J. Holmes, T. von Braunmühl, C. Berking, E. Sattler, M. Ulrich, U. Reinhold, H. Kurzen, T. Dirschka, C. Kellner, S. Schuh, and J. Welzel, "Optical coherence tomography of basal cell carcinoma: influence of location, subtype, observer variability and image quality on diagnostic performance," British Journal of Dermatology 178(5), 1102–1110 (2018).
45. T. von Braunmühl, D. Hartmann, J. K. Tietze, D. Cekovic, C. Kunte, T. Ruzicka, C. Berking, and E. C. Sattler, "Morphologic features of basal cell carcinoma using the en-face mode in frequency domain optical coherence tomography," Journal of the European Academy of Dermatology and Venereology 30(11), 1919–1925 (2016).

46. J. Gogas, C. Markopoulos, E. Kouskos, H. Gogas, D. Mantas, Z. Antonopoulou, and K. Kontzoglou, "Granular cell tumor of the breast: a rare lesion resembling breast cancer," European Journal of Gynaecological Oncology 23(4), 333–334 (2002).
47. M. Lacroix, D. Abi-Said, D. R. Fourney, Z. L. Gokaslan, W. Shi, F. DeMonte, F. F. Lang, I. E. McCutcheon, S. J. Hassenbusch, E. Holland, and K. Hess, "A multivariate analysis of 416 patients with glioblastoma multiforme: prognosis, extent of resection, and survival," Journal of Neurosurgery 95(2), 190–198 (2001).
48. N. Sanai, M. Y. Polley, M. W. McDermott, A. T. Parsa, and M. S. Berger, "An extent of resection threshold for newly diagnosed glioblastomas," Journal of Neurosurgery 115(1), 3–8 (2011).
49. O. Assayag, M. Antoine, B. Sigal-Zafrani, M. Riben, F. Harms, A. Burcheri, K. Grieve, E. Dalimier, B. Le Conte de Poly, and C. Boccara, "Large field, high resolution full-field optical coherence tomography: a pre-clinical study of human breast tissue and cancer assessment," Technology in Cancer Research & Treatment 13(5), 455–468 (2014).
50. T. Alice, N. Georges, "Medulloblastoma: optimizing care with a multidisciplinary approach," Journal of Multidisciplinary Healthcare 12, 335–347 (2019).
51. F. J. van der Meer, D. J. Faber, D. M. Baraznji Sassoon, M. C. Aalders, G. Pasterkamp, and T. G. van Leeuwen, "Localized measurement of optical attenuation coefficients of atherosclerotic plaque constituents by quantitative optical coherence tomography," IEEE Transactions on Medical Imaging 24(10), 1369–1376 (2005).
52. K. S. Yashin, E. B. Kiseleva, A. A. Moiseev, S. S. Kuznetsov, L. B. Timofeeva, N. P. Pavlova, G. V. Gelikonov, I. A. Medyanik, L. Y. Kravets, E. V. Zagaynova, and N. D. Gladkova, "Quantitative nontumorous and tumorous human brain tissue assessment using microstructural co- and cross-polarized optical coherence tomography," Scientific Reports 9(1), 2024 (2019).
53. O. Assayag, K. Grieve, B. Devaux, F. Harms, J. Pallud, F. Chretien, C. Boccara, and P. Varlet, "Imaging of non-tumorous and tumorous human brain tissues with full-field optical coherence tomography," NeuroImage: Clinical 2, 549–557 (2013).
54. C. Kut, K. L. Chaichana, J. Xi, S. M. Raza, X. Ye, E. R. McVeigh, F. J. Rodriguez, A. Quiñones-Hinojosa, and X. Li, "Detection of human brain cancer infiltration ex vivo and in vivo using quantitative optical coherence tomography," Science Translational Medicine 7(292), 292ra100-292ra100 (2015).
55. K. S. Yashin, E. B. Kiseleva, E. V. Gubarkova, A. A. Moiseev, S. S. Kuznetsov, P. A. Shilyagin, G. V. Gelikonov, I. A. Medyanik, L. Y. Kravets, A. A. Potapov, and E. V. Zagaynova, "Cross-polarization optical coherence tomography for brain tumor imaging," Frontiers in Oncology 9, 201 (2019).
56. T. R. Rebbeck, H. T. Lynch, S. L. Neuhausen, S. A. Narod, L. Van't Veer, J. E. Garber, G. Evans, C. Isaacs, M. B. Daly, E. Matloff, and O. I . Olopade, "Prophylactic oophorectomy in carriers of BRCA1 or BRCA2 mutations," New England Journal of Medicine 346(21), 1616–1622 (2002).
57. C. St-Pierre, W. J. Madore, E. De Montigny, D. Trudel, C. Boudoux, N. Godbout, A. M. Mes-Masson, K. Rahimi, and F. Leblond, "Dimension reduction technique using a multilayered descriptor for high-precision classification of ovarian cancer tissue using optical coherence tomography: a feasibility study," Journal of Medical Imaging 4(4), 041306 (2017).
58. T. Wang, Y. Yang, and Q. Zhu, "A three-parameter logistic model to characterize ovarian tissue using polarization-sensitive optical coherence tomography," Biomedical Optics Express 4(5), 772–777 (2013).
59. Y. Yang, T. Wang, X. Wang, M. Sanders, M. Brewer, and Q. Zhu, "Quantitative analysis of estimated scattering coefficient and phase retardation for ovarian tissue characterization," Biomedical Optics Express, 3(7) 1548–1556 (2012).
60. D. L. Marks, T. S. Ralston, and S. A. Boppart "Data analysis and signal postprocessing for Optical Coherence Tomography," In Optical Coherence Tomography, W. Drexler, J. G. Fujimoto (eds.), Springer, Berlin, Heidelberg, 405–426 (2008).
61. J. Liu, Y. Li, D. Yang, C. Yang, and L. Mao, "Current state of biomarkers for the diagnosis and assessment of treatment efficacy of prostate cancer," Discovery Medicine 27(150), 235–243 (2019).
62. J. Wang, J. Ni, J. Beretov, J. Thompson, P. Graham, and Y. Li, "Exosomal microRNAs as liquid biopsy biomarkers in prostate cancer," Critical Reviews in Oncology/Hematology 145, 102860 (2020).
63. A. Swaan, C. K. Mannaerts, M. J. Scheltema, J. A. Nieuwenhuijzen, C. D. Savci-Heijink, J. J. de la Rosette, R. J. Van Moorselaar, T. G. Van Leeuwen, T. M. De Reijke, and D. M. De Bruin, "Confocal laser endomicroscopy and optical coherence tomography for the diagnosis of prostate cancer: a needle-based, in vivo feasibility study protocol (IDEAL phase 2A)," JMIR Research Protocols 7(5), e132 (2018).
64. B. G. Muller, R. van Kollenburg, A. Swaan, E. Zwartkruis, M. J. Brandt, L. S. Wilk, M. Almasian, A. W. Schreurs, D. J. Faber, L. R. Rozendaal, and A. N. Vis, "Needle-based optical coherence tomography for the detection of prostate cancer: a visual and quantitative analysis in 20 patients," Journal of Biomedical Optics 23(8), 086001 (2018).
65. J. A. Gardecki, K. Singh, C. L. Wu, and G. J. Tearney, "Imaging the human prostate gland using 1-μm-resolution optical coherence tomography," Archives of Pathology & Laboratory Medicine 143(3), 314–318 (2019)
66. J. Lopater, P. Colin, F. Beuvon, M. Sibony, E. Dalimier, F. Cornud, and N. B. Delongchamps, "Real-time cancer diagnosis during prostate biopsy: ex vivo evaluation of full-field optical coherence tomography (FFOCT) imaging on biopsy cores," World Journal of Urology 34(2), 237–243 (2016).

67. B. G. Muller, A. Swaan, D. M. de Bruin, W. van den Bos, A. W. Schreurs, D. J. Faber, E. C. Zwartkruis, L. Rozendaal, A. N. Vis, J. A. Nieuwenhuijzen, and R. J. van Moorselaar, "Customized tool for the validation of optical coherence tomography in differentiation of prostate cancer," Technology in Cancer Research & Treatment 16(1), 57–65 (2017).
68. A. Goorsenberg, K. A. Kalverda, J. Annema, and P. Bonta, "Advances in optical coherence tomography and confocal laser endomicroscopy in pulmonary diseases," Respiration 99(3), 190–205 (2020).
69. A. M. Sergeev, V. M. Gelikonov, G. V. Gelikonov, F. I. Feldchtein, R. V. Kuranov, N. D. Gladkova, N. M. Shakhova, L. B. Snopova, A. V. Shakhov, I. A. Kuznetzova, A. N. Denisenko, V. V. Pochinko, Yu. P. Chumakov, and O. S. Streltzova, "In vivo endoscopic OCT imaging of precancer and cancer states of human mucosa," Optics Express 1(13), 432–440 (1997).
70. R. G. Michel, G. T. Kinasewitz, K. M. Fung, and J. I. Keddissi, "Optical coherence tomography as an adjunct to flexible bronchoscopy in the diagnosis of lung cancer: a pilot study," Chest 138(4), 984–988 (2010).
71. R. Wessels, M. van Beurden, D. M. de Bruin, D. J. Faber, A. D. Vincent, J. Sanders, T. G. Van Leeuwen, and T. J. Ruers, "The value of optical coherence tomography in determining surgical margins in squamous cell carcinoma of the vulva: a single-center prospective study," International Journal of Gynecologic Cancer 25(1), 112–118 (2015).
72. H. Wei, G. Wu, Z. Guo, H. Yang, Y. He, S. Xie, and X. Guo, "Assessment of the effects of ultrasound-mediated glucose on permeability of normal, benign, and cancerous human lung tissues with the Fourier-domain optical coherence tomography," Journal of Biomedical Optics 17(11), 116006 (2012).
73. L. P. Hariri, M. Mino-Kenudson, M. Lanuti, A. J. Miller, E. J. Mark, and M. J. Suter, "Diagnosing lung carcinomas with optical coherence tomography," Annals of the American Thoracic Society 12(2), 193–201 (2015).
74. L. P. Hariri, D. C. Adams, M. B. Applegate, A. J. Miller, B. W. Roop, M. Villiger, B. E. Bouma, and M. J. Suter, "Distinguishing tumor from associated fibrosis to increase diagnostic biopsy yield with polarization-sensitive optical coherence tomography," Clinical Cancer Research 25(17), 5242–5249 (2019).
75. M. Jain, N. Narula, B. Salamoon, M. M. Shevchuk, A. Aggarwal, N. Altorki, B. Stiles, C. Boccara, and S. Mukherjee, "Full-field optical coherence tomography for the analysis of fresh unstained human lobectomy specimens," Journal of Pathology Informatics 4 (2013).
76. J. N. d'Hooghe, A. W. Goorsenberg, D. M. de Bruin, J. Roelofs, J. T. Annema, and P. I. Bonta, "Optical coherence tomography for identification and quantification of human airway wall layers," PloS ONE 12(10) e0184145 (2017).

Silver Nanoparticles-Based Substrate for Blood Serum Analysis under 785 nm Laser Excitation

Sahar Z. Al-Sammarraie[1*], Lyudmila A. Bratchenko[1], Elena N. Typikova[1], Peter A. Lebedev[2], Valery P. Zakharov[1], and Ivan A. Bratchenko[1]

[1] Samara University, 34 Moskovskoe shosse, Samara 443066, Russian Federation

[2] Samara State Medical University, 39 Chapaevskaya str., Samara 443099, Russian Federation

*** e-mail:** saharzead@rocketmail.com

Abstract. Individuals who have different diseases need a routine assessment of their body metabolism, and the methods that used are practically difficult, inconvenient or expensive. The objective of this study was to develop a technique of human blood serum analysis that is simple, reliable and fast, and based on a surface-enhanced Raman spectroscopy (SERS). In this study, serum samples were examined using conventional Raman (CR) and SERS. The observed CR and SERS bands were analyzed. Several of these bands (724, 813, 890, 961, and 1132 cm^{-1}) clearly stand out by the impact of the SERS technique, as the intensities of these bands in CR measurements are weaker than the intensity of the autofluorescence and noise. The Enhancement Factor (EF) was up to 4×10^5. Stability of the proposed SERS technique was confirmed by the measurements of signal standard deviation. The observed standard deviation does not exceed 19% for different SERS substrates and does not exceed 8% in case of a single SERS substrate measurements. The obtained results demonstrate that the proposed SERS technique is stable and has significant potential in clinical diagnosis applications.
© 2022 Journal of Biomedical Photonics & Engineering.

Keywords: surface-enhanced Raman spectroscopy; Enhancement Factor; blood serum; silver nanoparticles; Raman band shift.

Paper #3461 received 1 Nov 2021; revised manuscript received 24 Jan 2022; accepted for publication 24 Jan 2022; published online 3 Feb 2022. doi: 10.18287/JBPE22.08.010301.

1 Introduction

The biggest threat to human life and health is a disease, according to death causes statistics provided by the World Health Organization [1]. Numerous diseases are caused by lifestyle behaviors, environmental pollution, occupational hazards, biological and natural factors, chronic intoxication and trauma, iatrogenic factors, and other external factors; and certain diseases are fatal [2, 3]. As a result, the most effective strategies to increase patient survival are early diagnosis and therapy [4]. That is why it is important for individuals who have different diseases to perform a routine assessment of their body functions. Health screening programs are central to the public health system. In order to analyze the functional and pathological processes of the human body, laboratory analyzes of body biofluids are widely used. Many studies on the human body and the investigation of disease processes are done at the level of single cells, proteins, and genes [5–7]. As a result, there is a growing demand for disease diagnostic and analysis technologies. It is necessary to establish a variety of measuring methods and standards for the early detection of various illnesses. Recently, biomarkers have been increasingly utilized in illness diagnosis to signal definite or possible changes in the structure or function of systems, organs, tissues, and cells. It should be noted that laboratory methods used today in clinical practice have a number of limitations.

Recently, Raman spectroscopy has been used to detect viruses, identify bacteria, analyze cells, and make clinical diagnoses [8–14]. Because of its multiple detection capabilities, single-molecule level sensitivity, and quantitative ability, Raman spectroscopy's unique spectral feature makes it an excellent label-free, reliable, and fast diagnostic tool since it can analyze chemical components such as proteins, nucleic acids [6–10], and carbohydrates in biological materials. Surface-enhanced Raman spectroscopy (SERS) has been extensively investigated for biological applications [2–5]. SERS is

recognized as an ultrasensitive optical detection technique with wide application potential in a variety of fields due to its great sensitivity at the single-molecule level.

However, the limitations of the SERS technique are (1) the method requires intimate contact between the enhancing surface and the analyte; (2) the substrates degrade with time resulting in a decrease in the signal; (3) limited selectivity of the substrates for a given analyte; (4) limited re-usability of the substrates; and (5) problems with homogeneity and reproducibility of the SERS signal within a substrate [15]. In this regard, novel approaches of SERS signal registration from the biological fluids are in a high demand. Optimization of methodology of SERS substrates preparation and SERS spectra acquisition requires new approaches to create fast, low-cost and reliable techniques of biofluids chemical sensing.

Thus, in the current study, a simple approach of SERS substrate implementation for blood serum analysis is considered. Blood serum or blood components is a biofluid that is widely used as a diagnostic sample since it is rich in biochemical and biological information, is easily accessible, and can be obtained noninvasively. For the same reasons, it is often saved in biobanks for research purposes. In general, it is a metabolite pool generated from almost all of the human body's organs and tissues. As a result, Raman spectroscopy of human blood samples can be used to monitor metabolic changes caused by illnesses [16–20]. Serum has regularly been investigated using the SERS approach. For instance, Bonifacio et al. [21] employed aqueous Au and Ag colloids in combination with three lasers ranging from visible to near-infrared to perform a systematic study of SERS spectra of blood serum and plasma. However, the SERS spectra analysis indicated that strong and reproducible spectra can be generated rapidly only if proteins are eliminated from samples and a near-infrared excitation is employed in combination with Ag colloids. While Cao et al. [22] investigated the spectral properties of human blood for the purpose of detecting lung adenocarcinoma, lung squamous carcinoma, and large cell lung cancer using SERS spectroscopy on a highly branched gold nanoparticle substrate. They showed that SERS spectroscopy was a sensitive analytical tool for cancer classification and discriminating. Scientific group of Pérez et al. [23] was the first to employ SERS spectroscopy to identify Chagas disease in blood serum using concentrated silver nanoparticles and chemometric techniques. They achieved great accuracy when classifying samples into three categories (healthy patients and asymptomatic patients). However, even when the appropriate experimental parameters are established, significant care must be given while planning research for the development of diagnostic tests. Blood serum, like other biological objects, contains a number of fluorophores and is characterized by the presence of fluorescence [24, 25]. It should be noted that fluorescence is background and noise for the Raman signal. In order to reduce the contribution of fluorescence to the signal in the study of biological objects, the excitation of spectra in the near infrared range is widely used. Therefore, excitation of the spectral characteristics is realized at a wavelength of 785 nm. It is advisable to use particles of silver, copper or gold to achieve surface enhancement of the Raman signal in the near infrared region [26–28]. Colloidal silver solution is characterized by simplicity of preparation.

In the current work to implement a simple analysis of human serum using SERS, a silver SERS substrate was prepared. The goal of this work was to develop a SERS technique based on sliver nanoparticles (Ag NPs) application for simple, reliable and rapid analysis of human serum. To assess the prospects of the proposed SERS technique, the stability of SERS substrates and a comparative analysis of the conventional Raman (CR) spectra and SERS characteristics of serum samples with the calculation of the enhancement factor (EF) were carried out.

2 Materials and methods

2.1 Colloidal silver nanoparticles solution

Silver nitrate and trisodium citrate were used as starting materials for the preparation of (AgNPs). The silver colloid was prepared by using chemical reduction method. All solutions of reacting materials were prepared in distilled water. In typical experiment 20 ml of distilled water heated to boil. To this solution 3 ml of 1.8% $AgNO_3$ of and 6 ml of 1% trisodium citrate ($Na_3C_6H_5O_7$) were added. The resulting solution was heated at 95 °C for 20 min until a yellow-green solution is formed. Then the solution was removed from the heating device and stirred until cooled to room temperature. The UV-Vis spectrum of the AgNPs solution was obtained by utilizing the Spectrophotometer (UNICO 1201, United Products & Instruments, USA). The obtained absorption spectrum of AgNPs solution is shown in Fig. 1 and demonstrates an absorption maximum at 410 nm with a full width at half-maximum of 40 nm, which corresponds to spherical nanoparticles with 20 nm in diameter.

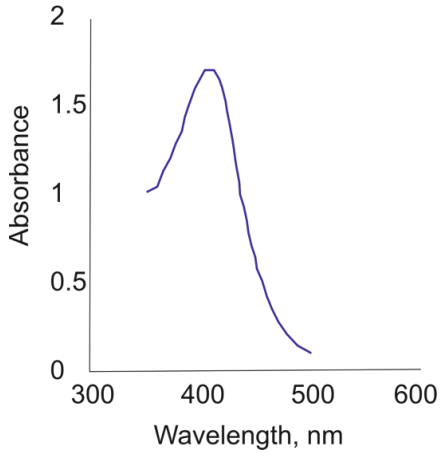
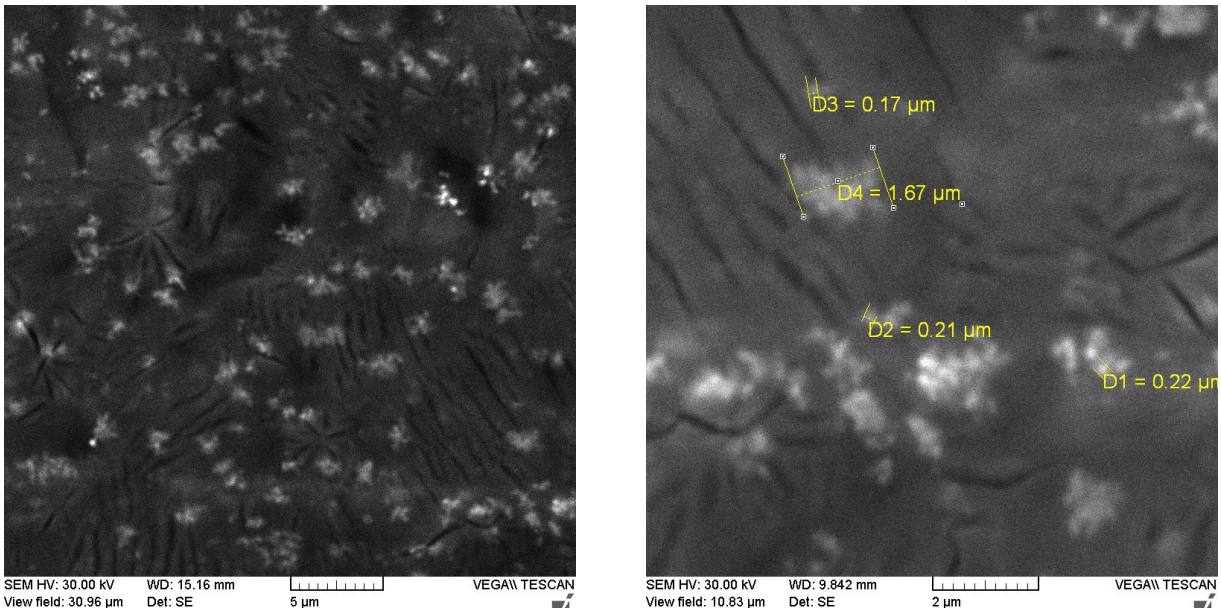


Fig. 1 UV-Vis absorbance spectrum of the colloidal AgNPs.



(a) (b)

Fig. 2 The electron-microscopic images of the substrate with silver particles at magnification factors of 7 000× and 20 000×.

The resulting colloidal solution with a volume of 20 ml was poured onto an aluminum foil with an area of 75 mm × 25 mm and dried at room temperature until completely dry. Fig. 2 presents the electron-microscopic images of the prepared substrate after drying. The electron-microscopic images of the substrate with silver structures were obtained on a Vega SB scanning electron microscope (Tescan, Czech Republic) with an INCA X-act energy dispersive X-ray analyzer (Oxford Instruments, the United Kingdom) at an accelerating voltage of 30 kV. The images contained agglomerates of spherical particles about 200 nm in size.

2.2 Serum samples preparation

A standardized sampling was carried out from patients of the Samara Regional Clinical Hospital named after V. D. Seredavin. The study included patients with stages 1–3a of chronic kidney disease. The study protocols were approved by the ethical committee of Samara State Medical University. All the subjects who participated in this study gave their written informed consent at the beginning of the study. The blood serum samples were collected from patients in fasting condition and placed in sealed containers, followed by freezing at a temperature of –16 °C. Immediately before the start of the analysis, the blood serum samples were defrosted at room temperature.

Each blood serum samples were dropped in a volume of 1.5 µl and dried for 30 min:

- on aluminum foil for CR analysis;
- on aluminum foil with the layer of dried silver colloid for SERS analysis.

2.3 Experimental setup and spectra collection

The experimental setup for Raman analysis of human serum includes a spectrometric system (EnSpectr R785, Spektr-M, Chernogolovka, Moscow Region, Russia) and a microscope (ADF U300, ADF, China). Focusing the exciting radiation and collecting the scattered radiation were implemented using 50× Objective LMPlan. The stimulation of collected spectra was performed by the laser module with central wavelength 785 nm. The diameter of the laser spot at the focus on the sample surface was 5 µm. The laser power was 10 mW for the SERS technique and 60 mW for the CR technique. Exposure time was 4 s for SERS and 20 s for CR. The resulting raw spectrum for each sample is an automatic sequential recording of four spectra with subsequent averaging. Thus, the recording time of the CR raw spectrum is 80 s, and 16 s for SERS.

The analyzed serum sample was examined 15 times in the same position and condition and then examined for 5 different SERS substrates at 5 different spots to indicate the accuracy and stability of the proposed SERS substrates in comparison to CR.

2.4 Spectra processing and calculation of enhancement factor (EF)

The analysis of the stability of the SERS substrate and the reproducibility of the result was carried out on raw spectra without preprocessing. The raw spectral data were subjected to calculating the mean spectrum and standard deviation. Calculation of standard deviation was performed in a standard manner [15]. The mean CR spectra and SERS spectra and shift peaks were assigned to the molecular structures and biochemical components based on the analysis of available studies.

The estimation of the EF is realized in a comparative analysis of the preprocessed CR and SERS spectra. Raw spectra were processed by carrying baseline correction and smoothing to remove noise and fluorescence background. Prior to analysis, the raw spectral data were smoothed by the Savitzky-Golay filter. Savitzky-Golay

filter was applied with filter window width of 15, 1 order of polynomial used for smoothing and 0 order of derivative to take (no derivative). Smoothing aims to remove noise and outliers from a given set of experimental data. Proper smoothing will act to increase the signal-to-noise ratio and enhance the primary features embedded in a given data-set. Numerical means whereby Raman spectral data may be smoothed have been widely employed in the field for many years [18, 29]. Baseline correction is based on polynomial approximation method (tenth-order polynomial function) to separate the autofluorescence and the Raman signal [28]. After spectral processing EF is estimated by the following equation:

$$EF = \frac{I_{SERS} \times EV_{Raman} \times C_{Raman} \times P_{Raman}}{I_{Raman} \times EV_{SERS} \times C_{SERS} \times P_{SERS}}, \quad (1)$$

where I_{SERS} and I_{Raman} are the intensities of the same band for the SERS and CR spectra, respectively; EV_{SERS} and EV_{Raman} are the exposure times for the SERS and CR spectra, respectively; C_{SERS} *and* C_{Raman} are the sample concentration for the SERS and CR spectra, respectively; P_{SERS} and P_{Raman} are the exciting laser power for the SERS and CR spectra, respectively. Since the CR and SERS spectra of the same sample were recorded to calculate the EF, the concentration ratio C_{Raman} / C_{SERS} is equal to 1 ($C_{Raman} = C_{SERS}$).

3 Results and discussion

At the first stage, the characteristic spectral features of a human serum sample using the SERS technology, using the CR technology, and the spectral characteristics of the prepared silver SERS substrate were considered. Fig. 3 shows the recorded raw SERS and CR spectra of serum. Fig. 4 demonstrates the preprocessed SERS and CR spectra of human serum corresponding to the Raman contribution. As can be seen from Fig. 3, the spectral contribution of the silver substrate to the SERS spectrum of the serum sample is insignificant. Consequently, when analyzing the SERS spectrum of serum obtained using the proposed approach, the spectral features characterize the tested serum sample and there is no need to take into account in the analysis the foreign contribution of the substrate. Only a few Raman peaks could be observed in the regular Raman spectra of the serum sample. The SERS spectra of the serum sample, obtained with the proposed technique with AgNPs shows multiple distinctive peaks, and the intensity of these peaks is enhanced compared with that of CR spectra.

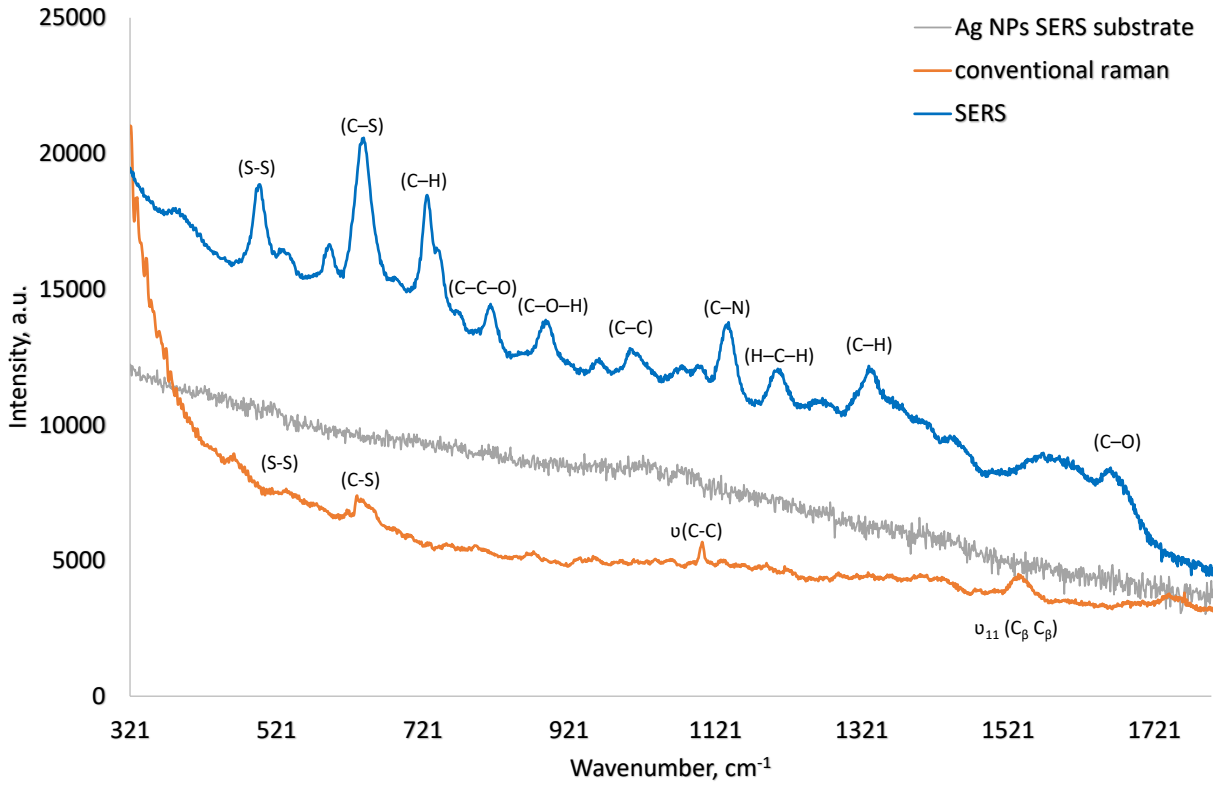


Fig. 3 Comparison of the raw spectrum of a blood serum sample for CR, SERS, and the spectral characteristics of the silver substrate.

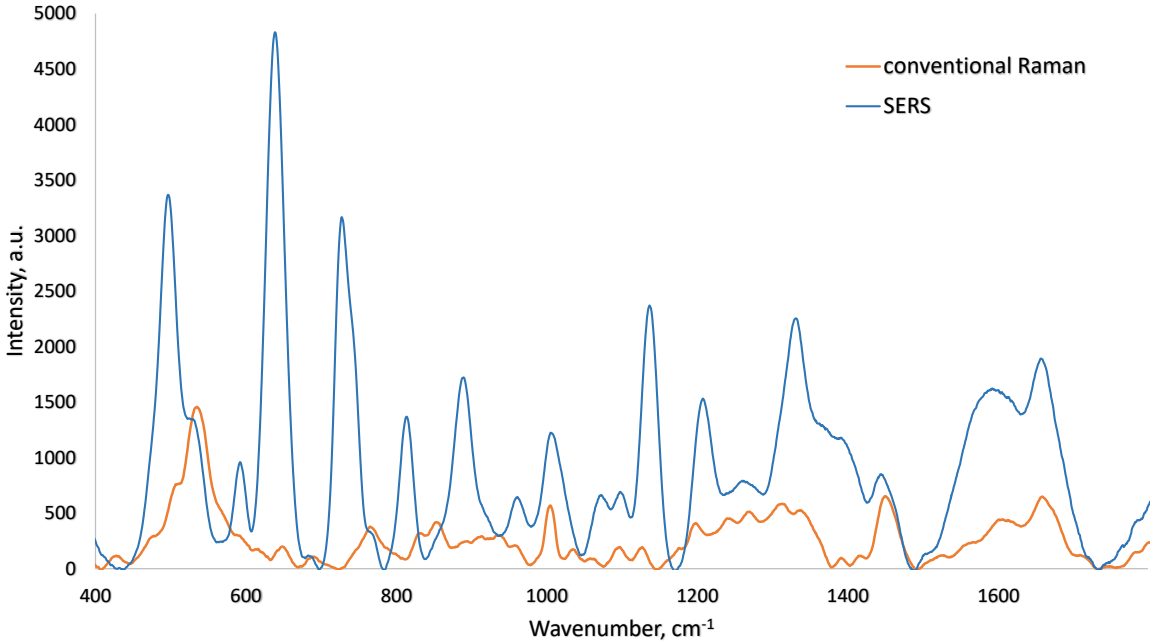


Fig. 4 Comparison of the preprocessed CR and SERS spectra of the same blood serum sample.

Table 1 Peak positions and their characteristic assignments.

Raman shift (cm^{-1})	**Peak assignment**	**Ref.**
Conventional Raman		
525	(S-S) disulfide stretching in proteins Phosphatidylserine	[37, 38]
641	(C–S) L-tyrosine, lactose	[39]
770	(C–H) Hypoxanthine, Phosphatidylserine	[40–43]
1100	υ(C-C)-lipids, fatty acids	[44]
1543	$\upsilon_{11}(C_\beta\ C_\beta)$, tryptophan	[45–46]
1661	(C–O) Amide I, α-helix	[40–43]
SERS		
498	(S-S) disulfide stretching in proteins Phosphatidylserine	[37, 38]
641	(C–S) L- tyrosine, lactose	[39]
728	(C–H) Hypoxanthine, Phosphatidylserine	[37, 38]
813	(C–C–O) L-Serine, glutathione	[37, 38]
890	(C–O–H) Glutathione, D-(C)-galactosamine	[37, 38]
961	υ (C-C), Cholesterol	[37, 38]
1003	(C–C) Phenylalanine	[39]
1086	(C-N) Stretching, Phosphodiester groups in nucleic acids	[37, 38]
1094	(C–N) Stretching mode in D-mannose	[47]
1132	(C-N) Ascorbic acid, L-serine	[37, 38]
1210	$C\text{-}C_6H_5$ stretching, L-tryptophan, phenylalanine	[48]
1291	CH_2 twisting in phospholipids	[37, 38]
1326–1329	CH vibration in DNA/RNA, CH_2 twisting in lipids	[41]
1331	(C–H) Nucleic acid base	[40]
1400	(C–H), Collagen, phospholipids	[41]
1450	$(C\text{-}H_2)$ deformation, Acetoacetate, tryptophan	[37, 38]
1584	(C–C) bending mode of phenylalanine	[40]
1655	(C–O) Amide I, α-helix	[37, 38]

Laser-induced fluorescence is the most common source of interfering baseline signal encountered in Raman measurements. The fluorescence interference in Raman spectroscopy may result from the compound analyzed or from fluorescent impurities in the sample. Autofluorescence background can be produced by tryptophan and tyrosine side chains in folded proteins, by carotenoids and photosynthetic pigments or other chromophores within microbial, animal and plant cells. In addition, it may due to manufacturing additives.

The observed CR and SERS bands are described in Table 1. The major CR peaks are observed at 525, 641, 770, 1100, 1543, 1661 and 1849 cm^{-1} and may be attributed to biochemical components of nucleic acids, fatty acids and Amide I group. For SERS measurements we observe strongly enhanced bands which may be attributed to such biochemical components as nucleic acids (641, 724, 813, 1003, 1210, 1132 and 1450 cm^{-1}), carbohydrates (641, 890, and 1094 cm^{-1}), lipids (1278 and 1327 cm^{-1}), etc. The observed SERS peaks are indicators of the corresponding serum components [29–32].

Several of the observed bands clearly stand out by the impact of SERS technique at 724, 813, 890, 961, and 1132 cm^{-1}. These bands were undetectable by CR spectroscopy, as the intensities of these bands are weaker than the intensity of the autofluorescence and noise signals. The SERS spectrum of serum with AgNPs showed many dominant vibration bands, indicating a strong interaction between the silver colloids and the serum substances. This interaction also indicated that biochemical ingredients in the serum were closely adsorbed onto the surfaces of the AgNPs, and Raman scattering took place in the highly localized optical fields of these structures, which resulted in a strong enhancement in the intensity [29–32].

In SERS spectrum, bands of several molecules could be shifted compared with the bands of these molecules in the CR spectrum. Such shift may be observed from 525, 770, and 1100 cm^{-1} bands to 498, 728, and 1003 cm^{-1} bands respectively. This might be due to the strong interaction between prepared substrate and analyte [33]. It is also found in Fig. 4, which demonstrates the redshift of the SERS spectrum relative to the CR spectrum that observed shift is related to the change of the chemical bond's energy. Some studies have also found the influence of atomic species on the Raman activities. The redshift in SERS is mainly due to the change of the localized plasmons depending on the dielectric functions of metallic nanostructures that, in turn, depend on different parameters, such as the medium, size of NPs, and intrinsic damping of metal, which are known to display this interesting common phenomenon [31]. Moreover, the reason for the blueshift or the redshift of the Raman peak is the change of the corresponding chemical bonds, leading to the migration of electron clouds. Specifically, the change involves the transformation of interatomic bond force and distance [34].

Thus, the spectral bands and SERS characteristics of the serum obtained in the current study are similar to those reported in the studies of other authors. However, Huang et al. and Feng et al. [35, 36] reported SERS bands at 702 cm^{-1} and 1383 cm^{-1} which were not observed in our study; these bands were assigned to the cytosine and CH_3 domains respectively.

The next stage of our research was the analysis of the results repeatability and the stability of the proposed silver substrates. To clarify the central location of the spectral data distribution, a calculation of a mean spectrum was carried out, and the standard deviation of the collected raw spectra was also performed to assess the spread of the values above and below the mean. Such data is presented in Fig. 5 and Fig. 6.

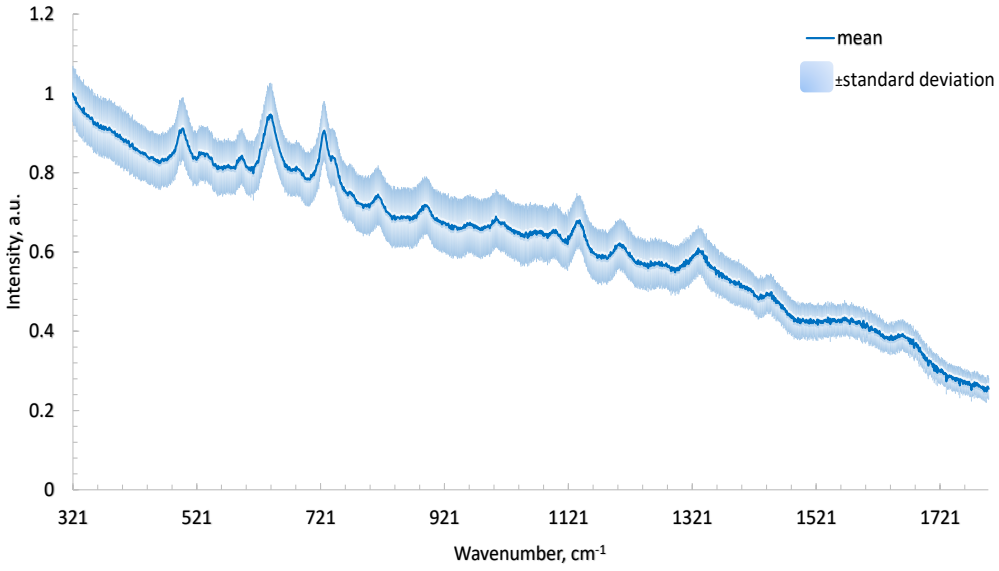


Fig. 5 Mean and standard deviation for human serum sample examined 15 times in the same conditions using single SERS substrate.

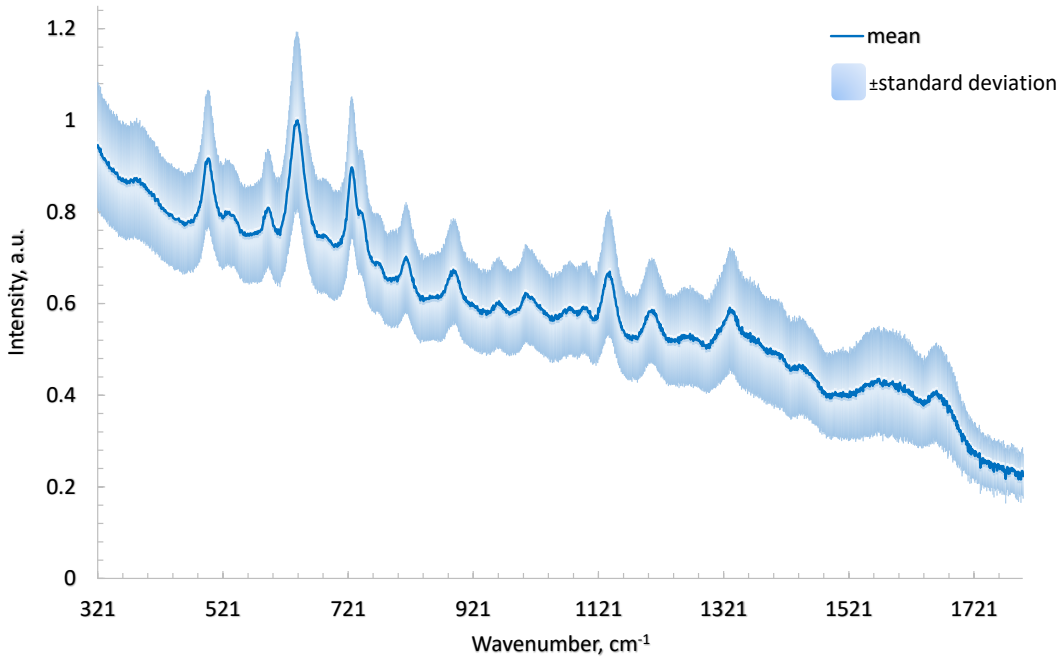


Fig. 6 Mean and standard deviation for serum sample examined for 5 different SERS substrates at 5 different spots.

Table 2 EF values for different spectral bands.

Raman shift (cm^{-1})	I_{Raman}	I_{SERS}	EF
727	0.240	313×10	3.91×10^5
641	131	479×10	1.10×10^3
815	13.4	136×10	3.04×10^3
1132	10.5	231×10	6.60×10^3

The low values of standard deviation show that the data are clustered closely around the mean, thus, the proposed SERS technique is reliable and may be applied in quantitative measurements. In case of a single SERS substrate application maximum standard deviation was up to 8%. In case of different SERS substrates utilization, the standard deviation was up to 19%.

The value of EF depends on the morphology of the NPs. However, the physic-chemical properties of the interfaces, such as the pH, the presence of impurity species, and the available surface on the metal, are also important and may affect the EF value. The interfacial properties of metal surfaces should be considered to understand why certain molecules do not work well in SERS, or why the spectral profile changes from preparation to preparation. The prepared AgNPs were effective and stable, as they are attached to a substrate standing at an appropriate interparticle distance to have a giant electromagnetic enhancement with the formation of hot spots [49]. Lin et al. [50] reported an EF of (5.6×10^9) using gold "pearl necklace" nanomaterials substrate. While Wang et al. [51] found that highly-branched gold nanoparticles provided an EF of (3.6×10^5). However, H. Wang et al. [52] reported an EF of (10^5) for the Ag metalized substrates. The highest EFs observed in the study are collected in Table 2. We found that the largest EF that was calculated from Eq. (1) is detected at 727 cm^{-1} peak and was 3.91×10^5. Note here, that in order to get a higher EFs, it is possible to consider CR bands (I_{Raman}) close to 0, and if newly appeared SERS bands are detected, than the calculated EF value may be extremely high.

The storage stability of the substrates was tested during 1-month period. In this period, we estimated standard deviation of the SERS signal and tracked EF changes. During the tracked period the standard deviation was not higher than the standard deviation observed for single substrate measurements presented above (up to 19%), and EF did not decrease by less than 8%. However, for future possible clinical applications the stability of the substrate should be estimated for a longer period. Important to note, that no blinking phenomenon [53] of SERS spectra from Ag nanoparticles was detected. The term "blinking" is used to describe temporal fluctuations in the Raman spectral signal. It is typically accepted that the observation of blinking behavior in the SERS spectrum is indicative of a single molecule undergoing adsorption/desorption cycles at a SERS "active" site. Blinking in SERS may be attributed to thermal diffusion of a single molecule in and out of hot spots, where

alterations in position of a few nanometers can create a significant change in SERS signal intensity [54, 55]. The intensity of SERS spectra for 5 different SERS substrates at 5 different points and for 15 times in the same condition for one SERS substrate did not change significantly and is within the standard deviation of 19%.

In addition, we showed non-invasiveness of the proposed approach as we examined the serum sample multiple times at the same spot and observed no changes in the intensity for each performed test. It is worth mentioning that the proposed method is quite promising since, unlike previous studies, we employed a non-cooling camera for spectra collection. For instance, Zhou et al. [55] studied SERS effect collecting spectra using a cooling system camera set to –70 °C.

SERS is recognized as an ultrasensitive optical detection technique with wide application potential in a variety of fields due to its great sensitivity at the single molecule level. However, the complex manufacturing and expensive price of SERS substrate remain a barrier to its wide application in industry [56]. Aside from the advantages and limitations of SERS technology in comparison to other diagnostic methods, it is also important to notice that SERS-active substrates are most often fabricated with transition metals (Rh, Pd, Pt, Fe, Co, etc.) and plasmonic metals such as Au and Ag, which have the ability to induce localized surface plasmon resonance, which is a result of the coupling of resonant oscillations of electrons and electromagnetic fields near the nanostructures. However, transition metals have also explored found to impart weaker SERS effects compared to plasmonic metals [57]. In the material selection process, it is also important to consider the suitability of the substrate material in terms of its stability in an environment or condition where it is to be applied. Each plasmonic metal exhibit their own characteristic properties that are not found in other metals; for example, gold is a biocompatible material but provides a lower signal enhancement than silver, which on the other hand is less stable due to it being prone to oxidation [58]. Studies have thus explored the use of both of these metals to take advantage of combining these properties, giving synergistic effects.

Homogeneity is another key point in the evaluation of the SERS substrate, especially when it is used for quantitative detection and imaging. The detection result is reliable only when the results from the substrate are reproducible because SERS is a localized phenomenon and it is highly sensitive to the local structure of the substrate and the surrounding environment. For the NP substrates, the homogeneity in size, shape, and aggregation state will increase the reproducibility. Besides the higher enhancement or better homogeneity, the cost of substrate fabrication should also be considered in SERS applications.

Our proposed approach was found to be considerably easier, faster and more convenient than the methods stated in earlier studies. The colloidal substrates are prepared by either the chemical reduction process or by laser ablation procedures. For instance, Chu et al. [59] proposed a laser ablation-assisted method to fabricate the SERS substrate on the teflon. For the reduction method, Chi et al. [60] created a Silver NP colloidal solution by reducing silver nitrite with sodium citrate in the presence of ultraviolet (UV) light by dropping sodium citrate solution to silver nitrite solution and placing the mixture in a UV chamber. Silicon substrates were immersed in an Ag NP colloidal solution to allow Ag NPs to adhere to the surface. Huang et al. and Zong et al. [35, 61] prepared colloids by adding NaOH solution to hydroxylamine hydrochloride solution and mixing the solution with $AgNO_3$ aqueous solution at room temperature, until the formation of a milky-grey color. The Ag colloids were pelleted by centrifugation. The pelleted Ag NP was then mixed with urine or serum samples at a 1:1 ratio in a rectangle aluminum plate. In another work, Jing et al. [62] used a seed growth technique with AuNPs as seeds to create spherical AgNPs by adding $HAuCl_4$ to deionized water, the solution was heated to boiling. Then, trisodium citrate was immediately added. Serum samples were mixed with the prepared AgNPs solution after cooling. The mixture was transferred to a silicon wafer for SERS analysis.

In comparison to the observed techniques, we have successfully developed a new simple and low-cost AgNPs SERS substrate with excellent sensitivity and promising stability. We obtained excellent SERS spectra using a digital camera without cooling (working at ambient temperature). The proposed technique of blood serum analysis has great potential to significantly increase the application of SERS methods, particularly in clinical applications. Nevertheless, further research in a larger group of collected blood specimens is required to confirm the applicability of the proposed techniques in clinical settings.

4 Conclusion

In this study human blood serum samples were examined using CR and newly proposed SERS technique. To demonstrate the applicability of the proposed technique the serum sample was examined 15 times in the same condition for one SERS substrate and then examined for 5 different SERS substrates at 5 different spots, calculated standard deviation for these cases was up to 8% and up to 19% correspondingly. The obtained results indicate accuracy and stability of the proposed SERS substrates. Demonstrated results shows that the obtained SERS effect helps to achieve up to 4×10^5 EF with silver NPs application for 785 nm laser excitation. Moreover, the proposed SERS technique provides a capability to detect Raman bands 724, 813, 890, 961, and 1132 cm^{-1} which may be attributed to such biochemical components as nucleic acids, carbohydrates, lipids, etc. These bands were not presented in the CR spectra of human serum; thus SERS analysis increases the possibility to detect disease biomarkers during blood samples analysis. The obtained results demonstrate that the proposed SERS technique is stable, no-invasiveness with no blinking phenomenon and has significant potential in clinical diagnosis applications.

Disclosures

All authors declare that there is no conflict of interests in this paper.

Acknowledgments

The study was supported by a grant from the Russian Science Foundation No. 21-75-10097 https://rscf.ru/project/21-75-10097/.

References

1. "Mortality Data", World Health Organization, (accessed 02.02.2022) [https://www.who.int/data/mortality].
2. O. J. Wouters, D. J. O'donoghue, J. Ritchie, P. G. Kanavos, and A. S. Narva, "Early chronic kidney disease: diagnosis, management and models of care," Nature Reviews Nephrology 11(8), 491–502 (2015).
3. S. K. Elwia, S. M. Abo El Wafa, and Y. M. Marei, "The Metabolic Mechanism Underlying the Enhancing Effects of Glycine and Tryptophan on Kidney Function: How to Reduce EGFR Inhibitory Effect on AAs," Egyptian Academic Journal of Biological Sciences, F. Toxicology & Pest Control 13(2), 37–48 (2021).
4. S. Luis-Lima, E. Porrini, "An overview of errors and flaws of estimated GFR versus true GFR in patients with diabetes mellitus," Nephron 136, 287–291 (2017).
5. R. Moynihan, R. Glassock, and J. Doust, "Chronic kidney disease controversy: how expanding definitions are unnecessarily labelling many people as diseased," BMJ 347, f4298 (2013).
6. D.-Q. Chen, G. Cao, H. Chen, D. Liu, W. Su, X.-Y. Yu, N. D. Vaziri, X.-H. Liu, X. Bai, L. Zhang, and Y.-Y. Zhao, "Gene and protein expressions and metabolomics exhibit activated redox signaling and wnt/β-catenin pathway are associated with metabolite dysfunction in patients with chronic kidney disease," Redox biology 12, 505–521 (2017).
7. C. H. Johnson, J. Ivanisevic, and G. Siuzdak, "Metabolomics: beyond biomarkers and towards mechanisms," Nature Reviews Molecular Cell Biology 17(7), 451–459 (2016).
8. P. F. Mulders, "From genes to metabolomics in renal cell carcinoma translational research," European Urology, 2(63), 252–253 (2013).
9. S. Kalim, E. P. Rhee, "An overview of renal metabolomics," Kidney International 91(1), 61–69 (2017).
10. Y. Y. Zhao, "Metabolomics in chronic kidney disease," Clinica Chimica Acta 422, 59–69 (2013).
11. R. H. Weiss, K. Kim, "Metabolomics in the study of kidney diseases," Nature Reviews Nephrology 8(1), 22–33 (2012).
12. L. A. Bratchenko, I. A. Bratchenko, A. A. Lykina, M. V. Komarova, D. N. Artemyev, O. O. Myakinin, A. A. Moryatov, I. L. Davydkin, S. V. Kozlov, and V. P. Zakharov, "Comparative study of multivariative analysis methods of blood Raman spectra classification," Journal of Raman Spectroscopy 51(2), 279–292 (2020).
13. L. A. Bratchenko, I. A. Bratchenko, Y. A. Khristoforova, D. N. Artemyev, D. Y. Konovalova, P. A. Lebedev, and V. P. Zakharov, "Raman spectroscopy of human skin for kidney failure detection," Journal of Biophotonics 14(2), e202000360 (2021).
14. I. A. Bratchenko, L. A. Bratchenko, A. A. Moryatov, Y. A. Khristoforova, D. N. Artemyev, O. O. Myakinin, A. E. Orlov, S. V. Kozlov, and V. P. Zakharov, "In vivo diagnosis of skin cancer with a portable Raman spectroscopic device," Experimental Dermatology 30(5), 652–663 (2021).
15. P. A. Mosier-Boss, "Review of SERS substrates for chemical sensing," Nanomaterials 7(6), 142 (2017).
16. E. Critselis, H. L. Heerspink, "Utility of the CKD273 peptide classifier in predicting chronic kidney disease progression," Nephrology Dialysis Transplantation 31(2), 249–254 (2016).
17. C. Pontillo, L. Jacobs, J. A. Staessen, J. P. Schanstra, P. Rossing, H. J. Heerspink, J. Siwy, W. Mullen, A. Vlahou, H. Mischak, and R. Vanholder, "A urinary proteome-based classifier for the early detection of decline in glomerular filtration," Nephrology Dialysis Transplantation 32(9), 1510–1516 (2017).
18. A. C. Webster, E. V. Nagler, R. L. Morton, and P. Masson, "Chronic kidney disease," The Lancet 389(10075), 1238–1252 (2017).
19. P. Ruggenenti, A. Fassi, A. P. Ilieva, S. Bruno, I. P. Iliev, V. Brusegan, N. Rubis, G. Gherardi, F. Arnoldi, M. Ganeva, and B. Ene-Iordache, "Preventing microalbuminuria in type 2 diabetes," New England Journal of Medicine 351(19), 1941–1951 (2004).
20. E. J. Want, I. D. Wilson, H. Gika, G. Theodoridis, R. S. Plumb, J. Shockcor, E. Holmes, and J. K. Nicholson, "Global metabolic profiling procedures for urine using UPLC–MS," Nature Protocols 5(6), 1005–1018 (2010).
21. A. Bonifacio, S. Dalla Marta, R. Spizzo, S. Cervo, A. Steffan, A. Colombatti, and V. Sergo, "Surface-enhanced Raman spectroscopy of blood plasma and serum using Ag and Au nanoparticles: a systematic study," Analytical and Bioanalytical Chemistry 406(9), 2355–2365 (2014).
22. X. Cao, Z. Wang, L. Bi, and J. Zheng, "Label-free detection of human serum using surface-enhanced raman spectroscopy based on highly branched gold nanoparticle substrates for discrimination of non-small cell lung cancer," Journal of Chemistry 2018, 9012645 (2018).

23. A. Pérez, Y. A. Prada, R. Cabanzo, C. I. González, and E. Mejía-Ospino, "Diagnosis of chagas disease from human blood serum using surface-enhanced Raman scattering (SERS) spectroscopy and chemometric methods," Sensing and Bio-Sensing Research 21, 40–45 (2018).
24. S. Madhuri, N. Vengadesan, P. Aruna, D. Koteeswaran, P. Venkatesan, and S. Ganesan, "Native Fluorescence Spectroscopy of Blood Plasma in the Characterization of Oral Malignancy," Photochemistry and Photobiology 78(2), 197–204 (2003).
25. R. Kalaivani, V. Masilamani, K. Sivaji, M. Elangovan, V. Selvaraj, S. G. Balamurugan, and M. S. Al-Salhi, "Fluorescence spectra of blood components for breast cancer diagnosis," Photomedicine and Laser Surgery 26(3), 251–256 (2008).
26. B. Sharma, R. R. Frontiera, A. I. Henry, E. Ringe, and R. P. Van Duyne, "SERS: Materials, applications, and the future," Materials Today 15(1–2), 16–25 (2012).
27. B. Sardari, M. Özcan, "Real-time and tunable substrate for surface enhanced Raman spectroscopy by synthesis of copper oxide nanoparticles via electrolysis," Scientific Reports 7(1), 7730 (2017).
28. G. M. Herrera, A. C. Padilla, and S. P. Hernandez-Rivera, "Surface enhanced Raman scattering (SERS) studies of gold and silver nanoparticles prepared by laser ablation," Nanomaterials 3(1), 158–172 (2013).
29. A. Subaihi, L. Almanqur, H. Muhamadali, N. AlMasoud, D. I. Ellis, D. K. Trivedi, K. A. Hollywood, Y. Xu, and R. Goodacre, "Rapid, accurate, and quantitative detection of propranolol in multiple human biofluids via surface-enhanced Raman scattering," Analytical Chemistry 88(22), 10884–10892 (2016).
30. E. Witkowska, T. Jagielski, A. Kamińska, A. Kowalska, A. Hryncewicz-Gwóźdź, and J. Waluk, "Detection and identification of human fungal pathogens using surface-enhanced Raman spectroscopy and principal component analysis," Analytical Methods 8(48), 8427–8434 (2016).
31. R. Liu, X. Zi, Y. Kang, M. Si, and Y. Wu, "Surface-enhanced Raman scattering study of human serum on PVA–Ag nanofilm prepared by using electrostatic self-assembly," Journal of Raman Spectroscopy 42(2), 137–144 (2011).
32. J. L. Pichardo-Molina, C. Frausto-Reyes, O. Barbosa-García, R. Huerta-Franco, J. L. González-Trujillo, C. A. Ramírez-Alvarado, G. Gutiérrez-Juárez, and C. Medina-Gutiérrez, "Raman spectroscopy and multivariate analysis of serum samples from breast cancer patients," Lasers in Medical Science 22(4), 229–236 (2007).
33. Q. Liao, M. Y. Li, R. Hao, X. C. Ai, J. P. Zhang, and Y. Wang, "Surface-enhanced Raman scattering and DFT computational studies of a cyanuric chloride derivative," Vibrational Spectroscopy 44(2), 351–356 (2007).
34. H. Ma, S. Liu, N. Zheng, Y. Liu, X. X. Han, C. He, H. Lu, and B. Zhao, "Frequency shifts in surface-enhanced Raman spectroscopy-based immunoassays: mechanistic insights and application in protein carbonylation detection," Analytical Chemistry 91(15), 9376–9381 (2019).
35. Z. Huang, S. Feng, Q. Guan, T. Lin, J. Zhao, C. Y. Nguan, H. Zeng, D. Harriman, H. Li, and C. Du, "Correlation of surface-enhanced Raman spectroscopic fingerprints of kidney transplant recipient urine with kidney function parameters," Scientific Reports 11(1), 2463 (2021).
36. S. Feng, L. Zhou, D. Lin, J. Zhao, Q. Guan, B. Zheng, K. Wang, H. Li, R. Chen, H. Zeng, and C. Du, "Assessment of treatment efficacy using surface-enhanced Raman spectroscopy analysis of urine in rats with kidney transplantation or kidney disease," Clinical and Experimental Nephrology 23(7), 880–889 (2019).
37. N. Stone, C. Kendall, J. Smith, P. Crow, and H. Barr, "Raman spectroscopy for identification of epithelial cancers," Faraday Discussions 126, 141–157 (2004).
38. N. Stone, C. Kendall, N. Shepherd, P. Crow, and H. Barr, "Near-infrared Raman spectroscopy for the classification of epithelial pre-cancers and cancers," Journal of Raman spectroscopy 33(7), 564–573 (2002).
39. J. W. Chan, D. S. Taylor, T. Zwerdling, S. M. Lane, K. Ihara, and T. Huser, "Micro-Raman spectroscopy detects individual neoplastic and normal hematopoietic cells," Biophysical Journal 90(2), 648–656 (2006).
40. S. Feng, R. Chen, J. Lin, J. Pan, Y. Wu, Y. Li, J. Chen, and H. Zeng, "Gastric cancer detection based on blood plasma surface-enhanced Raman spectroscopy excited by polarized laser light," Biosensors and Bioelectronics 26(7), 3167–3174 (2011).
41. J. Lin, R. Chen, S. Feng, J. Pan, Y. Li, G. Chen, M. Cheng, Z. Huang, Y. Yu, and H. Zeng, "A novel blood plasma analysis technique combining membrane electrophoresis with silver nanoparticle-based SERS spectroscopy for potential applications in noninvasive cancer detection," Nanomedicine: Nanotechnology, Biology and Medicine 7(5), 655–663 (2011).
42. J. De Gelder, K. De Gussem, P. Vandenabeele, and L. Moens, "Reference database of Raman spectra of biological molecules," Journal of Raman Spectroscopy: An International Journal for Original Work in all Aspects of Raman Spectroscopy, Including Higher Order Processes, and also Brillouin and Rayleigh Scattering 38(9), 1133–1147 (2007).
43. Z. Movasaghi, S. Rehman, and D. I. ur Rehman, "Fourier transform infrared (FTIR) spectroscopy of biological tissues," Applied Spectroscopy Reviews 43(2), 134–179 (2008).
44. G. Shetty, C. Kendall, N. Shepherd, N. Stone, and H. Barr, "Raman spectroscopy: elucidation of biochemical changes in carcinogenesis of oesophagus," British Journal of Cancer 94(10), 1460–1464 (2006).
45. D. Naumann, "Infrared and NIR Raman spectroscopy in medical microbiology," Proceedings of SPIE 3257, 245–257 (1998).

46. R. J. Lakshmi, V. B. Kartha, C. R. Murali Krishna, J. G. Solomon, G. Ullas, and P. Uma Devi, "Tissue Raman spectroscopy for the study of radiation damage: brain irradiation of mice," Radiation Research 157(2), 175–182 (2002).
47. W. T. Cheng, M. T. Liu, H. N. Liu, and S. Y. Lin, "Micro-Raman spectroscopy used to identify and grade human skin pilomatrixoma," Microscopy Research and Technique 68(2), 75–79 (2005).
48. D. P. Lau, Z. Huang, H. Lui, D. W. Anderson, K. Berean, M. D. Morrison, L. Shen, and H. Zeng, "Raman spectroscopy for optical diagnosis in the larynx: preliminary findings," Lasers in Surgery and Medicine 37(3), 192–200 (2005).
49. M. V. Canamares, J. V. Garcia-Ramos, S. Sanchez-Cortes, M. Castillejo, and M. Oujja, "Comparative SERS effectiveness of silver nanoparticles prepared by different methods: A study of the enhancement factor and the interfacial properties," Journal of Colloid and Interface Science 326(1), 103–109.
50. Z. H. Lin, I. C. Chen, and H. T. Chang, "Detection of human serum albumin through surface-enhanced Raman scattering using gold "pearl necklace" nanomaterials as substrates," Chemical Communications 47(25), 7116–7118 (2011).
51. Z. Y. Wang, W. Li, Z. Gong, P. R. Sun, T. Zhou, and X. W. Cao, "Detection of IL-8 in human serum using surface-enhanced Raman scattering coupled with highly-branched gold nanoparticles and gold nanocages," New Journal of Chemistry 43(4), 1733–1742 (2019).
52. H. Wang, N. Malvadkar, S. Koytek, J. Bylander, W. B. Reeves, and M. C. Demirel, "Quantitative analysis of creatinine in urine by metalized nanostructured parylene," Journal of Biomedical Optics 15(2), 027004 (2010).
53. C. Popa, M. Petrus, and A. M. Bratu, "Ammonia and ethylene biomarkers in the respiration of the people with schizophrenia using photoacoustic spectroscopy," Journal of Biomedical Optics 20(5), 057006 (2015).
54. Y. Kitahama, "Observation and analysis of blinking surface-enhanced Raman scattering," Journal of Visualized Experiments 131, e56729 (2018).
55. Y. Zhu, C. S. Choe, S. Ahlberg, M. C. Meinke, A. Ulrike, J. M. Lademann, and M. E. Darvin, "Penetration of silver nanoparticles into porcine skin ex vivo using fluorescence lifetime imaging microscopy, Raman microscopy, and surface-enhanced Raman scattering microscopy," Journal of Biomedical Optics, 20(5), 051006 (2014).
56. Y. S. Huh, A. J. Chung, and D. Erickson, "Surface enhanced Raman spectroscopy and its application to molecular and cellular analysis," Microfluidics and Nanofluidics 6(3), 285–297 (2009).
57. M. Sharifi, S. H. Hosseinali, R. H. Alizadeh, A. Hasan, F. Attar, A. Salihi, M. S. Shekha, K. M. Amen, F. M. Aziz, A. A. Saboury, and K. Akhtari, "Plasmonic and chiroplasmonic nanobiosensors based on gold nanoparticles," Talanta 212, 120782 (2020).
58. Y. L. Liu, J. Zhu, G. J. Weng, J. J. Li, and J. W. Zhao, "Gold nanotubes: synthesis, properties and biomedical applications," Microchimica Acta 187(11), 612 (2020).
59. F. Chu, S. Yan, J. Zheng, L. Zhang, H. Zhang, K. Yu, X. Sun, A. Liu, and Y. Huang, "A simple laser ablation-assisted method for fabrication of superhydrophobic SERS substrate on Teflon film," Nanoscale Research Letters 13(1), 244 (2018).
60. J. Chi, T. Zaw, I. Cardona, M. Hosnain, N. Garg, H. R. Lefkowitz, P. Tolias, and H. Du, "Use of surface-enhanced Raman scattering as a prognostic indicator of acute kidney transplant rejection," Biomedical Optics Express 6(3), 761–769 (2015).
61. M. Zong, L. Zhou, Q. Guan, D. Lin, J. Zhao, H. Qi, D. Harriman, L. Fan, H. Zeng, and C. Du, "Comparison of Surface-Enhanced Raman Scattering Properties of Serum and Urine for the Detection of Chronic Kidney Disease in Patients," Applied Spectroscopy 75(4), 412–421 (2021).
62. J. Guo, Z. Rong, Y. Li, S. Wang, W. Zhang, and R. Xiao, "Diagnosis of chronic kidney diseases based on surface-enhanced Raman spectroscopy and multivariate analysis," Laser Physics 28(7), 075603 (2018).

Mathematical Modelling of the Influence of Different Concentrations of Oxaloacetate to Glycerol-3-Phosphate Dehydrogenase Structure

Nataliya A. Kolotyeva[1*], Frida N. Gilmiyarova[1], Oksana A. Gusyakova[1], Marina V. Komarova[2], Nikita V. Remizov[2], and Elena A. Ryskina[3]

[1] Samara State Medical University, 89 Chapaevskaya str, Samara 443099, Russia
[2] Samara National Research University, 34 Moskovskoe shosse, Samara 443086, Russia
[3] Higher School of Economics, 20 Myasnitskaya str., Moscow 101000, Russia

*** e-mail:** n.a.koloteva@samsmu.ru

Abstract. The study was devoted to the influence of different concentrations of oxaloacetate on the conformational structure of glycerol-3-phosphate dehydrogenase in a temperature gradient, using differential scanning fluorimetry on a Prometheus NT.48 device (NanoTemper Technologies, Germany). We studied the fluorescence ratio (350/330 nm) of glycerol-3-phosphate dehydrogenase in the presence of oxaloacetate at concentrations of 0.5–16 μM in a temperature gradient of 20–95 °C. We built linear regression models for the physiological temperature range and nonlinear models (polynomial of the third degree) for the temperature range corresponding to protein melting. Temperature was the independent variable; fluorescence ratio was the variable. The effect of different oxaloacetate concentrations on glycerol-3-phosphate dehydrogenase thermostability was evaluated by comparing the parameters of obtained regression models. At the physiological temperature range of 20–40 °C, the fluorescence ratios and their growth rates at oxaloacetate concentrations of 0.5-8 μM ($p < 0.001$) were found to be lower than those of controls. Higher average fluorescence ratios and growth rates were detected at oxaloacetate concentrations of 16 μM ($p < 0.001$). When heating over 45 °C, no differences were found in the average denaturation temperature of glycerol-3-phosphate dehydrogenase between the oxaloacetate concentrations studied. The experiment demonstrates the change in the total amplitude of the fluorescence signal in the process of heating the enzyme. The effect of biologically active compounds on fluorescence ratio differs in the area of low concentrations (0.5 and 1 μM) and high concentrations (16 μM). Oxaloacetate at a final concentration of 0.5–1 μM contributes to the thermodynamic stability of glycerol-3-phosphate dehydrogenase, while the concentration of 16 μM causes a decrease in its thermostability. © 2022 Journal of Biomedical Photonics & Engineering.

Keywords: glycerol-3-phosphate dehydrogenase; oxaloacetate; differential scanning fluorimetry; conformation structure; mathematical modelling.

Paper #3462 received 02 Nov 2021; accepted for publication 28 Feb 2022; published online 21 Mar 2022. doi: 10.18287/JBPE22.08.010302.

1 Introduction

In recent years, there has been an increasing interest in small molecules – compounds with a molecular mass between 40 and 1000 Da – that can change the content of metabolites and their fluxes in the pathways of intermediate metabolism, which can regulate specific intermolecular processes. The study of small molecules today seems to be an urgent task because, having a very

small molecular weight, they have multiple effects not only on metabolism in general, but also on intercellular interaction systems [1–4].

Glycerol-3-phosphate dehydrogenase (EC 1.1.1.8, GPDH), is a NAD-dependent dehydrogenase located at the crossroads of the metabolic pathways of carbohydrate and fat metabolism, whose structural and functional potential enables numerous biomolecular processes. Dihydroxyacetone phosphate and the redox partner, glycerol 3-phosphate, are substrates of the reaction. With a lack of energy, the dihydroxyacetone phosphate molecule continues its way in the glycolytic process; if there is enough energy, it can enter the lipid biosynthesis pathway [5, 6]. Numerous metabolic and non-metabolic functions of these switches are provided by gentle regulation by GPDH. Mitochondrial GPDH has been shown to accelerate glucose oxidation by stimulating acetyl coenzyme A production, histone acetylation, and induction of genes encoding inflammatory mediators in macrophages, promoting oncogenesis in glioma cells [7, 8]. The study of GPDH represents a therapeutic target for treatment and mechanisms of cancer regulation [9–11].

Oxaloacetate (OA) is a metabolic intermediate, a valuable and rather rare molecule, its concentration in mitochondria does not exceed 10^{-6} M [12], participates in many metabolic pathways, including gluconeogenesis, the citric acid cycle, the glyoxylate cycle, amino acid synthesis, fatty acid synthesis. Oxaloacetate is a critical component in ATP production and must be continuously regenerated for the citric acid cycle and electron transfer chain to continue. Oxaloacetate is important not only as a molecular switch and mediator in complex biological processes. Due to its central role in energy metabolism, it has been called a bioenergetic drug specifically designed to increase cellular energy levels, has protective, promitochondrial actions, prevents neuroinflammation, neurodegeneration [13–15].

The use of the differential scanning fluorimetry method makes it possible to evaluate protein folding as well as its conformational and colloidal stability under various thermal and chemical conditions. The principle of the method is based on changes in the endogenous fluorescence of tryptophan and tyrosine, which is very sensitive and changes with thermal unfolding. Using a thermal gradient causes denaturation of the tertiary structure, the protein unfolds, which contributes to the escape of hydrophobic sites with tryptophan from the pockets. This leads to a shift in the fluorescence peaks; differential scanning fluorimetry tracks these changes with high temporal resolution and can even detect several unfolding transitions [16].

This study focuses on the effect of different concentrations of oxaloacetate on the conformational structure of glycerol-3-phosphate dehydrogenase in a temperature gradient, followed by the study of fluorescence curves and fitting mathematical model.

2 Materials and Methods

2.1 The Experiment overview

The experiments were performed in the Laboratory of Molecular and Radiation Biophysics at the National Research Center “Kurchatov Institute”.

We used reagents from Sigma-Aldrich, USA: catalytic protein glycerol-3-phosphate dehydrogenase, oxaloacetate, 50 mM Tris-HCl buffer, pH 7.5. The pH value was monitored before and after adding the small molecule solution to the samples using a Mettler Toledo pH-meter (USA). The change in pH of the medium had fluctuations within the range of 0.01–0.02.

The conformational structure of glycerol-3-phosphate dehydrogenase protein molecules under the influence of oxaloacetate was determined using Differential Scanning Fluorimetry (DSF) on a Prometheus NT.48 instrument (NanoTemper Technologies, Germany). The conformational stability of the protein was described by its average denaturation temperature Tm (°C), which is the point where half of the protein unfolds. The principle of differential scanning fluorimetry is based on the change in endogenous fluorescence of tryptophan and tyrosine at 330 and 350 nm, which changes with thermal unfolding [17]. Six dilutions were prepared in which the final concentration of GPDH was constant, 1 μM, and the final concentration of oxaloacetate solution varied: 0.5 μM, 1 μM, 2 μM, 4 μM, 8 μM, and 16 μM. We placed 10 μl of the prepared solution into Prometheus NT.48, nanoDSF grade capillaries (Germany). Scanning fluorimetry was performed at a laser intensity of 30%, heating range from 20 °C to 95 °C, step 1 °C/min.

2.2 Statistical Analyses

Mathematical modeling of fluorescence ratio curves as a function of temperature and oxaloacetate concentration and statistical analysis of obtained parameters of regression equations were performed using SPSS v. 25 (IBM Corporation, Armonk, New York, USA). We used linear models and analysis of covariance (ANCOVA) for the physiological temperature range, approximation by cubic regression to investigate protein melting point. To assess the quality of fitted models, we examined regression residuals, calculated coefficients of determination (R^2) and standard errors of regression (SE regr). A two-tailed p-value < 0.05 was considered statistically significant.

3 Results and Discussion

Preliminary visual analysis of the melting curves of GPDH without ligand and with the oxaloacetate (Fig. 1) makes it possible to distinguish several sites that differ in biochemical nature. In the physiological temperature range (up to 45–50 °C) there is a linear increase in the fluorescence ratio, at a temperature of the order of 50–55°C – melting, and at higher temperatures – a subsequent increase in the fluorescence ratio.

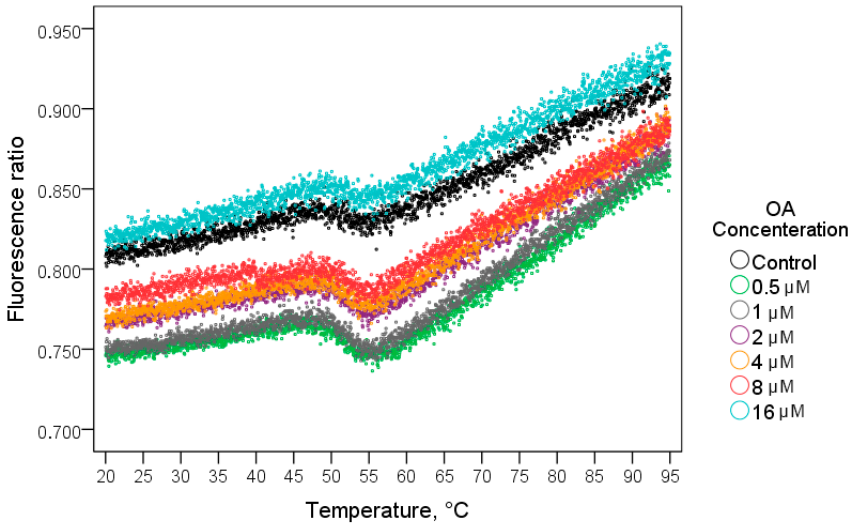


Fig. 1 Ratio of fluorescences at different concentrations of oxaloacetate during GPDH heating in the temperature range 20–95 °C.

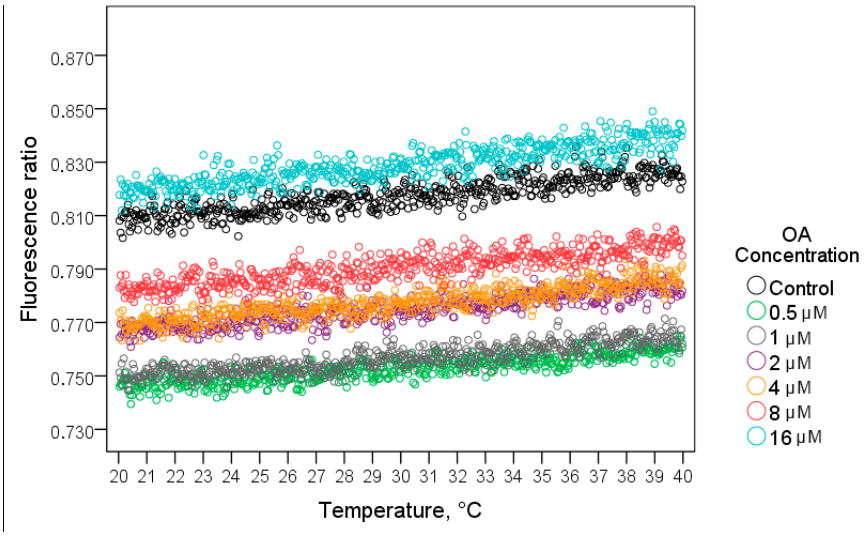


Fig. 2 Ratio of fluorescences at different concentrations of oxaloacetate during GPDH heating in the temperature range 20–40 °C.

Table 1 Summary of linear models of the relationship of GPDH fluorescence to temperature in the range from 20 to 40 °C when oxaloacetate is added at different concentrations.

Concentration of oxaloacetate	**Intercept, × 10^{-3}**		**Slope, × 10^{-3}**		**Model Quality Assessment**	
	b_0	SE b_0	b_1	SE b_1	R^2	SE regr
Control	789.1	0.77	0.95	0.025	0.72	3.43
0.5 µM	731.5	0.58	0.71	0.019	0.70	2.59
1 µM	733.6	0.62	0.77	0.020	0.73	2.77
2 µM	749.8	0.66	0.84	0.022	0.74	2.91
4 µM	751.3	0.68	0.88	0.022	0.77	2.99
8 µM	764.1	0.77	0.88	0.025	0.76	3.42
16 µM	797.5	0.83	1.05	0.027	0.70	3.68

Note: b_0 – constant; SE b_0 – standard errors of constant; b_1 – regression coefficients; SE b_1 – standard errors of regression coefficients; R^2 – coefficient of determination; SE regr – standard errors of regression.

At the first stage, we isolated the temperature range corresponding to the physiological norm from 20 to 40 °C (Fig. 2) and compared the average values of the fluorescence ratio in the presence of different concentrations of oxaloacetate and their growth rate. We used paired linear regression analysis, which determines the inclination angles of the linear growth of the fluorescence ratio, and covariance analysis (ANCOVA), which allows comparing these inclination angles in different ligands and comparing the mean fluorescence ratio values.

A summary of the parameters of the fitted pairwise linear regression equations, coefficients of determination and standard regression errors are shown in Table 1. All fitted models are statistically significant and have good quality: determination coefficients (R^2) are from 0.70 to 0.77. Standard regression errors are from 2.5×10^{-3} to 3.43×10^{-3}.

Fig. 3 shows the slope angles of the regression lines (parameters b_1 of each equation and its 95% confidence interval).

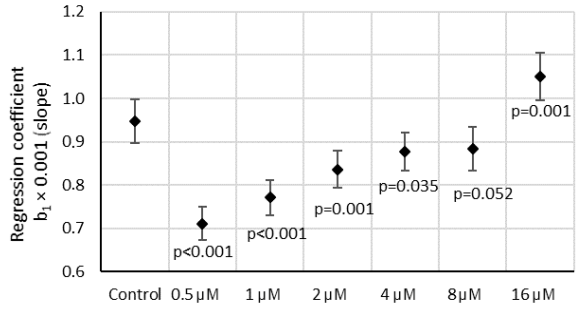


Fig. 3 Angles of regression equations of fluorescence ratio growth when HPA is heated in the temperature range from 20 to 40 °C when oxaloacetate is added at different concentrations: regression coefficients b_1 and their 95% CI

Covariance analysis presents a pooled linear model for controlling and varying ligand concentrations (Table 2).

According to the model, ANCOVA mean values of fluorescence ratio in the middle of the studied temperature range are as follows (95% confidence intervals are given in parentheses):

Control: 0.817 (95% CI: 0.817–0.818),
0.5 µM: 0.753 (95% CI: 0.753–0.753),
1 µM: 0.757 (95% CI: 0.756–0.757),
2 µM: 0.775 (95% CI: 0.775–0.775),
4 µM: 0.778 (95% CI: 0.777–0.778),
8 µM: 0.791 (95% CI: 0.790–0.791),
16 µM: 0.829 (95% CI: 0.829–0.829).

As shown in Figs. 1 and 2, and in Table 2, fluorescence ratios are lower at the probe with oxaloacetate concentration of 0.5–8 µM (all $p < 0.001$), than in the control, the lowest ligand concentration being 0.5 µM. Conversely, higher average fluorescence ratios were detected at a ligand concentration of 16 µM ($p < 0.001$).

As for the comparison of the growth rate of fluorescence ratios when heated to 40 °C, lower values were obtained for a ligand concentration of 0.5–2 µM (all $p < 0.001$) than in the control sample. Close to control but slightly lower for oxaloacetate concentrations 4 and 8 µM ($p = 0.035$ and $p = 0.052$) and higher fluorescence ratio growth rates were noted for a concentration of 16 µM ($p = 0.001$).

In the next step, we studied the effect of oxaloacetate on the conformational stability of GPDH when the enzyme was heated to melting point. To do this, we selected different variants of nonlinear regression models, so that on the one hand there was an acceptable approximation quality, and on the other hand, that regression parameters had a good biochemical interpretation, since the goal of the simulation is to compare the parameters found at different concentrations of small molecules.

We considered a number of possible models: sinusoidal, S-shaped, Hill's equation, cubic parabola. As a result of a detailed analysis of mathematical models, it was decided to use a cubic parabola of the following form:

$$f(t) = d \times (t - b)^3 + c \times t + a, \qquad (1)$$

where $f(t)$ is a dependent variable, fluorescence ratio; t – independent variable, temperature, °C; *a, b, c, d* are parameters of the equation, or regression coefficients.

The choice of this mathematical model for the present study is due to the simplicity and convenient meaningful interpretation of its parameters: b – corresponds to the theoretical inflection point during melting or the average denaturation temperature Tm (°C). Indeed, the second derivative $f(t)$ is as follows:

$$\frac{d^2 f(t)}{dt^2} = 6 \times d \times (t - b). \qquad (2)$$

Equating $6 \times d \times (t - b)$ to zero, we get $t = b$.

Parameter c corresponds to the maximum melting rate. This is proved as follows. The first derivative of the function $f(t)$ is calculated:

$$\frac{df(t)}{dt} = 3 \times d \times (t - b)^2 + c. \qquad (3)$$

At the temperature of the inflection point: $t = b$, the value of the first derivative and, accordingly, the melting rate of the protein is obtained equal to the parameter *c*.

Comparison of different concentrations of oxaloacetate was carried out by the method of confidence intervals: their overlap indicates the statistical indistinguishability of these parameters, and non-overlap indicates the statistical significance of differences in the melting parameter under study.

To build models, a temperature range of 44–56 °C was chosen. The approximation quality for different oxaloacetate concentrations was very different (Table 3, Fig. 4). Thus, for ligand concentrations from 0.5 to 8 mkM, the coefficients of determination were from 0,64 to 0,84, which characterizes the models as fairly accurate.

Table 2 Parameters of the combined ANCOVA model for the dependence of the GPDH fluorescence ratio on the temperature in the range from 20 to 40 °C when oxaloacetate is added at different concentrations.

	b, × 10^{-3}	**SE b, × 10^{-3}**	**p**
Intercept	789.09	0.708	<0.001
temperature	0.95	0.023	<0.001
0.5 µM	–57.58	1.001	<0.001
1 µM	–55.52	1.001	<0.001
2 µM	–39.25	1.001	<0.001
4 µM	–37.82	1.001	<0.001
8 µM	–25.00	1.001	<0.001
16 µM	8.39	1.001	<0.001
Control	reference	–	–
Interaction Effects			
0.5 µM × temperature	–0.24	0.033	<0.001
1 µM × temperature	–0.18	0.033	<0.001
2 µM × temperature	–0.11	0.033	0.001
4 µM × temperature	–0.07	0.033	0.035
8 µM × temperature	–0.06	0.033	0.052
16 µM × temperature	0.10	0.033	0.001
Control × temperature	reference	–	–

Note: b – regression coefficients; SE b – standard errors of regression coefficients; p – significance level.

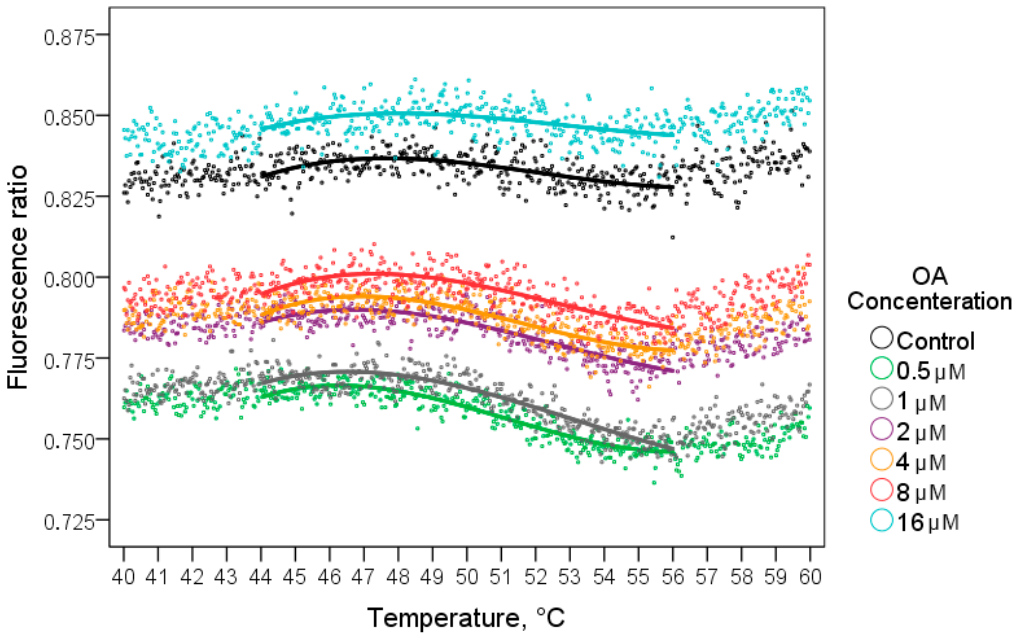


Fig. 4 Ratio of fluorescences during GPDH melting in the temperature range from 44 to 56 °C when oxaloacetate is added at different concentrations: observed values and approximation by cubic parabola.

At the same time, for the reference sample model, the R^2 determination coefficient is 0.33, and for a sample with an oxaloacetate concentration of 16 µM R^2 a total of 0.16. The standard regression errors for all models are in the 0.003–0.005 range.

Table 3 Summary of nonlinear models of dependence of fluorescence ratio at melting of GPDH in temperature range from 44 to 56 °C at addition of oxaloacetate at different concentrations.

	a	b	c, × 10^{-3}	d, × 10^{-6}	R^2	p
Control	0.911±0.007	52.13±0.66	–1.51±0.13	25.15±7.07	0.33	<0.001
0.5 μM	0.917±0.006	51.15±0.19	–3.14±0.11	43.46±5.34	0.84	<0.001
1 μM	0.934±0.007	53.10±0.77	–3.35±0.14	25.76±6.11	0.82	<0.001
2 μM	0.923±0.006	52.59±0.70	–2.72±0.12	26.41±6.71	0.71	<0.001
4 μM	0.923±0.006	51.62±0.30	–2.66±0.12	40.10±6.31	0.70	<0.001
8 μM	0.928±0.007	52.66±0.64	–2.58±0.13	29.95±6.74	0.64	<0.001
16 μM	0.907±0.008	52.83±1.45	–1.13±0.16	16.37±7.95	0.16	<0.001

Note: a –parameter of the equation; b – parameter of the equation, corresponds theoretical inflection point during melting or average denaturation temperature Tm, °C; c – parameter of the equation, corresponds the maximum melting rate of GPDH at inflection point; d – parameter of the equation; R^2 – coefficient of determination; p – significance level.

A graphical representation of the regression parameter b characterizing the temperature of the inflection point at which the melting rate is maximum is shown in Fig. 5. Overlapping confidence intervals of parameter b indicate that inflection points at different intermediate concentrations do not differ.

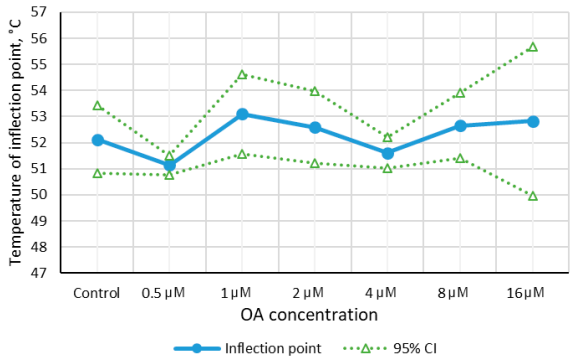


Fig. 5 Inflection points of fluorescence ratios during GPDH melting in the temperature range from 44 to 56 °C with addition of oxaloacetate at different concentrations. The regression coefficients b from the cubic model (solid line) and their 95% CI (dotted lines) are given.

The maximum melting rates according to the fitted mathematical models differ significantly (Fig. 6). Since the fluorescence ratios decrease when the protein melts, the velocities have a negative sign. The fastest melting (the highest absolute value parameters with corresponding to the first derivatives at the inflection point) was noted for GPDH in the presence of oxaloacetate at a concentration of 0.5 μM and 1 μM. A smaller, but also significantly different melting rate is characteristic of ligand concentrations of 2 to 8 μM. Finally, the presence of 16 μM oxaloacetate in the sample did not cause the melting rate to differ from the control sample.

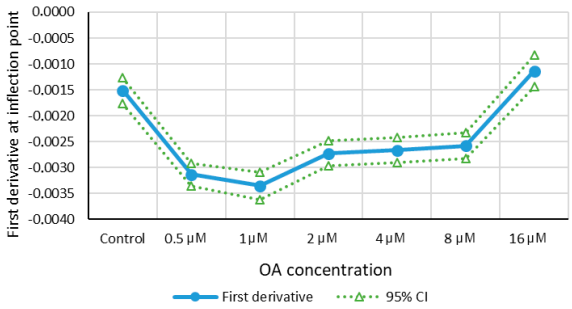


Fig. 6 Maximum melting rates of GPDH in the temperature range from 44 to 56 °C with addition of oxaloacetate at different concentrations. Regression coefficients *c* from cubic model (solid line) and their 95% CI (dotted lines) are given.

4 Conclusions

The experiment demonstrates that the total amplitude of the fluorescence signal in the process of heating the enzyme changed. The effect of biologically active compounds on the fluorescence ratio differs in the area of low concentrations (0.5 and 1 μM) and high concentrations (16 μM). In the physiological temperature range, a linear increase in the fluorescence ratio by an average of $0.95 \pm 0.024 \times 10^{-3}$ for each degree of heating occurs when heated from 20 to 40 °C. Oxaloacetate concentrations of 0.5 μM and 1 μM cause the most significant decreases in fluorescence ratios and its growth rate compared with the control, which mediates the folding of the protein molecule and increases the thermodynamic stability of glycerophosphate dehydrogenase. Oxaloacetate concentrations of 16 μM cause an increase in the fluorescence ratio and an increase in its growth rate, which results in unfolded conformation of the enzyme molecule and a decrease in thermostability.

Documenting and interpreting interactions between metabolites and proteins in a biological context is expected to be important for assessing human health, helping researchers understand the molecular basis of normal and pathological conditions. In particular, regulators of metabolites associated with changes in protein structure may provide new strategies for potential therapeutic interventions.

Disclosures

All authors declare that there is no conflict of interests in this paper.

References

1. E. L. Van Nostrand, S. C. Huelga, and G. W. Yeo, "Experimental and Computational Considerations in the Study of RNA-Binding Protein-RNA Interactions," Advances in Experimental Medicine and Biology 907, 1–28 (2016).
2. E. A. Ryskina, N. A. Kolotyeva, F. N. Gilmiyarova, and N. N. Chernov, "Intermolecular interaction of proteins and small molecules (review)," European Journal of Natural History 3, 8–13 (2016).
3. K. Rooijers, C. M. Markodimitraki, F. J. Rang, S. S. de Vries, A. Chialastri, K. L. de Luca, D. Mooijman, S. S. Dey, and J. Kind, "Simultaneous quantification of protein-DNA contacts and transcriptomes in single cells," Nature Biotechnology 37(7), 766–772 (2019).
4. Q. Xu, R. L. Dunbrack Jr., "ProtCID: a data resource for structural information on protein interactions," Nature Communications 11(1), 711 (2020).
5. Y. Mugabo, S. Zhao, A. Seifried, S. Gezzar, A. Al-Mass, D. Zhang, J. Lamontagne, C. Attane, P. Poursharifi, J. Iglesias, E. Joly, M.-L. Peyot, A. Gohla, S. R. Murthy Madiraju, and M. Prentki, "Identification of a mammalian glycerol-3-phosphate phosphatase: role in metabolism and signaling in pancreatic beta-cells and hepatocytes," Proceedings of the National Academy of Sciences 113(4), 430–439 (2016).
6. E. Possik, S. R. Murthy Madiraju, and M. Prentki, "Glycerol-3-phosphate phosphatase/PGP: Role in intermediary metabolism and target for cardiometabolic diseases," Biochimie 143, 18–28 (2017).
7. P. K. Langston, A. Nambu, J. Jung, M. Shibata, H. I. Aksoylar, J. Lei, P. Xu, M. T. Doan, H. Jiang, M. R. MacArthur, X. Gao, Y. Kong, E. T. Chouchani, J. W. Locasale, N. W. Snyder, and T. Horng, "Glycerol phosphate shuttle enzyme GPD2 regulates macrophage inflammatory responses," Nature Immunology 20(9), 1186–1195 (2019).
8. J. Lu, Z. Xu, H. Duan, H. Ji, Z. Zhen, B. Li, H. Wang, H. Tang, J. Zhou, T. Guo, B. Wu, D. Wang, Y. Liu, Y. Niu, and R. Zhang, "Tumor-associated macrophage interleukin-β promotes glycerol-3-phosphate dehydrogenase activation, glycolysis and tumorigenesis in glioma cells," Cancer Science 111(6), 1979–1990 (2020).
9. C. Zhou, J. Yu, M. Wang, J. Yang, H. Xiong, H. Huang, D. Wu, S. Hu, Y. Wang, X.-Z. Chen, and J. Tang, "Identification of glycerol-3-phosphate dehydrogenase 1 as a tumour suppressor in human breast cancer," Oncotarget 8(60), 101309–101324 (2017).
10. P. Rusu, C. Shao, A. Neuerburg, A. A. Acikgöz, Y. Wu, P. Zou, P. Phapale, T. S. Shankar, K. Döring, S. Dettling, H. Körkel-Qu, G. Bekki, B. Costa, T. Guo, O. Friesen, M. Schlotter, M. Heikenwalder, D. F. Tschaharganeh, B. Bukau, G. Kramer, P. Angel, C. Herold-Mende, B. Radlwimmer, and H.-K. Liu, "GPD1 Specifically Marks Dormant Glioma Stem Cells with a Distinct Metabolic Profile," Cell Stem Cell 25(2), 241–257 (2019).
11. F. Lorenzetti, A. M. Capiglioni, R. A. Marinelli, M. C. Carrillo, and M. de Luján Alvarez, "Hepatic glycerol metabolism is early reprogrammed in rat liver cancer development," Biochimie 170, 88–93 (2020).
12. D. L. Nelson, M. M. Cox, and A. L. Lehninger, Lehninger principles of biochemistry, W. H. Freeman, New York, 2013.
13. F. Campos, T. Sobrino, P. Ramos-Cabrer, and J. Castillo, "Oxaloacetate: A novel neuroprotective for acute ischemic stroke," The International Journal of Biochemistry & Cell Biology 44(2), 262–265 (2012).
14. R. H. Swerdlow, R. Bothwell, L. Hutfles, J. M. Burns, and G. A. Reed, "Tolerability and pharmacokinetics of oxaloacetate 100 mg capsules in Alzheimer's subjects," BBA Clinical 5, 120–123 (2016).
15. H. M. Wilkins, S. Koppel, S. M. Carl, S. Ramanujan, I. Weidling, M. L. Michaelis, E. K. Michaelis, and R. H. Swerdlow, "Oxaloacetate enhances neuronal cell bioenergetic fluxes and infrastructure," Journal of Neurochemistry 137(1), 76–87 (2016).
16. G. R. Grimsley, S. R. Trevino, R. L. Thurlkill, and J. M. Scholtz, "Determining the conformational stability of a protein from urea and thermal unfolding curves," Current Protocols in Protein Science 71(1), 28.4.1–28.4.14 (2013).
17. C. G. Alexander, R. Wanner, C. M. Johnson, D. Breitsprecherc, G. Winterb, S. Duhrc, P. Baaskec, and N. Fergusona, "Novel microscale approaches for easy, rapid determination of protein stability in academic and commercial settings," Biochimica et Biophysica Acta (BBA) – Proteins and Proteomics 1844(12), 2241–2250 (2014).

Endofluorescence Imaging of Murine Hepatocellular Carcinoma Cell Culture by Fluorescence Lifetime Microscopy with Modulated CMOS Camera

Elena Potapova[1*], Evgeny Zherebtsov[1], Ksenia Kandurova[1], Alexander Palalov[1], Viktor Dremin[1,2], and Andrey Dunaev[1]

[1] Research and Development Center of Biomedical Photonics, Orel State University, 95 Komsomolskaya str., Orel 302026, Russia

[2] College of Engineering and Physical Sciences, Aston University, Aston Triangle, Birmingham B4 7ET, UK

*** e-mail:** potapova_ev_ogu@mail.ru

Abstract. In this work, we propose the results of pilot studies on using the modulated CMOS camera for the imaging of autofluorescence in murine hepatocellular carcinoma cells with excitation in UV light. Here, we assess the capabilities of the imaging system to detect changes in the NAD(P)H fractions produced and utilised in the glycolysis, pentose phosphate pathway and oxidative phosphorylation. Our results suggest that the camera and the system based on one possess a sufficient margin of SNR and sensitivity to detect the cellular metabolic changes associated with the metabolic pathways mentioned.
© 2022 Journal of Biomedical Photonics & Engineering.

Keywords: hepatocellular carcinoma; metabolism; frequency domain fluorescence lifetime imaging.

Paper #3464 received 17 Nov 2021; revised manuscript received 24 Feb 2022; accepted for publication 25 Feb 2022; published online 22 Mar 2022. doi: 10.18287/JBPE22.08.010303.

1 Introduction

Liver cancer is characterized by its rapid progression, so the issues of timely diagnosis and further treatment do not lose their relevance [1]. Improvement of medical diagnostic technology and the introduction of new modern methods can help to identify pathological changes at the initial stages and increase the effectiveness of traditional diagnostic procedures [2]. Biophotonics methods can be used to obtain data on the metabolic state of the liver and tumour tissues. In particular, fluorescence methods demonstrate high sensitivity to changes in the metabolic state of tissues. For this reason, the evaluation of the spectral and temporal parameters of fluorescence can serve as a diagnostic criterion, including in oncology [3]. Modern technologies allow combining fluorescent measurements with standard tools for minimally invasive surgery [4–7]. An important step in developing this approach is a fundamental study of the metabolic state of malignant cells to understand their biochemical processes better and correctly interpret the data obtained at the tissue and organ levels.

Uncontrolled tumour growth is accompanied by numerous disorders of redox balance and changes in metabolic pathways, including glycolysis and the pentose phosphate pathway [8]. The redox states of the NADH and NADPH pools play an important role in determining the activity of energy production paths, in managing oxidative stress and in maintaining antioxidant defence. Because the fluorescence spectra of NADH and NADPH are indistinguishable, interpretation of signals resulting from their combined fluorescence can be challenging [9]. At the same time, measurements of fluorescence intensity may be affected by inhomogeneous surface illumination, the presence of blood and photobleaching. Registering fluorescence lifetime can eliminate these limitations. This technology is sensitive to intermolecular interactions [10] and allows the recognition of endogenous fluorophores with overlapping spectra.

This work aimed to study the imaging of NAD(P)H autofluorescence intensity and lifetime parameters by a setup for fluorescence lifetime microscopy (FLIM) based on a camera with two-tap CMOS sensor for measurements in the frequency domain (pco.flim, PCO GmbH, Germany). The implementation of measurements in the frequency domain with the camera benefits from significantly lower prices for the equipment when compared with the equipment for FLIM imaging in the time domain. Previously, the camera was successfully used for widefield imaging of protoporphyrins in brain

tumours *in vivo* [11]. Nevertheless, the capabilities of the CMOS-based FLIM technique in the frequency domain for the imaging of weak NADH autofluorescence signals from cells require dedicated studies in the aspects of the sufficiency of their signal-to-noise ratio and sensitivity.

In this work, we evaluate NAD(P)H autofluorescence imaging using frequency domain, full-frame FLIM microscopy to identify changes in metabolic activity in the H33 hepatocellular carcinoma cell culture. The results obtained in this work may assist transition of the technique to medical practice to identify characteristic patterns of physiological parameters in hepatocytes and the cells of liver cancer, as well as to identify potential diagnostic criteria to distinguish them.

2 Materials and Methods

2.1 Experimental setup

The experimental setup (Fig. 1) included a frequency domain CMOS camera pco.flim (PCO AG, Germany) operated at the modulation frequency of 40 MHz and image resolution of 1008×1008 pixels. A 375 nm laser (PCO AG, Germany) was used to excite the autofluorescence in cells. The camera was connected to an inverted biological microscope, IX73 (Olympus Corporation, Japan) with a 40× objective. The exposure time of 500 ms was typically used for the images and results presented in the paper. The output power of the UV laser did not exceed 10 mW before coupling the microscopy system and was at the level of 0.7 mW in the field of view of the objective. The fluorescence lifetimes were estimated by the phase shift and the change in the modulation index of the recorded fluorescence radiation relative to the amplitude-modulated exciting radiation.

2.2 Cell culture

A cell culture of murine H33 hepatocellular carcinoma (HCC) was used as the object of study. H33 HCC were established from primary mouse tumours that were induced using a diethylnitrosamine/phenobarbital protocol and propagated by subcutaneous transfer between mice [12]. The cells were cultured in Dulbecco's modified Eagle medium (DMEM), supplemented with 10% of foetal bovine serum, penicillin and streptomycin, at 37 °C, 100% relative humidity, under an atmosphere containing 5% CO_2 and 95% air. Cells were placed in 35- mm dishes and measured after 3–4 days.

For inducing changes in metabolism in the cell culture of murine H33, well-known pharmacological agents were used, which can simulate various metabolic changes, including influence on redox states of the NADH and NADPH pools. Dehydroepiandrosterone (DHEA), iodoacetic acid (IA), Carbonyl cyanide-4-(trifluoromethoxy)phenylhydrazone (FCCP) and rotenone were all purchased from Sigma-Aldrich. The concentrations of pharmacological agents were chosen by standard or slightly exceeding the concentrations used to alternate metabolism in cultured cells. DHEA is a known non-competitive inhibitor of glucose-6-phosphate dehydrogenase (G6PDH), the rate-limiting step in the pentose phosphate pathway [13]. Iodoacetic acid (IA) is reported as an inhibitor of glycolysis, acting primarily on the enzyme glyceraldehyde-3-phosphate dehydrogenase, which catalyses the conversion of glyceraldehyde-3-phosphate into the high-energy phosphate compound, 1,3 bisphosphoglycerate with the reduction of NAD to NADH [14]. FCCP is a known uncoupling agent of the mitochondrial electron transport chain [15]. FCCP can disrupt ATP synthesis through uncoupling the proton gradient generated by the mitochondrial membrane. Rotenone acts as a strong inhibitor of complex I of the mitochondrial respiratory chain [16].

The measured cells included the control group (N = 9), one treated with iodoacetic acid (20 μM, N = 4) 2 h prior to measurements, and one treated with dehydroepiandrosterone (DHEA, 10 μM, N = 4) 15 min prior to measurements. The measurements included recording of the basal fluorescence signal, fluorescence signal after addition of oxidative phosphorylation uncoupler FCCP (0.2 mM), and complex I inhibitor rotenone (0.02 mM). The measurements lasted for 15 min.

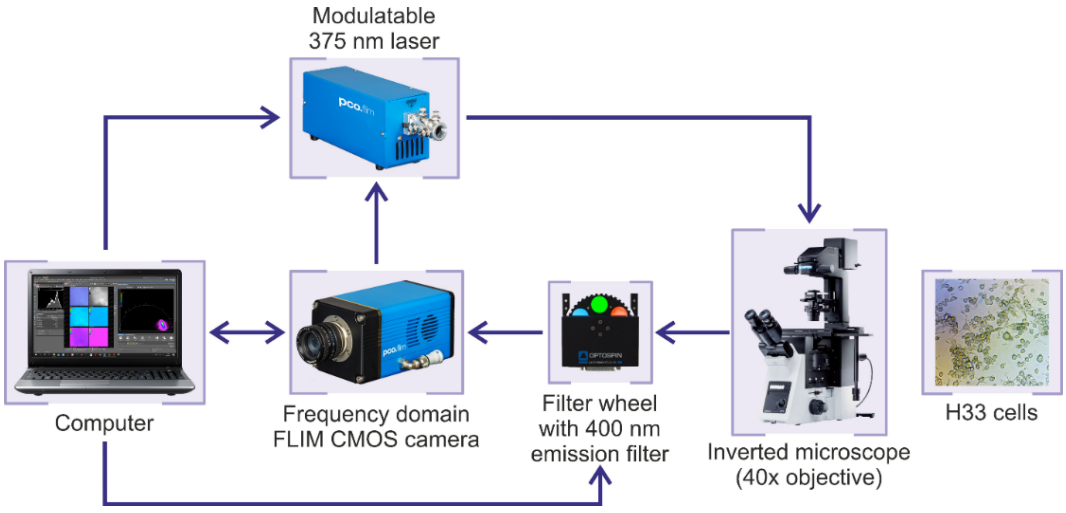


Fig. 1 Schematic diagram of the FLIM setup used for the imaging of H33 cells.

2.3 Fluorescence Measurements

Measurement of mitochondrial NADH autofluorescence in live cells was performed according to the algorithm described in Ref. [17]. After stabilizing the autofluorescence signal 1 μM FCCP was added to maximize mitochondrial respiration. Waited again to stabilize the autofluorescence signal and was added 1 mM rotenone which blocks the mitochondrial electron transport chain. The total NADH pool value in cells is the difference between the average fluorescence values after application of rotenone and the average fluorescence values after addition of FCCP provides. The averaged maximum fluorescence values obtained after rotenone addition and the averaged minimum fluorescence values obtained after FCCP addition represent 100% and 0% respectively. The values within the 0–100% scale represent the NADH redox index.

In this study, we measured bound and unbound NAD(P)H ratio using the phasor approach to FLIM [18–20]. The autofluorescence emitted in cells after excitation at a wavelength of 375 nm originates from NAD(P)H (free and bound) and FAD. When using an optical filter (400 nm), the fluorescence of NADN can be separated from the FAD contribution. Analysis of fluorescence lifetime in each pixel was carried out following the phasor approach to the FLIM. The phasor coordinates G and S in a pixel with coordinates i, j were calculated in the frequency domain:

$$\begin{aligned} \mathrm{G}_{i,j}(\omega) &= m_{i,j}\cos(\varphi_{i,j}), \\ \mathrm{S}_{i,j}(\omega) &= m_{i,j}\sin(\varphi_{i,j}), \end{aligned} \tag{1}$$

where $m_{i,j}$ and $\varphi_{i,j}$ are the measured modulation index and the phase shift of the emission with respect to the excitation. For each pixel, the lifetimes are calculated based on modulation index (τ_m) and the phase shift (τ_ϕ) as follows:

$$\begin{aligned} \tau_\phi &= \omega^{-1}\tan(\phi), \\ \tau_m &= \frac{1}{\omega}\sqrt{\frac{1}{m^2}-1}. \end{aligned} \tag{2}$$

2.4 Statistical Analysis and Images

Fluorescence lifetime parameters and final phasor plots were obtained using NIS-Elements software (Nikon Instruments Inc.). Comparisons between the studied groups were performed using the one-way analysis of variance (ANOVA test). Statistics tests and histograms generation were performed using OriginPro 2015 (OriginLab). Fluorescence intensity images and lifetime maps were processed using ImageJ (National Institutes of Health).

3 Results and Discussion

First, the imaging system was calibrated with a fresh 0.1 mM NADH solution. Representative examples of the phasor plot of autofluorescence were obtained from the NADH solution. Representative examples of the phasor plots of autofluorescence obtained from the NADH solution and HCC cells after the calibration procedures are shown in Fig. 2(a) and Fig. 2(b), respectively. The allocation of the points on the universal circle (Fig. 2(a)) suggests the pure single-exponential decay of the measured signal from the NADH solution. The distribution of the data points in images obtained from H33 cells had the shape of an oval inside the universal circle, which points to two-exponential decay in the time domain and the presence of two independent lifetimes in the mix of fluorescence agents in the cells.

Fig. 3 shows the fluorescence intensity (first column) and lifetime maps (colour) of phase shift (second column) and modulation index (third column) of murine H33 cells in the control (first line), IA (second line) and DHEA (third line) experiments.

The analysed parameters included NADH pool, NADH redox index, and phase and modulation indexes characterizing the first and second components of fluorescence lifetime decay (Fig. 4). The statistical significance of the differences was assessed using the one-way ANOVA test ($p < 0.05$).

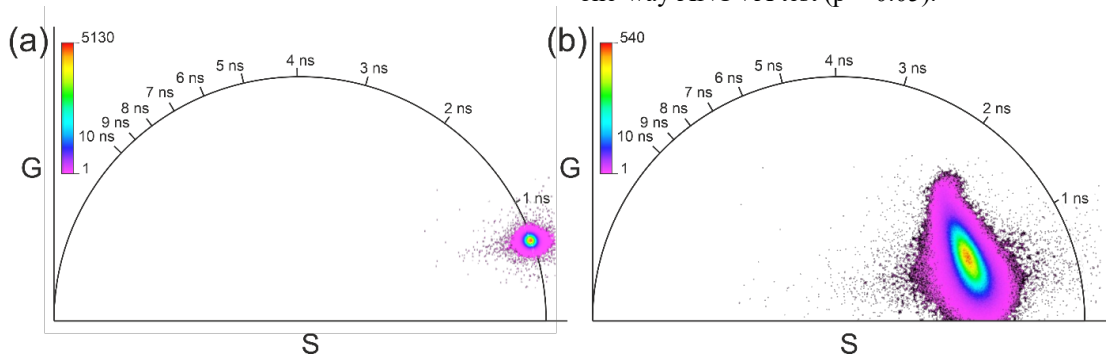


Fig. 2 Representative examples of the phasor plots of autofluorescence obtained from the NADH solution (a) and HCC cells (b).

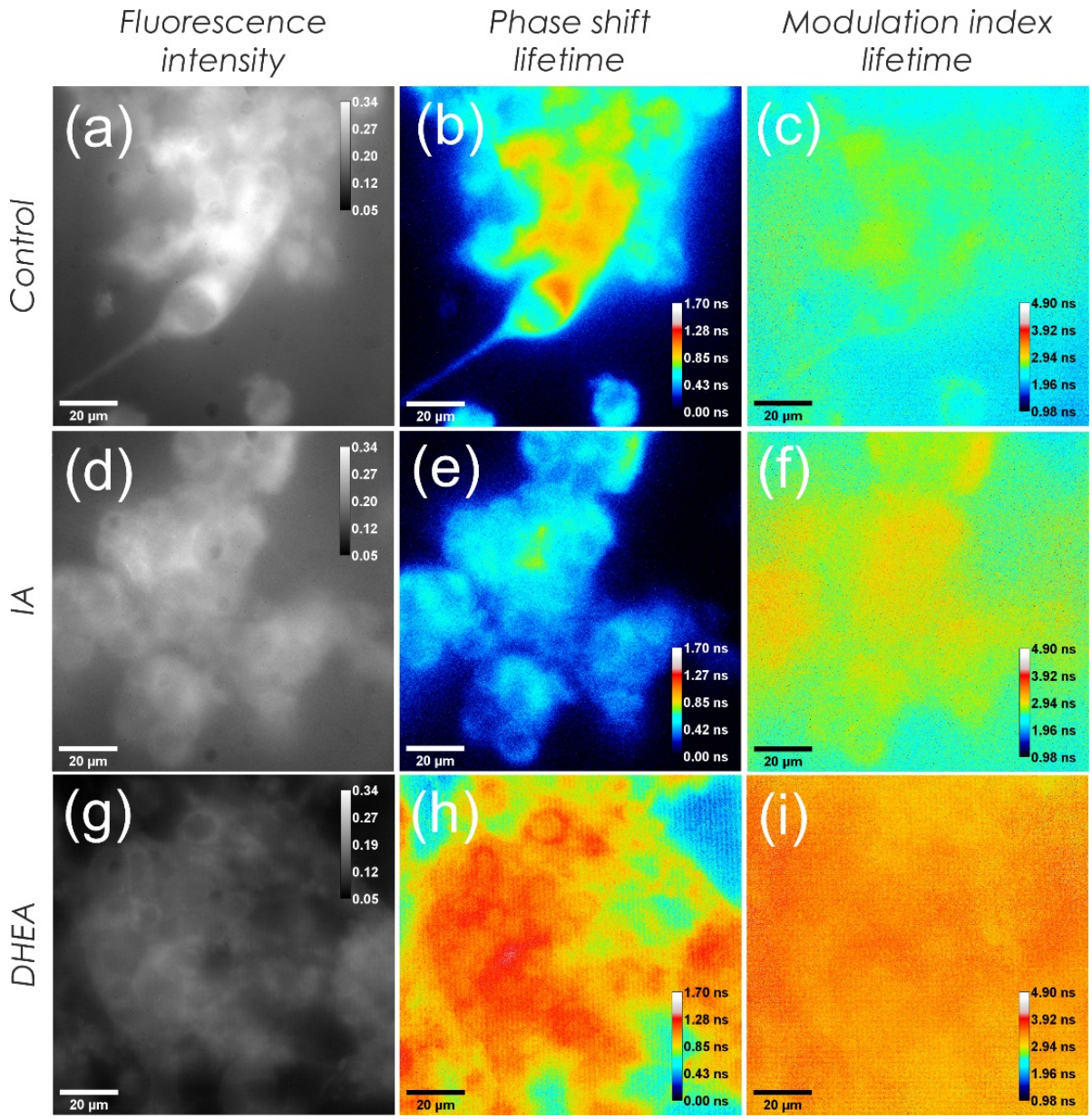


Fig. 3 Fluorescence intensity and lifetime maps (colour) of cells of murine H33 in control (a, b, c), iodoacetic acid (IA) (d, e, f) and dehydroepiandrosterone (DHEA) (g, h, i) experiments.

The results demonstrated a decrease in the average NADH pool, in both IA and DHEA groups (41 ± 27 a.u., 37 ± 7 a.u., 30 ± 18 a.u., respectively), while the NADH redox index increased by more in the IA group (53% ± 27%, 76% ± 16%, 70% ± 17%). Lower values of the redox index indicate more significant respiratory activity of cells. FCCP was used to uncouple ATP phosphorylation from the electron transport chain, resulting in unregulated, increased oxidation of NADH back to NAD. Uncoupling phosphorylation caused a decrease in the first and second components of the fluorescence lifetime in the control, IA and DHEA experiments. Inhibition of the activity of the electron transport chain by adding rotenone, a blocker of NADH dehydrogenase (complex I), increased the weighted lifetimes of the two components in all experiments. Therefore, it can be concluded that the application of inhibitors worsened the condition of the cells to different degrees. The observed changes may indicate that liver cancer cells use the process of glycolysis for glucose oxidation and energy production in the form of ATP to a greater extent than the pentose phosphate pathway. Inhibition of glycolysis is more critical for the viability of this cell culture. Inhibition of glycolysis IA led to a significant decrease in the first and second components of fluorescence lifetime decay in basal measurements (53.8% and 7.4%, respectively). In contrast, inhibition of the pentose phosphate pathway using DHEA led to a statistically significant increase in these parameters in the basic test (22.2% and 11.4% respectively). All three groups showed similar dynamics of changes. However, a significant scatter of the obtained values was observed in the control group, which made it difficult to assess in

more detail possible changes in the ratio of bound and unbound NAD(P)H.

In 1979, B. Chance described the idea that NADH autofluorescence can be used as a marker of the redox state of cells and cellular energy metabolism [21]. The intensity of autofluorescence with UV excitation mostly indicates the total amount of NADN. At the same time, NADH has short and long lifetime components, depending on its protein binding status. According to changes in the relative ratio of free and bound NADH, it is possible to estimate the cellular metabolic redox status [22]. In this study, we show that the frequency domain FLIM technique based on the two tap CMOS image sensor can be used as a valuable tool for non-invasive and marker-free study of metabolic changes in living cell cultures in vitro. Fluorescence lifetime is specific to molecular species, so the ratio of free/bound.

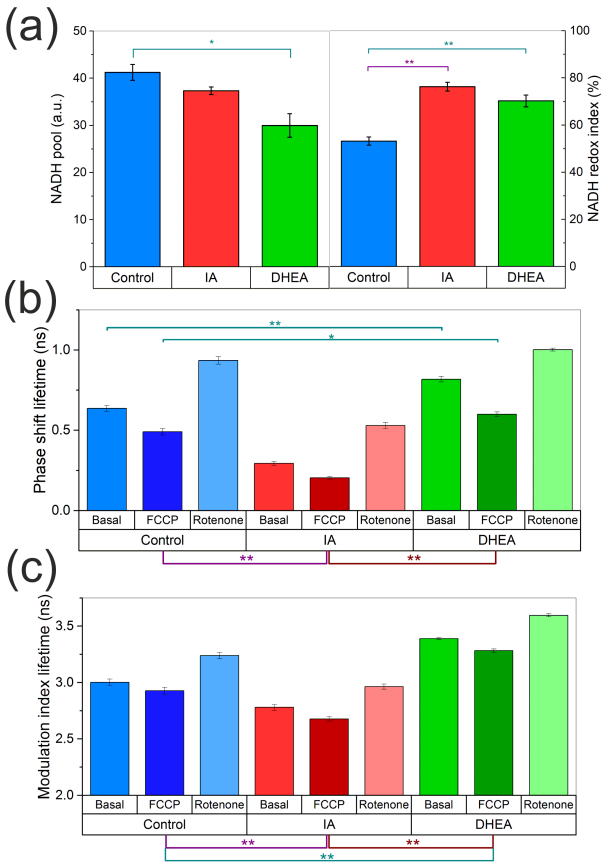


Fig. 4 Computed parameters NADH pool (a-left axis), NADH redox index (a-right axis), and phase shift (b) and modulation index (c) based fluorescence parameters characterizing the first and second components of fluorescence lifetime under varied metabolic conditions (IA – iodoacetic acid, DHEA – dehydroepiandrosterone, FCCP – carbonyl cyanide-4-(trifluoromethoxy) phenylhydrazone). A single SE was taken to plot error bars.

NADH can be measured in each pixel. This is important for expanding the understanding of tumour metabolic mechanisms. Earlier results obtained in the study of liver tumours using multiphoton microscopy FLIM with TCSPC system showed that Time-Domain FLIM can simultaneously display and quantify the cellular morphology and microenvironment of the living liver without fluorescent dyes [23, 24]. The key advantage of frequency-domain FLIM is its fast lifetime image acquisition; moreover, frequency-domain FLIM can be implemented without the use of costly pulsed lasers.

Raman microscopy can also be noted among the methods for studying the metabolic features of tumours [25]. Raman imaging allows one to examine cellular conditions in a non-invasive and non-destructive way. However, it is difficult to quantify metabolic changes in a single cell using only Raman microscopy. Most disadvantages of Raman spectroscopy are related to the weakness of the Raman effect, which leads to longer measurement times and possible damage to cells by thermal heating from the laser. However, it is worth mentioning the promising development of the combined Raman imaging and fluorescence lifetime imaging microscopy systems for diagnosis of cancer state and metabolic monitoring [26] and surface-enhanced Raman scattering (SERS) technique in Raman microscopy [27].

4 Conclusion

The obtained data on the application of the new type of frequency domain FLIM camera showed the feasibility of imaging the endogenous fluorescence and fluorescence lifetime parameters to be used for evaluating metabolic processes in cells. The preliminary studies with the imaging system allowed us to observe the criticality of glycolysis for the functioning of malignant cells.

The obtained results of the work and further research can become a scientific basis for the development of diagnostic methods for assessing mitochondrial function in liver tissues using *in vivo* fluorescence spectroscopy with time resolution.

Disclosures

All authors declare that there is no conflict of interests in this paper.

Acknowledgements

The authors acknowledge the support of the Russian Science Foundation under project No. 21-15-00325. The authors appreciate the technical support and valuable discussions of Dr. Gerhard Holst (PCO AG, Kelheim, Germany).

References

1. J. M. Llovet, R. K. Kelley, A. Villanueva, A. G. Singal, E. Pikarsky, S. Roayaie, R. Lencioni, K. Koike, J. Zucman-Rossi, and R. S. Finn, "Hepatocellular carcinoma," Nature Reviews Disease Primers 7(1), 6 (2021).
2. D. Mezale, I. Strumfa, A. Vanags, A. Kalva, D. Balodis, B. Strumfs, I. Fridrihsone, A. Abolins, and J. Gardovskis, "Diagnostic Algorithm of Hepatocellular Carcinoma: Classics and Innovations in Radiology and Pathology," Chapter 2 in Hepatocellular Carcinoma-Advances in Diagnosis and Treatment, C. T. Streba, C. C. Vere, and I. Rogoveanu, IntechOpen, UK, 2018.
3. M. M. Lukina, L. E. Shimolina, N. M. Kiselev, V. E. Zagainov, D. V Komarov, E. V Zagaynova, and M. V Shirmanova, "Interrogation of tumor metabolism in tissue samples ex vivo using fluorescence lifetime imaging of NAD (P) H," Methods and Applications in Fluorescence 8(1), 14002 (2019).
4. K. Kandurova, V. Dremin, E. Zherebtsov, E. Potapova, A. Alyanov, A. Mamoshin, Y. Ivanov, A. Borsukov, and A. Dunaev, "Fiber-Optic System for Intraoperative Study of Abdominal Organs during Minimally Invasive Surgical Interventions," Applied Sciences 9(2), 217 (2019).
5. V. Dremin, E. Potapova, E. Zherebtsov, K. Kandurova, V. Shupletsov, A. Alekseyev, A. Mamoshin, and A. Dunaev, "Optical percutaneous needle biopsy of the liver: A pilot animal and clinical study," Scientific Reports 10(1), 14200 (2020).
6. E. Zherebtsov, M. Zajnulina, K. Kandurova, E. Potapova, V. Dremin, A. Mamoshin, S. Sokolovski, A. Dunaev, and E. U. Rafailov, "Machine Learning Aided Photonic Diagnostic System for Minimally Invasive Optically Guided Surgery in the Hepatoduodenal Area," Diagnostics 10(11), 873 (2020).
7. E. A. Zherebtsov, E. V. Potapova, A. V. Mamoshin, V. V. Shupletsov, K. Y. Kandurova, V. V. Dremin, A. Y. Abramov, and A. V. Dunaev, "Fluorescence lifetime needle optical biopsy discriminates hepatocellular carcinoma," Biomedical Optics Express 13(2), 633–646 (2022).
8. L. Kou, X. Jiang, H. Huang, X. Lin, Y. Zhang, Q. Yao, and R. Chen, "The role of transporters in cancer redox homeostasis and cross-talk with nanomedicines," Asian Journal of Pharmaceutical Sciences 15(2), 145–157 (2020).
9. T. S. Blacker, M. R. Duchen, "Investigating mitochondrial redox state using NADH and NADPH autofluorescence," Free Radical Biology and Medicine 100, 53–65 (2016).
10. K. Suhling, P. M. W. French, and D. Phillips, "Time-resolved fluorescence microscopy," Photochemical & Photobiological Sciences 4(1), 13–22 (2005).
11. M. T. Erkkilä, B. Bauer, N. Hecker-Denschlag, M. J. M. Medina, R. A. Leitgeb, A. Unterhuber, J. Gesperger, T. Roetzer, C. Hauger, W. Drexler, G. Widhalm, and M. Andreana, "Widefield fluorescence lifetime imaging of protoporphyrin IX for fluorescence-guided neurosurgery: An ex vivo feasibility study," Journal of Biophotonics 12(6), e201800378 (2019).
12. N. L. Lazarevich, O. A. Cheremnova, E. V. Varga, D. A. Ovchinnikov, E. I. Kudrjavtseva, O. V. Morozova, D. I. Fleishman, N. V. Engelhardt, and S. A. Duncan, "Progression of HCC in mice is associated with a downregulation in the expression of hepatocyte nuclear factors," Hepatology 39(4), 1038–1047 (2004).
13. E. Köhler, H.-J. Barrach, and D. Neubert, "Inhibition of NADP dependent oxidoreductases by the 6-aminonicotinamide analogue of NADP," FEBS Letters 6(3), 225-228 (1970).
14. I. J. Bickis, J. H. Quastel, "Effects of metabolic inhibitors on energy metabolism of Ehrlich ascites carcinoma cells," Nature 205(4966), 44–46 (1965).
15. H. Terada, "Uncouplers of oxidative phosphorylation," Environmental Health Perspectives 87, 213–218 (1990).
16. G. Palmer, D. J. Horgan, H. Tisdale, T. P. Singer, and H. Beinert, "Studies on the respiratory chain-linked reduced nicotinamide adenine dinucleotide dehydrogenase: XIV. Location of the sites of inhibition of rotenone, barbiturates, and piericidin by means of electron paramagnetic resonance spectroscopy," Journal of Biological Chemistry 243(4), 844–847 (1968).
17. F. Bartolomé, A. Y. Abramov, "Measurement of Mitochondrial NADH and FAD Autofluorescence in Live Cells," in Mitochondrial Medicine, Human Press, New York, 263–270 (2015).
18. M. A. Digman, V. R. Caiolfa, M. Zamai, and E. Gratton, "The phasor approach to fluorescence lifetime imaging analysis," Biophysical Journal 94(2), L14–L16 (2008).
19. C. Stringari, A. Cinquin, O. Cinquin, M. A. Digman, P. J. Donovan, and E. Gratton, "Phasor approach to fluorescence lifetime microscopy distinguishes different metabolic states of germ cells in a live tissue," Proceedings of the National Academy of Sciences 108(33), 13582–13587 (2011).
20. M. Y. Berezin, S. Achilefu, "Fluorescence lifetime measurements and biological imaging," Chemical Reviews 110(5), 2641–2684 (2010).
21. B. Chance, B. Schoener, R. Oshino, F. Itshak, and Y. Nakase, "Oxidation-reduction ratio studies of mitochondria in freeze-trapped samples. NADH and flavoprotein fluorescence signals," Journal of Biological Chemistry 254(11), 4764–4771 (1979).
22. D. K. Bird, L. Yan, K. M. Vrotsos, K. W. Eliceiri, E. M. Vaughan, P. J. Keely, J. G. White, and N. Ramanujam, "Metabolic mapping of MCF10A human breast cells via multiphoton fluorescence lifetime imaging of the coenzyme NADH," Cancer Research 65(19), 8766–8773 (2005).

23. H. Wang, X. Liang, Y. H. Mohammed, J. A. Thomas, K. R. Bridle, C. A. Thorling, J. E. Grice, Z. P. Xu, X. Liu, and D. H. G. Crawford, "Real-time histology in liver disease using multiphoton microscopy with fluorescence lifetime imaging," Biomedical Optics Express 6(3), 780–792 (2015).
24. S. Rodimova, D. Kuznetsova, N. Bobrov, V. Elagin, V. Shcheslavskiy, V. Zagainov, and E. Zagaynova, "Mapping metabolism of liver tissue using two-photon FLIM," Biomedical Optics Express 11(8), 4458–4470 (2020).
25. S. Elumalai, S. Managó, and A. C. De Luca, "Raman Microscopy: Progress in Research on Cancer Cell Sensing," Sensors 20(19), 5525 (2020).
26. L. Becker, N. Janssen, S. L. Layland, T. E. Mürdter, A. T. Nies, K. Schenke-Layland, and J. Marzi, "Raman Imaging and Fluorescence Lifetime Imaging Microscopy for Diagnosis of Cancer State and Metabolic Monitoring," Cancers 13(22), 5682 (2021).
27. S. Z. Al-Sammarraie, L. A. Bratchenko, E. N. Typikova, P. A. Lebedev, V. P. Zakharov, and I. A. Bratchenko, "Silver Nanoparticles-Based Substrate for Blood Serum Analysis under 785 nm Laser Excitation," Journal of Biomedical Photonics & Engineering 10301 (2022).

Invasive and minimally invasive optical detection of pigment accumulation in brain cortex

Luís R. Oliveira[1], Tânia M. Gonçalves[2], Maria R. Pinheiro[2], Luís E. Fernandes[3], Inês S. Martins[1,3], Hugo F. Silva[1], Hélder P. Oliveira[4,5], Valery V. Tuchin[6,7,8], and Luís M. Oliveira[1,2*]

[1] Center of Innovation in Engineering and Industrial Technology, ISEP, Rua Dr. António Bernardino de Almeida 431, Porto 4249-015, Portugal

[2] Physics Department, School of Engineering, Polytechnic Institute of Porto, Rua Dr. António Bernardino de Almeida 431, Porto 4249-015, Portugal

[3] Faculty of Engineering, University of Porto, FEUP, Porto 4200-465, Portugal

[4] Institute for Systems and Computer Engineering, Technology and Science, INESC TEC, Porto 4200-465, Portugal

[5] Faculty of Science, University of Porto, FCUP, Porto 4169-007, Portugal

[6] Science Medical Center, Saratov State University, 83 Astrakhanskaya str., Saratov 410012, Russia

[7] Laboratory of Laser Molecular Imaging and Machine Learning, Tomsk State University, 36 Lenin's av., Tomsk 634050, Russia

[8] Laboratory of Laser Diagnostics of Technical and Living Systems, Institute of Precision Mechanics and Control, FRC "Saratov Scientific Centre of the Russian Academy of Sciences", 24 Rabochaya str., Saratov 410028, Russia

*** e-mail:** lmo@isep.ipp.pt

Abstract. The estimation of the spectral absorption coefficient of biological tissues provides valuable information that can be used in diagnostic procedures. Such estimation can be made using direct calculations from invasive spectral measurements or though machine learning algorithms based on noninvasive or minimally invasive spectral measurements. Since in a noninvasive approach, the number of measurements is limited, an exploratory study to investigate the use of artificial generated data in machine learning techniques was performed to evaluate the spectral absorption coefficient of the brain cortex. Considering the spectral absorption coefficient that was calculated directly from invasive measurements as reference, the similar spectra that were estimated through different machine learning approaches were able to provide comparable information in terms of pigment, DNA and blood contents in the cortex. The best estimated results were obtained based only on the experimental measurements, but it was also observed that artificially generated spectra can be used in the estimations to increase accuracy, provided that a significant number of experimental spectra are available both to generate the complementary artificial spectra and to estimate the resulting absorption spectrum of the tissue.
© 2022 Journal of Biomedical Photonics & Engineering.

Keywords: tissue spectroscopy; diffuse reflectance; absorption coefficient; brain cortex; DNA content; blood content; pigment detection; machine learning; generative models.

Paper #3467 received 05 Dec 2021; revised manuscript received 07 Mar 2022; accepted for publication 08 Mar 2022; published online 28 Mar 2022. doi: 10.18287/JBPE22.08.010304.

1 Introduction

Biological tissues differ one from the other in various aspects, since they can have differentiated contents of biological components inside, a different state of health and a different age. The evaluation of such parameters from tissues is not always easy. An example is the evaluation of the tissue state of health in the initial stages of cancer development, since the early-stage formation of cancer cells and the small changes created by those cells

in the surrounding environment are not detected by visual inspection.

Optical methods can help in such evaluations, since any small change in tissue physiology or morphology will translate in changes on the tissue's optical properties [1, 2]. The measurement of the spectral optical properties from similar tissues, such as the refractive index (RI) or the absorption coefficient (μ_a) in a wide spectral range [3] allows to acquire and compare information regarding the contents of proteins, blood and lipids. Detected differences of these contents can be used as bio-optical markers to identify and discriminate pathologies such as cancer [1] or diabetes [4, 5]. Such spectral evaluation also allows to detect the presence of pigments, such as melanin or lipofuscin, whose accumulation in tissues has been reported to be related to the ageing process [6] or to the development of cancer [7, 8]. The evaluation of the scattering coefficient (μ_s), or the reduced scattering coefficient (μ'_s) in a wide spectral range may also be useful to discriminate pathological from healthy tissues. Studies have showed that pathology-induced changes in tissue structure translate in a change of form and magnitude of the μ_s and μ'_s spectra [1, 9].

Considering the potential of the optical methods to acquire diagnostic information, both the RI and the μ_a spectra are sensitive to the absorption bands of tissue chromophores and can be used in the detection of pathology-discriminating information with higher accuracy [10–12]. Considering the identification, quantification and content discrimination of chromophores and pigments between healthy and pathological tissues, the analysis of the spectral μ_a ($\mu_a(\lambda)$) has proven to be more useful [1, 2, 13–15].

The evaluation of $\mu_a(\lambda)$ has been traditionally made through the use of inverse simulations, whose computational codes are based on the Monte Carlo or the Adding-Doubling algorithms [16–18]. These simulation codes require some optical measurements as input, such as the total transmittance (T_t), the total reflectance (R_t), the collimated transmittance (T_c) and the RI of the tissue [16–18]. All these measurements must be acquired from the tissue under study, and although the R_t and RI data can be measured with a noninvasive or minimally invasive procedure from *in vivo* tissues, the T_t and T_c measurements require a more invasive approach and are more commonly made from *ex vivo* tissue samples [19]. Another disadvantage of the traditional simulation methods is that the available codes perform a simulation at a time for individual wavelengths. This means that to acquire the necessary data to reconstruct the $\mu_a(\lambda)$ of a particular tissue for a broad spectral range, one needs to perform a large number of simulations. As recently reported [1, 2, 11, 13–15], such time and computer demanding approach can be replaced by a faster method to calculate the $\mu_a(\lambda)$ of the tissue in a few seconds. This calculation method still needs the T_t and R_t spectra from *ex vivo* tissues, but if those spectra are available, the entire $\mu_a(\lambda)$ can be obtained immediately [1, 13].

To explain this new calculation approach we consider a hypothetical biological tissue sample with slab-form and fixed thickness, d, that consists of a medium where light absorption dominates over light scattering. If this sample is excited by a collimated light beam with intensity $I_0(\lambda)$, then the Bouguer-Beer-Lambert law can be used to calculate the transmitted light intensity, $I(\lambda)$ [13, 20]:

$$I(\lambda) = I_0(\lambda) e^{-A_b(\lambda)}, \quad (1)$$

where $A_b(\lambda)$ represents the absorbance spectrum of the tissue sample that is defined as [13, 20]:

$$A_b(\lambda) = -ln\left(\frac{I(\lambda)}{I_0(\lambda)}\right) = \mu_a \times d. \quad (2)$$

Eq. (2) can be used to calculate the $\mu_a(\lambda)$ of the tissue under study from the measured transmitted spectrum. In reality, biological tissues also have significant scattering properties, meaning that a light beam of intensity $I_0(\lambda)$ that irradiates a slab-form tissue sample will be fractioned into three distinct forms, which correspond to the three optical phenomena that occur [19]: light absorption, light transmission and light reflection. Provided that the transmitted light and the reflected light spectral fraction ratios ($T_t(\lambda)$ and $R_t(\lambda)$, respectively) can be measured from the sample, the $A_b(\lambda)$ of the sample can be calculated using the following relation [1, 12]:

$$T_t(\lambda) + R_t(\lambda) + A_b(\lambda) = 1. \quad (3)$$

The calculation with Eq. (3) is possible for any tissue with dominating absorption, with dominating scattering or with a combination of absorption and scattering properties. The combination of Eqs. (2) and (3) allows to calculate the $\mu_a(\lambda)$ of the tissue from the $T_t(\lambda)$ and $R_t(\lambda)$ that were measured from the slab sample [1]:

$$\mu_a(\lambda) = \frac{1-[T_t(\lambda)+R_t(\lambda)]}{d}. \quad (4)$$

The measuring setups used to acquire the T_t and R_t spectra use integrating spheres and these ratios are represented in arbitrary units. Consequently, from Eq. (4), $\mu_a(\lambda)$ will be represented in cm^{-1} (or mm^{-1}), depending on the units that d was measured (cm or mm). Although this is a fast procedure to obtain $\mu_a(\lambda)$ of a tissue, it still depends on measurements from excised tissue samples.

Since the main objective of applying optical technologies to clinical practice is to provide efficient diagnostic or treatment approaches that can be made *in vivo*, without excising tissues from the patient, other ways to obtain $\mu_a(\lambda)$ must be searched. One possible approach relies on the acquisition of diffuse reflectance (R_d) spectra, a measurement procedure which can be applied with noninvasive or minimally invasive approaches to *in vivo* tissues [2]. In opposition to the calculations made with Eq. (4), there is no direct relation between the R_d and μ_a spectra. A possible estimation method to reconstruct the $\mu_a(\lambda)$ from spectral R_d measurements relies on the use of machine learning (ML)

techniques and its viability was demonstrated in a recent study with human healthy and pathological colorectal mucosa tissues [2]. Although one of the challenges in the application of ML algorithms in the field of biophotonics is the reduced number of datasets to build the ML models [21], the estimations of the mean μ_a spectra of the colorectal mucosa tissues reported in Ref. [2] were made with acceptable accuracy using only 10 R_d spectra from each tissue. The reconstructed μ_a spectra of both colorectal mucosa tissues were averaged and allowed to obtain discriminated lipofuscin contents in healthy and pathological tissues, showing similar contents to the ones obtained with direct calculations as described by Eq. (4).

The results presented in Ref. [2], although obtained with a small number of datasets to train the algorithms, open the way to apply ML methods to noninvasive tissue spectroscopy measurements for the development of new noninvasive diagnostic procedures. To increase the accuracy of the training process in the development of ML algorithms, a large number of spectra is necessary, but sometimes that is not possible in biophotonics. In some cases, it is not possible to get a large number of tissue samples from different patients or animals to perform the necessary spectral measurements. Another drawback is that for some tissues, no matter how many spectra are measured, they will all be very similar and data variability will be small. New spectra that provide repeated information will be superfluous in the training of ML algorithms and will imply a longer time in the training process. Another option to improve the accuracy of the ML algorithms is to increase the number of available training data by generating new datasets digitally when they are not available experimentally. Such option can be done, but some attention must be made to avoid changing the spectral features, and ensure that the generated spectra are characteristic of the tissue under study. Such artificial generation of spectra can be done using Generative Adversarial Networks (GANs), which is a recent class of ML models that are commonly used to generate new artificial samples of data from a random input [22]. Such procedure is possible since GANs are composed by two distinct ML models, the generator and the discriminator, and they cooperate in a zero-sum game to learn how to generate new synthetic data [23]. The generator model learns how to create new data from random noise and its goal is to fool the discriminator. In contrast, the discriminator will try to differentiate between the generated data and the real experimental data. By the end of the learning process, the generator should be able to artificially create new data that is similar to the already pre-existing experimental data [24]. GANs can be used to generate both new R_d and new μ_a spectra to increase the number of available samples to train and validate other ML models that estimate the μ_a spectra from noninvasive-type R_d spectral measurements. By increasing the available dataset in the algorithms that recreate the μ_a spectra, it is expected that the ML models will become more robust to input variance and avoid overfitting. The use of GANs to increase the number of datasets opens other possibilities, and such method was used in the present work, as described in Subsection 2.4.

The optical study of brain tissues is of great interest, since the brain is the most complex organ in the body and few studies regarding the spectral optical properties of its tissues have been performed so far. Such interest in the optical studies of brain tissues regards also the high incidence of brain diseases, such as stroke, Parkinson or Alzheimer, in the past 30 years [25]. The ageing process of the brain tissues is directly related to the occurrence of these diseases, since as tissues become older neuron degeneration and death occurs more rapidly [26–28]. To prevent the occurrence of these diseases, a monitoring procedure to evaluate neuron ageing, degeneration and death is most desirable. Optical methods can be used in the development of such procedures, but to do so, the knowledge of the spectral optical properties of the brain tissues in a wide spectral range is necessary. With such knowledge, the development of optical procedures to perform superficial or in-depth monitoring assisted by optical clearing treatments of the health of brain tissues can be possible [19, 29, 30]. Considering such goals to develop new optical methods to monitor tissue's health and ageing in the brain, we performed a study to discriminate and identify the pigment contents in the brain cortex. This study was made using tissue samples from the brain of adult rabbits and consisted on performing spectral measurements to be used both in the direct calculation of the spectral μ_a and in its estimation through ML algorithms. The methodology used in the present study is described in Section 2 and the results are presented in Section 3.

2 Materials and methods

Since the objective of the present study was to obtain and analyze the $\mu_a(\lambda)$ of the brain cortex through different methods, *ex vivo* samples were collected from the brain of rabbits. The selection of the rabbit brain to collect the samples to use in our study was based on that the rabbit and the human brains are very similar, since both have the same three divisions with a fore brain, a mid brain and a hind brain, and also because both contain the cerebellum, the medulla, the corpus callosum, the hypothalamus and the pituitary gland [31].

The research here described is accordingly with the Declaration of Helsinki and was approved by the research review board in biomedical engineering of the Center of Innovation in Engineering and Industrial Technology (CIETI), in Porto, Portugal. Such approval has the number CIETI/Biomed_Research_2021_01. Due to the fact that this study consisted only on the evaluation of the $\mu_a(\lambda)$, both by direct calculation from experimental measurements and by estimation through ML, the following subsections describe the experimental, calculation and estimation procedures adopted.

2.1 Tissue collection and preparation

Ten adult grey rabbits, having a similar age near 36 months, were acquired from a breeder near our lab in

Porto (Portugal), who sells the animals for consumption. The measurements were made with two cortex brain samples from each animal in different days.

For each study with samples from a particular animal, the rabbit was sacrificed in the previous day and the brain was removed from the skull and frozen for 12 h. After this period, tissue samples were sliced from the cortex using a cryostat (Leica™, Wetzler, Germany, model CM1860 UV). Twenty samples were prepared in total, having an approximated circular form ($\phi \sim 1$ cm) and a fixed thickness of 0.5 mm. All these samples were submitted to spectral measurements, which are described in Subsection 2.2.

2.2 Spectral measurements

To obtain the $\mu_a(\lambda)$ of the brain cortex by direct calculation, two types of spectral measurements were made, using the T_t and R_t setups represented in Fig. 1(a) and in Fig. 1(b). A total number of 10 cortex samples, collected from five adult rabbits, was used to acquire both the T_t and R_t spectra with these setups. These measurements were made in an earlier stage of the research and the corresponding results were already published [13].

At a later stage of the research, other 10 cortex samples were collected from other five adult rabbits and prepared in the same manner to be used in the acquisition of the R_d spectra, which was necessary for the ML estimations. Such measurements were made using the setup presented in Fig. 1(c).

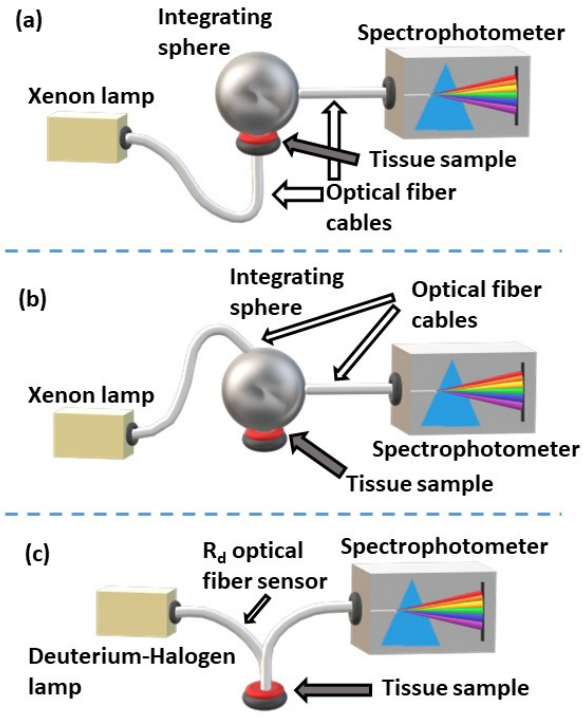


Fig. 1 Experimental setups to measure: $T_t(\lambda)$ (a), $R_t(\lambda)$ (b) and $R_d(\lambda)$ (c).

Considering the measurements with the T_t setup, a broadband pulsed Xenon lamp emits a beam that is delivered below the sample through an optical fiber cable (core diameter of 600 μm). A collimating lens located at the tip of the cable below the sample collimates the beam with a 6 mm diameter. Such beam is transmitted by the tissue sample and then is submitted to several reflections inside the integrating sphere (integration), before being delivered to the spectrometer through a similar optical fiber cable.

Considering the R_t setup presented in Fig. 1(b), the exciting beam that is also emitted by the pulsed Xenon lamp is delivered to an upper entrance of the integrating sphere through an optical fiber cable (core diameter of 600 μm) and collimating lens. The collimated beam with 6 mm in diameter is directed to an exciting direction that makes 8° with the vertical axis of the integrating sphere to guarantee that both specular and diffuse reflectance occur at the tissue surface. After the reflection occurs at the tissue surface, the reflected beam is directed into the inside of the sphere where it is reflected several times at its internal surface (integration), before exiting to be delivered to the spectrometer through a similar optical fiber cable.

In the case of the R_d setup presented in Fig. 1(c), the sample was excited with a broadband deuterium-halogen lamp. An R_d optical fiber sensor, which was kindly supplied by ArtPhotonics™ (Berlin, Germany) for our research, was used both to irradiate the sample and to collect the diffuse reflected light from it. This sensor contained a detection fiber at the center, which was surrounded by seven irradiation fibers, all made of silica with a core diameter of 400 μm and a cladding thickness of 20 μm. The numerical aperture of these fibers was 0.22. The detection fiber at the center was covered with aluminum, having a total diameter of 560 μm. The exciting fibers were covered by polyamide and their total diameter was 465 μm. Such fibers were packed around the detection fiber, without any spacing, having a source-detector separation of 512.5 μm. The tip of the R_d sensor was kept fixed at 2 mm distance above the tissue sample surface during measurements. Apart from the R_d sensor, all the equipment used in the setups presented in Fig. 1 were acquired from Avantes™ (Apeldoorn, The Netherlands).

The reason for using two different lamps in the different measurement setups is that for the case of integrated measurements (T_t and R_t), a high intensity signal is needed for the integration process inside the integrating sphere, and a small intensity signal for the R_d measurements to avoid saturation of the spectrometer. Although two different lamps were used in the T_t / R_t and R_d setups, the spectral measurements in all cases were not influenced by the spectral characteristics of the lamps. For each particular set of measurements, the setup of the spectrometer was made to measure the T_t, R_t or R_d spectra directly. The calculations of these spectra are made by the software of the spectrometer, based on the transmitted or reflected spectra that are measured from the sample and the reference spectra of the lamp used in each setup.

The reflectance reference used both in the R_t and R_d setups was the RS-2 reflectance reference from Avantes, with a reflectance above 92% in the entire spectral range considered in this study.

As referred above, 10 spectra were acquired with each of the setups presented in Fig. 1. These spectra were measured between 200 and 1000 nm. The spectra acquired with the T_t and R_t setups were used in a direct calculation of the $\mu_a(\lambda)$ of the brain cortex, while the spectra acquired with the R_d setup were used as input to the ML algorithms to estimate $\mu_a(\lambda)$ of the brain cortex and compare with the one that results from direct calculations. Subsection 2.3 describes the direct calculations from the experimental measurements, while Subsection 2.4 describes the procedure used in the ML approach.

2.3 Calculations

After performing all spectral measurements with the setups presented in Fig. 1(a) and Fig. 1(b), calculations were made to obtain the $\mu_a(\lambda)$ of the brain cortex. Since 10 spectra were obtained with each measurement setup, 10 μ_a spectra were calculated using Eq. (4). In each of these calculations, a pair of T_t and R_t spectra were used along with the sample thickness, d. Considering the 10 μ_a spectra that resulted from these calculations, the mean $\mu_a(\lambda)$ and corresponding standard deviation (SD) were calculated.

A further analysis of the mean $\mu_a(\lambda)$ showed evidence of pigment content in the brain cortex, meaning that additional calculations were necessary to identify those pigments and discriminate their content. According to literature [32], the brain is known to accumulate mainly melanin and lipofuscin. These pigments originate from their precursors, such as *L*-tyrosine, *L*-cysteine, and dopamine (in the case of melanin) [6] and from cell organelles, such as mitochondria, Golgi apparatus, and lysosomes (in the case of lipofuscin) [33–35]. These precursors can easily associate with metals, specially iron, to form melanin and lipofuscin [36].

Considering that the resulting mean $\mu_a(\lambda)$ that was calculated directly from the experimental measurements represents the mean absorption coefficient of the cortex between 200 and 1000 nm, we looked for the absorption spectra of these pigments on literature. Ref. [37] presents the absorption spectrum of melanin and Ref. [38] presents the absorption spectrum for lipofuscin in the same wavelength range that we considered in our study. We retrieved numerical data from the graphs in these two references and reconstructed the absorption spectra for melanin and for lipofuscin. A graph containing both spectra is presented in Section 3. After obtaining these absorption spectra for the pigments, an optimized combination of both was calculated to subtract to the mean $\mu_a(\lambda)$ of the brain cortex, in a way that such reconstructed absorption presents a horizontal baseline. The results of this calculation and an equation that describes the pigment combination that was used are presented in Section 3.

2.4 Machine Learning estimations

After calculating the $\mu_a(\lambda)$ of the brain cortex directly from the experimental measurements and making an analysis to discriminate the melanin and lipofuscin content in this tissue, another study was made to check if the same results were reachable from a minimally invasive approach.

To proceed with a measuring technique that approaches noninvasive or minimal invasive measurements that can be done *in vivo*, R_d spectra were also acquired from similar tissue samples for the same wavelength range (200–1000 nm). These 10 spectra consist on a reduced number of samples to train the ML algorithms in the reconstruction of the μ_a spectra, but to increase the number of samples to train the algorithms, we first used GANs to artificially generate new R_d and new μ_a spectra from the experimental ones. The objective of this initial process was to turn the ML models that estimate μ_a more robust and decrease their overfitting tendency.

The process of data augmentation with the GANs models consists on the following steps:

a) generate a new artificial spectrum from random noise using the generator,
b) train the discriminator using the both the experimental and the generated spectrum,
c) update the parameters of the generator using the discriminator loss (error metric).

Due to the dynamics between the generator and the discriminator, the GANs model convergence is not a stable state. This happens because there is a certain point in the training process where the generator is so good that the discriminator starts to guess if the new data is real or artificial, which in turn gives the generator deceitful feedback. To prevent this from happening, the training process was stopped when the average of the generated spectra was the closest to the mean experimental data. Another important factor when training GANs models is the learning rate of the generator and the discriminator. As an example, if the discriminator converges earlier than the generator, it increases the chances of model collapse, where the generator only produces one type of sample in an attempt to fool the discriminator. The learning rate was sweep between the 0.001–0.000001 values and then fixed at 0.0001 due to the fact that further decreases did not contribute to a better performance of the GANs model. Additionally, the neural networks that compose the GANs model were defined with different architectures. The discriminator had five layers, being the first two composed with 801 nodes, the third with 600 nodes, the fourth with 400 nodes, and the fifth with 1 node. The generator had five layers, with all the layers having 801 nodes, with the exception of the third, which has only 600 nodes.

During the training process, one of the GANs model was trained to generate new R_d spectra and the other was trained to generate new μ_a spectra. Since these two GANs models converge at different times, the number of epochs for the GANs model that generated new R_d spectra was set to 7901, while the number of epochs for the GANs

model that generated new μ_a spectra was set to 1301. After training and fine tuning of the GANs models, the new generated data was plotted and compared to the experimental data, showing good agreement (presented in Section 3).

After training the GANs models, they were used to generate new spectra in groups of 10, 50 and 100 to train the other ML models in solving the regression problem of recreating the μ_a spectra from the measured R_d spectra. To improve the overall spectral shape of the generated spectra, a Savitzky-Golay filter was applied to smooth the spectra. For each group of generated spectra, three experiments were conducted:

a) in the first experiment, the ML models were trained with the generated spectra and tested with the experimental spectra (G/E),
b) in the second experiment, the ML models were trained with the experimental spectra and tested with the generated spectra (E/G),
c) in the third experiment, both the generated and experimental spectra were combined altogether (AT) to be used in the training and testing of the ML model.

In this last experiment, the generated and experimental spectra were split in an 80/20 proportion to be used in the training and testing procedures to evaluate the performance of the ML model. As an example, for the group of 10 generated spectra, we assured that the test dataset consisted on 8 experimental and 2 generated spectra. A separate experiment was made for the ML model, where no generated spectra were used both in the training and testing process. In this case, the Leave One Out (LOO) method was used to obtain a performance reference point, as we did in our previous work with data from the human colorectal tissues [2].

Similarly to what has been done during the generation of spectra with the GANs models, the Single Layer Perceptron (SLP), the K-Nearest Neighbor (KNN) and the Random Forest Regressor (RFR) algorithms were fine tuned to achieve the best performance possible. These algorithms were the ones with the best performance in our previous study [2]. For this reason, we selected them to use in the present study. The SLP was set with two layers, the first one having 10 nodes and the second having 801 nodes. The learning process was set at 0.001 and the number of epochs was set at 50 during the three experiments that were described above. For the KNN and the RFR algorithms, the number of neighbors and the number of trees where set to 3 and 4, respectively. Further increments in these hyper parameters increase the computational cost of the ML models with no apparent increase in performance.

To quantify the performance of the ML models in the estimation of the μ_a spectra, the Euclidean Distance (ED) between the mean estimated spectrum (MES) and the mean reference spectrum (MRS) was calculated using Eq. (5) [21]:

$$ED = |a - b|, \quad (5)$$

where a is the μ_a value of the mean estimated spectrum (MES) and b is the μ_a value of the mean reference spectrum (MRS), with the MES calculated from the individual generated spectra and the MRS calculated from the individual experimental spectra.

The results obtained from the GANs and ML estimations and ED comparative graphs to select the best ML algorithm for μ_a generation from the R_d spectra are presented in Section 3. The calculations to retrieve the pigment combination from the $\mu_a(\lambda)$ generated by the best method are also presented to show that pigment content evaluation is possible with a minimally invasive approach.

3 Results

Since the present study was conducted with experimental measurements to obtain the $\mu_a(\lambda)$ of the brain cortex, both by direct calculation and through ML estimations, the presentation of results is divided in various subsections. Subsection 3.1 presents the mean experimental spectra that were used in the various stages of this study. Subsection 3.2 presents the results obtained with the direct calculation approach and Subsection 3.3 presents the results estimated through ML. Subsection 3.4 presents the evaluation of the pigment content, both from the direct calculation and from the ML estimation approaches.

3.1 Spectral measurements

The first step of the present study consisted on acquiring spectral measurements with all the setups in Fig. 1. As indicated in Subsection 2.2, 10 T_t and 10 R_t spectra were acquired from 10 cortex samples at an initial stage. At a later stage 10 R_d spectra were acquired from 10 similar cortex samples. The samples used in these measurements were all collected from adult rabbits acquired from the same supplier. The mean and SD of the T_t, R_t and R_d spectra that resulted from these measurements are presented in Fig. 2.

The wavelength dependencies for all mean spectra presented in Fig. 2 are accordingly to others previously obtained from other biological tissues [1, 2, 12, 14, 15]: T_t increases with the wavelength and both R_t and R_d decrease with the wavelength. All mean spectra in Fig. 2 present good sensitivity to the absorption bands of DNA/RNA (260 nm) and hemoglobin/myoglobin (274, 415, 540 and 570 nm). The mean T_t spectrum also shows evidence of water in the tissues – absorption band centered at 980 nm.

Regarding the SD, the R_d spectrum presented in Fig. 2(c) shows small magnitude (less spreading between samples in these measurements) for the entire spectral range. In the case of the T_t spectrum, SD is very low for shorter wavelengths due to the strong absorption between 200 and 300 nm, while for longer wavelengths it increases with the wavelength. The R_t spectrum presents a more or less constant SD in the entire spectral range.

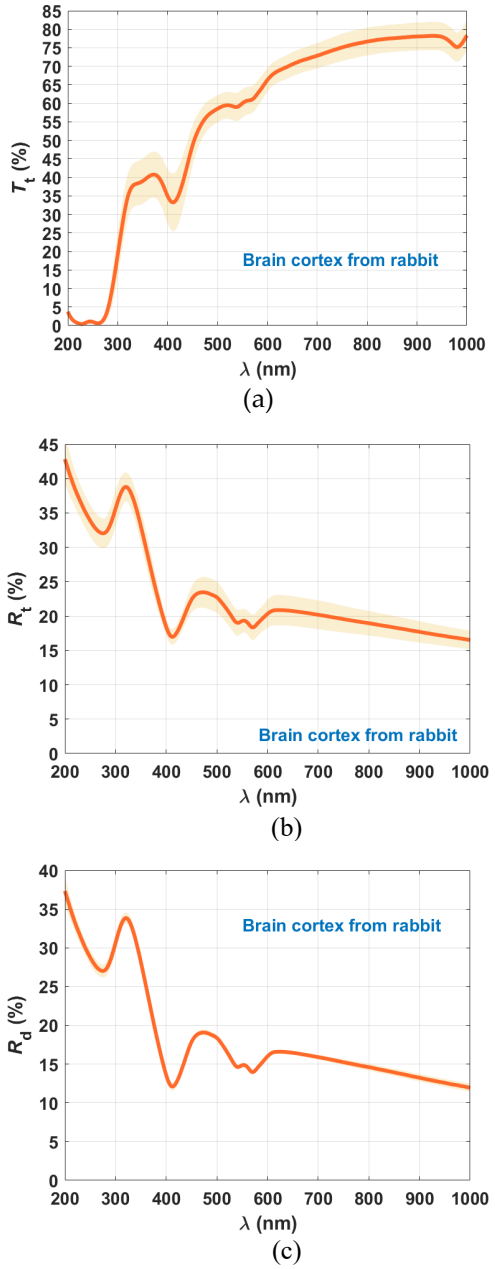


Fig. 2 Mean measured spectra and SD of the rabbit brain cortex: (a) $T_t(\lambda)$, (b) $R_t(\lambda)$, and (c) $R_d(\lambda)$.

3.2 Direct calculation of $\mu_a(\lambda)$

Using the T_t and R_t spectra two by two in Eq. (4), the 10 μ_a spectra were calculated. The mean $\mu_a(\lambda)$ and SD that resulted from these direct calculations are presented in Fig. 3.

Due to the contributions of T_t and R_t in the calculation of the $\mu_a(\lambda)$ through Eq. (4), there are several absorption bands visible in Fig. 3. The first absorption band occurs at 230 nm, showing the amino acid connections of tyrosine and tryptophan in proteins [39, 40]. The occurrence of this band is not surprising, since it is known that the brain tissues, especially the cortex contain several types of proteins, such as actin, albumin, α-tubulin, β-tubulin, neuron specific enolase (NSE), and vimentin [41]. The second absorption band seen in Fig. 3 occurs at 267 nm, showing a combination of the absorption band of DNA/RNA at 260 nm with the one of hemoglobin at 274 nm [42]. The absorption bands of oxygenated hemoglobin in the visible range are also visible at 411 nm (Soret band) and 540 and 570 nm (Q bands) [42], as well as the absorption band of water at 980 nm [42].

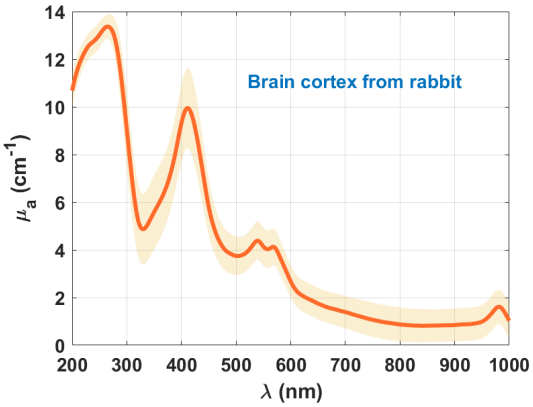


Fig. 3 Mean μ_a spectrum and SD of the rabbit brain cortex.

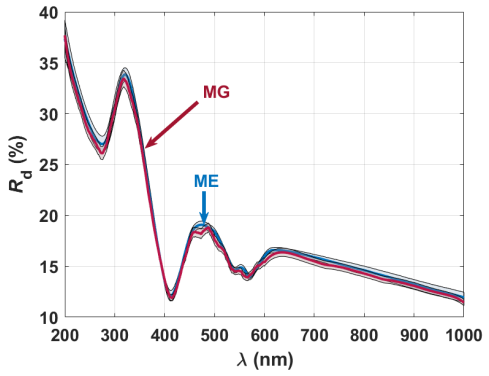
Additional information can be retrieved from the mean $\mu_a(\lambda)$ represented in Fig. 3, since such spectrum presents a decreasing baseline with increasing wavelength. Such behavior for the baseline suggests the presence of pigments in the cortex brain tissues that were used in the present study. A further analysis of this spectrum will be made in Subsection 3.4 to identify the pigments and quantify their content. First, we need to check if the ML estimations are capable of generating similar $\mu_a(\lambda)$ from the R_d spectra as the ones obtained with direct calculation from invasive measurements. Such part of the study is presented in Subsection 3.3.

3.3 Machine Learning estimation of $\mu_a(\lambda)$

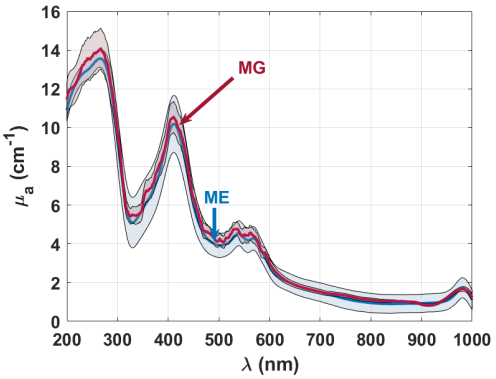
Once the $\mu_a(\lambda)$ of the brain cortex was calculated directly from the experimental spectra of T_t and R_t, we initiated the estimation of the absorption spectrum through ML algorithms. According to the description presented in Subsection 2.4, this part of the study was initiated by training and fine-tuning the GANs models to generate both new R_d and μ_a spectra to be used for the training and validation of the ML algorithms. After fine-tuning the GANs, the new generated spectra were represented along with the experimental spectra in Fig. 4 for comparison.

As we can see from graphs in Fig. 4, some low-magnitude discrepancies are seen between the ME and the MG spectra at some wavelengths. Regardless of these discrepancies, the overall wavelength-dependence and the magnitude of the generated spectra are very similar to the ones that result from direct calculations with the experimental measurements. After this initial training and tuning of the GANs, they were used to generate new groups of 10, 50 and 100 spectra. Such groups of spectra were used in the training process of the ML algorithms to

recreate $\mu_a(\lambda)$ from $R_d(\lambda)$, as described in Subsection 2.4. Such training process was made in four ways – using only the 10 experimental spectra with the LOO method, using 10 experimental and 10 generated spectra, using 10 experimental and 50 generated spectra, and using 10 experimental and 100 generated spectra. By doing these different trials, we expect to identify both the overfitting and the underfitting characteristics of the ML algorithms and also to see if the increase of the generated spectra prevents the occurrence of the overfitting. Such four tests were made with all ML algorithms.



(a)

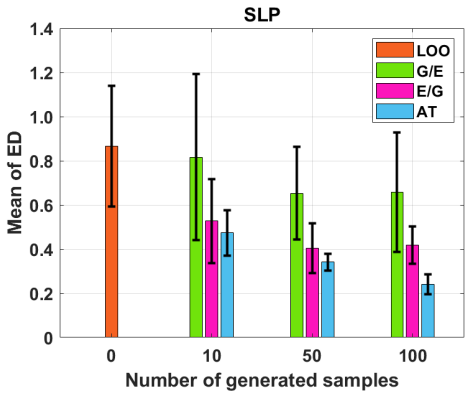


(b)

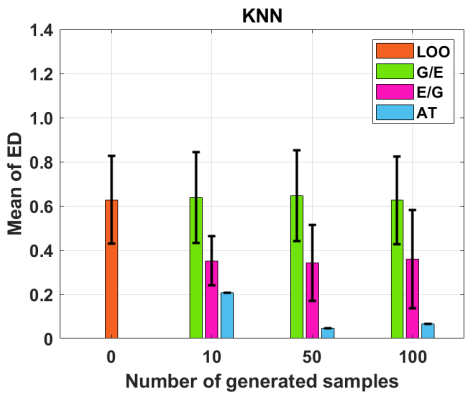
Fig. 4 Mean experimental (ME) and mean generated (MG) spectra for R_d (a) and μ_a (b) of the rabbit brain cortex.

The first ML algorithm that was used to recreate $\mu_a(\lambda)$ from the $R_d(\lambda)$ was the SLP. The second was the KNN and the third was the RFR. Following the estimation procedure described in Subsection 2.4, in all AT estimations with each algorithm, the spectra generated with the GANs were combined with the experimental spectra, having 80% of the total spectra been used in the training process and the remaining 20% been used in the validation process of the algorithm. Experimental spectra were included both in the training and in the validation process of the three AT algorithms.

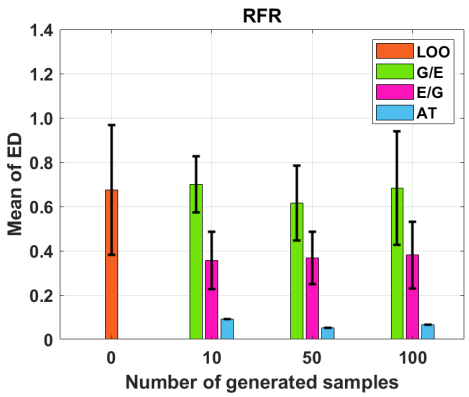
To evaluate which algorithm generated the better μ_a spectra, Eq. (5) was used to calculate the ED as a measurement of the algorithm performance. Fig. 5 presents the results of these calculations for four cases, according to the number of generated spectra used in the estimations: none, 10, 50 and 100.



(a)



(b)



(c)

Fig. 5 Calculated ED for the SLP (a), the KNN (b) and the RFR (c) models.

Analyzing the graphs in Fig. 5, we see various information. First, the ED obtained for the LOO method presents a high value for all algorithms, indicating that by using only 10 experimental spectra, the estimations are deceiving. Considering the SLP algorithm, we see that the G/E method shows similar ED for 10 generated samples to the one observed for the LOO method. By increasing to 50 generated samples, a decrease of the mean ED is observed, but no improvement is seen when

the number of generated samples increases to 100. Considering the E/G method, when 10 generated samples are used in the training process, we see a significant decrease of ED from the one obtained for the LOO method. When 50 generated samples are used, a further decrease is observed, but increasing the number of samples to 100, no improvement is observed, once again. The AT method is the one that presents a continuous decrease of ED in the SLP algorithm, but comparing with the other algorithms, the SLP is the one that presents the highest SD values.

In the case of the KNN the ED value obtained for the G/E method remains almost equal to the one obtained with the LOO method in all cases tested. This means that such method does not show any improvement in the recreation of μ_a. The E/G method presents similar variations to the ones observed with the SLP algorithm, but with a higher SD. Once again no improvement is seen when passing from 50 to 100 generated samples. The AT method is the one that presents higher decreases of ED in all cases studied with the KNN algorithm. In this study, very low mean ED and SD values are seen for the cases of 50 and 100 generated samples. Although these values are low, the mean ED for the study with 10 generated samples is still comparably high.

Finally, when using the RFR algorithm, we see variations for the mean ED that are similar to the ones obtained for the KNN algorithm. Considering the magnitude of the SD, and with the exception of the G/E estimation with 100 generated samples, we see smaller values than in the other algorithms. In the case of the G/E, once again the mean ED remains almost unchanged and similar to the value obtained for the LOO method. The ED for the E/G method decreases to about one-half of the value seen for the LOO method, but no improvement is seen when the number of generated samples is increased. In the case of the AT method, we see the best results, since in all cases tested with this algorithm, a significant decrease is observed, obtaining ED values always below 0.1.

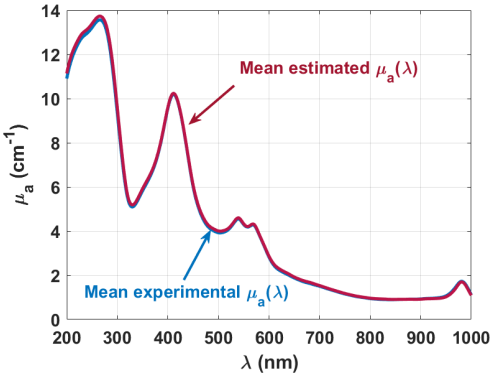


Fig. 6 Comparison between the MES and the MRS of μ_a that result from the estimation with the LOO method.

An overall evaluation of the results presented in Fig. 5 shows that the RFR algorithm is the one with the best performance. Not also it presents the highest decrease in ED for the AT method, but all estimation methods tested with this algorithm present the lowest SD. Considering these facts, we represented in the following four figures all the MES obtained with the RFR algorithms to compare with the MRS that resulted from the direct calculations, as presented in Fig. 3. Such comparison is made in Fig. 6 for the MES obtained with the LOO method, in Fig. 7 for the MES obtained with 10 generated spectra, in Fig. 8 for the MES obtained with 50 generated spectra and in Fig. 9 for the MES obtained with 100 generated spectra.

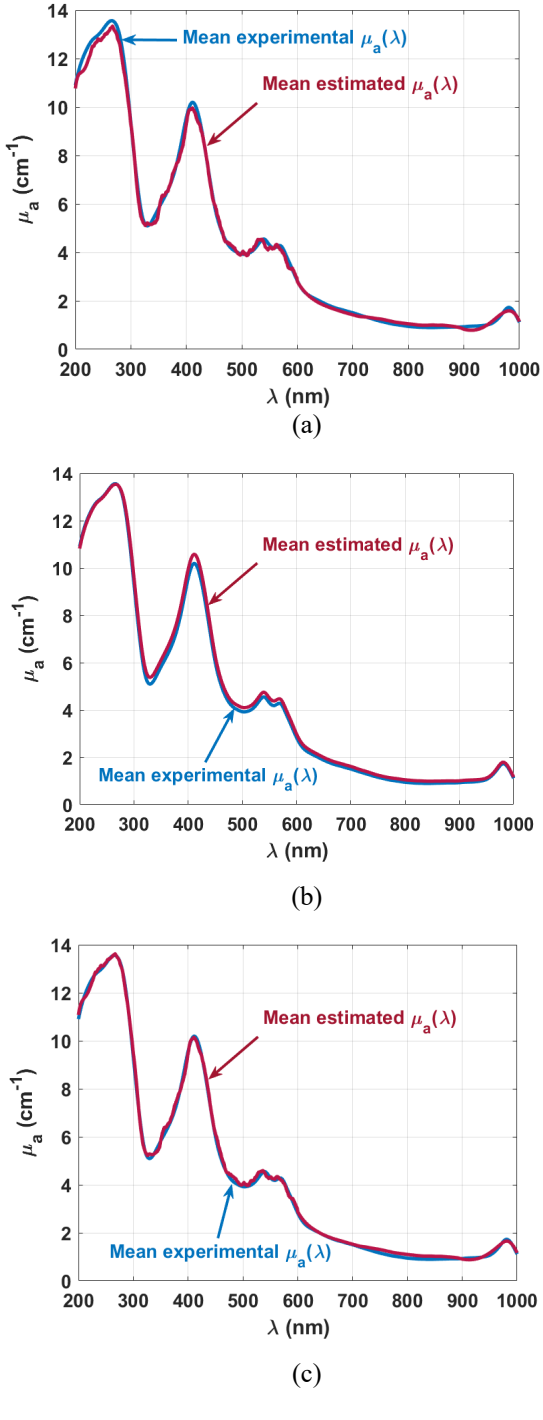
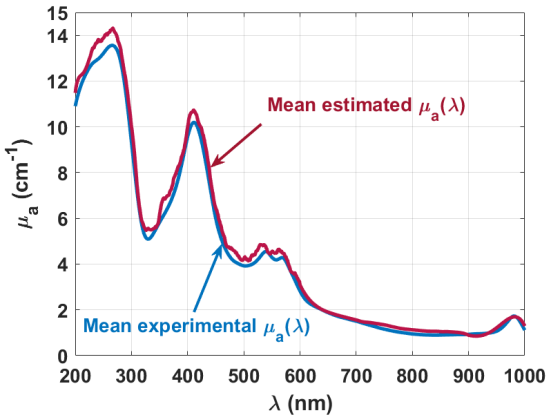
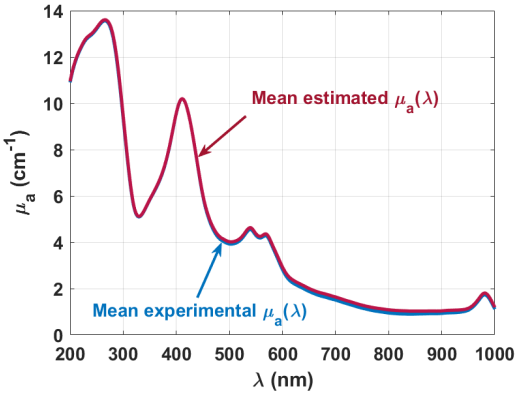


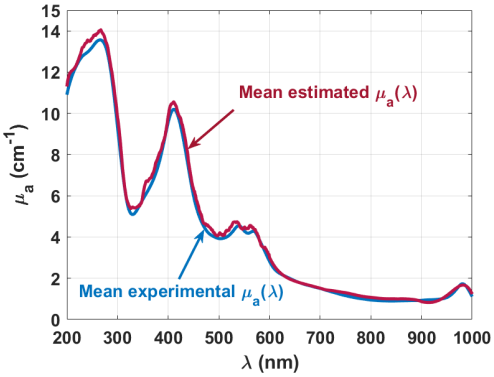
Fig. 7 Comparison between the MES and the MRS of μ_a that result from the estimations with 10 generated samples: 10–G/E (a), 10–E/G (b) and 10–AT (c).



(a)



(b)



(c)

Fig. 8 Comparison between the MES and the MRS of μ_a that result from the estimations with 50 generated samples: 50–G/E (a), 50–E/G (b) and 50–AT (c).

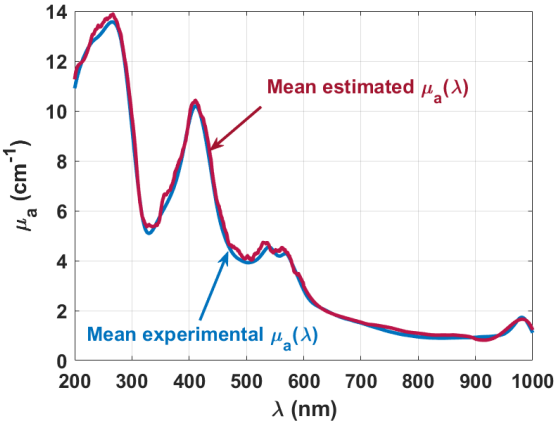
Considering the matching of the MES to the MRS in the various panels presented in the above Figs., we see that in general they are all good, presenting the same levels of μ_a at all wavelengths, similar wavelength dependencies and showing the same absorption bands. The best matching is obtained for the LOO method (Fig. 6), but such good matching is deceiving, since only a small number of experimental spectra were used both in the training and in the validation of the RFR model to obtain such mean estimation. Other good estimations that apart from the previously mentioned characteristics show good spectral smoothing are the ones obtained with the E/G method (see Figs. 7(b), 8(b) and 9(b)). Although these estimations are only second-best to the one obtained with the LOO method, once again these results are also deceiving. By using the experimental spectra in the training process and the generated spectra in the validation is not a reliable approach in the ML point-of-view. Nevertheless, the analysis of the corresponding graphs in the above Figures shows that this method also improves with the increase of the generated spectra that are used in the validation. When we analyze the mean estimations produced by the G/E method (see Figs. 7(a), 8(a) and 9(a)), we see that the mean estimations lose the smoothing characteristic. Regardless of the lack of spectral smoothing, these estimations also show good agreement with the MRS in terms of wavelength dependence, μ_a levels and absorption bands. Comparing between the three estimations with the G/E method, we see that the worst case occurs for the estimation with 50 generated spectra. Such result shows that if a large number of experimental spectra were available in the GANs generation process, a better performance could be obtained with this method. Finally, the MES obtained with the AT method also shows lack of spectral smoothing (see Figs. 7(c), 8(c) and 9(c)), but the μ_a spectra obtained with this method are more approximated to the MRS, as indicated by the lowest ED values in the graph in Fig. 5(c). Once again, the results obtained with the AT method show that more experimental spectra are necessary to improve both the generation of new spectra with the GANs models and the estimation of the $\mu_a(\lambda)$ from the measured $R_d(\lambda)$.

The data in the graphs of Figs. 6, 7, 8 and 9 show the necessity of increasing the number of samples to use in the training and validation of the ML algorithms to improve the quality of the estimations. Such increase in the number of experimental spectra would also improve the efficiency of the GANs to generate new spectra. By doing that, the various estimations presented in the previous Figures could have higher spectral smoothness, which is the most evident flaw in the estimations made with the G/E and AT methods. Nevertheless, if we disregard the lack of smoothness in the estimated spectra, we see from the previous Figures that all cases studied present acceptable results. We will now present the final stage of this research – the evaluation of pigment content in the brain cortex.

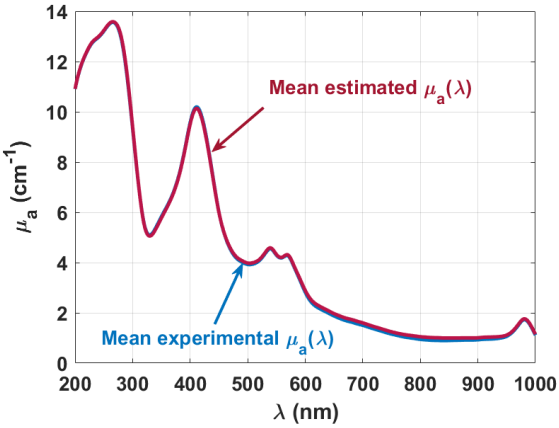
3.4 Pigment content evaluation from the calculated and estimated $\mu_a(\lambda)$

After performing an evaluation on the quality of the $\mu_a(\lambda)$ that were estimated with the various methods within the RFR algorithm, we will now consider the ones that presented the best performance for the further calculations to obtain the pigment content in the brain cortex. At this last stage of the research it will be interesting to check if the estimated μ_a spectra have similar contents of melanin and lipofuscin, and if by retrieving the absorption of those pigments we can find similar absorption ratios for DNA/RNA and hemoglobin as the ones previously obtained for the $\mu_a(\lambda)$ that was

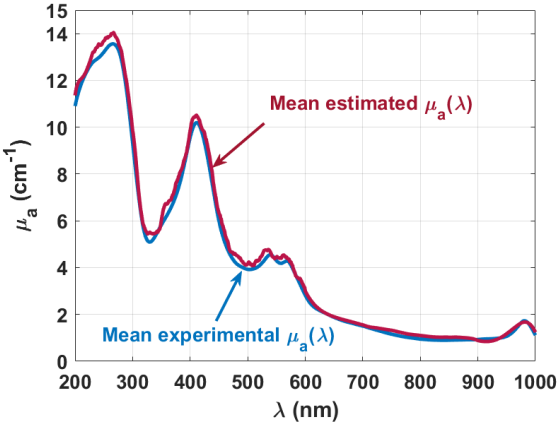
obtained from direct calculation [13]. Although the tissue samples used to acquire the spectral measurements for the direct calculation and for the ML estimations of $\mu_a(\lambda)$ were collected from different animals, those animals were obtained from the same source and were all adults with approximately the same age.



(a)



(b)



(c)

Fig. 9 Comparison between the MES and the MRS of μ_a that result from the estimations with 100 generated samples: 100–G/E (a), 100–E/G (b) and 100–AT (c).

In the same way as we did with the $\mu_a(\lambda)$ obtained with direct calculations [13], we started by reconstructing the absorption spectra of melanin and lipofuscin from graphical data published in literature [37, 38]. These spectra are presented in Fig. 10.

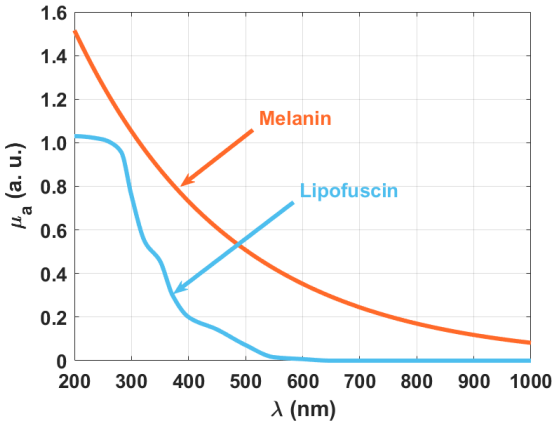


Fig. 10 The absorption spectra (μ_a) for melanin and lipofuscin.

The absorption spectrum of melanin presented in Fig. 10 was reconstructed from graphical data presented in Ref. [37] and it correspond to eumelanin, the most common type of the melanin pigments, and the one that can be observed in the skin. The authors of Ref. [37] constructed such graph based on diffuse reflectance measurements made from human skin *in vivo*, but in that paper it is also indicated that such data does not differ much from the one collected from *ex vivo* samples. In the case of the melanin found in brain tissues, which is commonly designated as neuromelanin, it is a mixture of eumelanin and pheomelanin [43]. With the objective of reconstructing the absorption spectrum of neuromelanin with the highest precision, we searched for the absorption spectrum of pheomelanin to see if it differs from the one of eumelanin that is reported in Ref. [37]. A discussion of the extinction coefficient both of eumelanin and pheomelanin is available on the website of the Oregon Medical Laser Center [44], where both types of melanin present a very similar extinction spectrum between 200 and 900 nm. Since these spectra are very similar, by considering in our study the spectrum of eumelanin, as represented in Fig. 10, we can consider that it is a good approximation to the mixture of eumelanin and pheomelanin that composes the neuromelanin in the brain tissues.

Since the absorption spectra presented in Fig. 10 were reconstructed from published graphical data, no mathematical equation is available to describe them. This means that to combine these spectra with the objective of subtracting such combination from the $\mu_a(\lambda)$ of the brain cortex, numerical data for each of the curves in Fig. 10 needs to be considered. In the case of the $\mu_a(\lambda)$ that was obtained through direct calculations [13], and after some trials to combine the two spectra in Fig. 10 to characterize the pigment content in the cortex, we found that such content is characterized by the following combination:

$$\mu_{a-pigment}(\lambda) = 3.5 \times M(\lambda) + 1.9 \times L(\lambda), \quad (6)$$

with $M(\lambda)$ and $L(\lambda)$ representing the wavelength dependencies of the absorption coefficient of melanin and lipofuscin, respectively, as represented in Fig. 10.

As referred in Ref. [13], Eq. (6) provides a good description of the decreasing baseline that is seen in Fig. 3, but such baseline may not be only due to the presence of these pigments in the cortex. The precursors of these pigments or other pigments may also be included in the cortex and contribute to the absorption baseline. An example is hemosiderin, which has an absorption spectrum similar to the one of melanin [45]. Since the cortex tissues used in the present study presented no evidence of rapid hemoglobin destruction or fast and excessive iron deposition, we neglected the absorption of hemosiderin in the calculation of $\mu_{a\text{-pigment}}(\lambda)$ with Eq. (6). Considering carotenoid-type pigments, such as lutein, β-cryptoxanthin, and zeaxanthin, all have a similar absorption spectrum, with null absorption for wavelengths above ~500 nm and low absorption in the UV range. Between 400 and 500 nm, these carotenoid-type pigments have three absorption peaks, being the higher magnitude of these peaks observed for β-cryptoxanthin [46]. Due to the fact that these absorption bands occur between 420 and 476 nm [46], they seem to have no influence in the resulting $\mu_a(\lambda)$ of the cortex. As seen in Fig. 3 for this wavelength range, the mean μ_a spectrum of the cortex only shows a well-defined Soret band, with center wavelength at 411 nm.

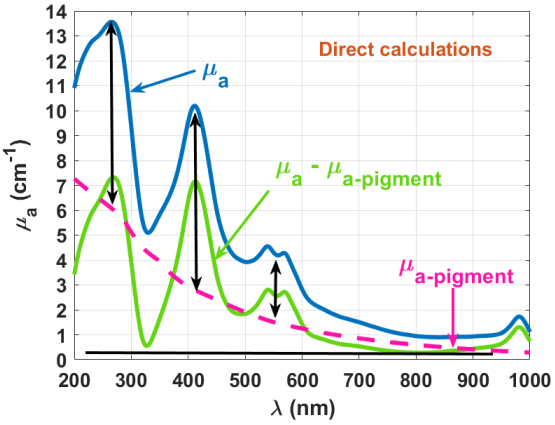
Considering the melanin precursors, they show an absorption spectrum mainly characterized by UV-bands, with null values above 300 nm. *L*-cysteine, has an absorption spectrum which consists on the combination of two overlapping bands, the one with higher magnitude centered near 230 nm and the other centered near 280 nm [47]. This means that *L*-cysteine might also be present in the brain cortex tissues and that its absorption may contribute to the absorption band that we see at 230 nm in Fig. 3. The absorption spectrum presented in Fig. 3 shows no evidence of the 280 nm band, but the strong band at 267 nm that results from the combination of the DNA/RNA band at 260 nm and the hemoglobin band at 274 nm, might be masking the 280 nm band. Considering *L*-tyrosine, its absorption spectrum is the combination of two bands with a small overlapping, with the higher-magnitude band being centered at a wavelength smaller than 240 nm and the other centered near to 285 nm [48]. Considering dopamine, its absorption spectrum contains only a single band, with a central peak near 280 nm [49]. As in the case of *L*-cysteine, and for the same reasons presented above, the absorption bands of *L*-tyrosine and dopamine may be masked by the strong absorption bands of the amino acid connections in proteins and the one that results from the combination of DNA/RNA and hemoglobin. Such fact suggests that melanin precursors may also be present in the cortex samples used in the present study.

Considering now the lipofuscin precursors, we found only the absorption spectrum for mitochondria, which is also limited to the UV range. Such spectrum contains a single band between 300 and 400 nm, with the peak near 360 nm [50]. Considering the absorption spectrum that we calculated for the brain cortex (Fig. 3), the absorption band of mitochondria may be masked by the Soret band, which extends to a lower wavelength close to 320 nm.

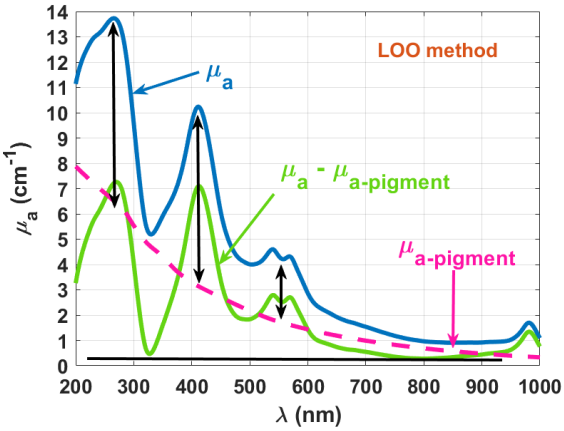
Considering the above discussion about the absorption spectra of pigments and their precursors, and assuming that only melanin and lipofuscin contribute to the decaying baseline presented in Fig. 3 for the brain cortex, we will now present a comparative evaluation of the pigment contents in the various $\mu_a(\lambda)$ that were estimated by the different RFR methods used in the present study. The first step of this final comparative study consisted on subtracting the combination of melanin and lipofuscin absorption, as described by Eq. (6), from the mean μ_a spectrum presented in Fig. 3. The corrected $\mu_a(\lambda)$ obtained with this calculation is considered as a reference for the similar calculations to be made with the different μ_a spectra that were generated with the best performance methods with the RFR model. Such methods are the AT with 10, 50 and 100 digitally generated spectra, as presented in Fig. 5. We also considered the spectrum generated with the LOO method to evaluate its capability with a low number of experimental spectra to reproduce the pigment content and evaluate the DNA and hemoglobin ratios. In these calculations, the combination of pigments to subtract to each mean μ_a spectrum was recalculated as in Eq. 6, but using different numbers as multiplication factors to $M(\lambda)$ and $L(\lambda)$, so that the corrected $\mu_a(\lambda)$ could have similar baseline values to the ones that were obtained from the corrected $\mu_a(\lambda)$ that results from direct calculations. The results from these calculations are presented in Fig. 11 for the cases of direct calculations from experimental measurements and the LOO method.

Comparing between the two graphs of Fig. 11, it is seen that the μ_a spectra that result from direct calculations and from the LOO method (blue curves) are very similar. The corresponding μ_a spectra that were obtained using the AT method with 10, 50, and 100 digitally generated spectra are also similar to these, but some small differences exist. As an example, comparing between the two graphs of Fig. 11, it is seen that the absorption peaks at 267 and 411 nm are a little higher in the case of the LOO method than in the case of direct calculations.

The double-arrow lines presented in both graphs of Fig. 11 refer to the calculated ratios at the main absorption bands, with center wavelengths at 267 nm, 411 nm and 550 nm. Before subtracting the pigments, those ratios were calculated as the value of μ_a in the blue curve divided by the value of μ_a of the pigment in the pink curve. After subtracting the pigment absorption (pink curve) to the μ_a of the brain cortex (blue curve), the corrected μ_a spectrum of the brain cortex (green curve) was obtained in all cases studied. Considering such corrected spectra, the new ratios were calculated as the value of μ_a at the above wavelengths in the green curve divided by the minimum value in that same curve, which occurs at 801 nm and is represented by the black horizontal line in both graphs of Fig. 11.



(a)



(b)

Fig. 11 Wavelength dependencies of μ_a for the combination of melanin and lipofuscin and for the rabbit brain cortex, before and after subtracting the absorption of the pigments that resulted from direct calculations (a), and RFR-LOO estimation (b).

To summarize the calculations performed to obtain the pigment contents and the results presented in Fig. 11, Table 1 contains the melanin and lipofuscin combinations used in each case.

Table 1 Pigment combinations used in the various methods to obtain the corrected $\mu_a(\lambda)$ of the brain cortex.

Method	Pigment content
Direct calculation	3.50×M+1.90×L
RFR – LOO	4.04×M+1.70×L
RFR – 10AT	4.84×M+0.40×L
RFR – 50AT	4.68×M+1.00×L
RFR – 100AT	4.85×M+0.60×L

Considering the multiplication factors for M and L in Table 1, we see that all methods studied show a higher content of melanin than the one of lipofuscin in the brain cortex. Although the ML models used in the present study showed some drawbacks, they were all able to reach the same result that differentiates the melanin and lipofuscin contents in the brain cortex. Comparing between methods, the multiplication factors in Table 1 show that both the LOO and the AT methods originate a higher content of melanin and a lower lipofuscin content than the ones obtained through the direct calculation method.

To evaluate the DNA and hemoglobin contents in the brain cortex, the absorption ratios at the main absorption bands were calculated for all methods, before and after subtracting the pigments absorption from the μ_a spectra. Table 2 presents those results at the wavelengths 267 nm, 411 nm and 550 nm for comparison.

Table 2 Absorption ratios for the main absorption bands of DNA and hemoglobin for the various methods used to obtain $\mu_a(\lambda)$ of the brain cortex.

	Absorption ratios at central wavelengths					
	267 nm		411 nm		555 nm	
Method	before	after	before	after	before	after
Direct calculation	2.19	26.42	3.55	25.80	2.73	9.26
RFR – LOO	2.12	26.23	3.25	25.64	2.50	9.10
RFR – 10AT	2.22	27.11	2.92	24.18	2.11	8.07
RFR – 50AT	2.15	27.12	3.04	25.61	2.25	8.81
RFR – 100AT	2.21	27.92	2.99	25.39	2.17	8.62

Considering the data presented in Table 2, we see that the LOO method produces very close ratios to the ones obtained with the direct calculation method for the considered absorption bands. In order to reach these values, a higher melanin content and a lower lipofuscin content needed to be considered to reproduce the corrected $\mu_a(\lambda)$ that results from the ML-LOO method. By reaching these results with a limited number of experimental spectra, the LOO method can be considered a good option to recreated the μ_a spectrum, but with limited statistics, as explained in our previous study [2].

When introducing artificially generated spectra with the objective of obtaining higher performance for the RFR algorithm, we see that by increasing the number of digital spectra from 10 to 50 and then to 100, all studies show absorption ratios in the same order of magnitude of the ones obtained in the direct calculation procedure. As the number of digital spectra increases from 10 to 50, we see that the absorption ratios become more approximated to the ones obtained through the direct calculation approach, but when considering 100 digital spectra, such approximation becomes worse. Such variation indicates that the GANs models used to generate digital spectra work to a certain point, and if the number of generated spectra increases above some limiting value, the generated spectra present features that differ from the real tissue under study. This occurs due to the fact that the GANs models learn the normal distribution of the experimental spectra. Consequently, when the number of artificially generated spectra is increased above a certain limit, the GANs models are more likely to generate low-quality spectra that are located at the extremes of the

normal distribution. Considering the GANs models used in this study to generate both the R_d and μ_a spectra, the generated data seems to maintain the spectral quality up to a number of 50 digitally generated spectra. Such spectral quality is not maintained for a higher number of artificially generated spectra, as we observed in some trials that were performed. In future applications we plan to use different GANs models to generate spectra artificially and fine-tuning will be performed to obtain a significant number of artificial data.

4 Conclusions

The present study shows the possibility of using ML estimations to reconstruct the $\mu_a(\lambda)$ of a tissue from noninvasive or minimally invasive spectral measurements, but to obtain high accuracy in the estimated spectra, a large number of experimental spectra is necessary. When a large number of measured spectra is not available, which is the most common case in spectral biophotonics, and if the LOO approach is acceptable for a particular study, it can be used to recreate $\mu_a(\lambda)$ and obtain diagnostic information with good accuracy. In cases when the LOO method is not an option, and the artificial generation of spectra is a possibility, the RFR or other algorithms can be used to recreate $\mu_a(\lambda)$. In that case, the digital generation of spectra can be made using GANs, but this study shows that a small number of experimental spectra will not be sufficient to generate a large number of artificial spectra with good quality. To obtain such high numbers of good artificial spectra, a considerable number of experimental measurements must be provided.

To evaluate the precision of the algorithms and models used in our study, the mean ED between the MES and MRS was calculated. Since the LOO method uses only experimental spectra, we considered its mean ED as a reference in the evaluation of the other methods accuracy. As reported in the graphs of Fig. 5, the LOO method had a mean ED of 0.628.

Considering the different methods used with the SLP algorithm, and retrieving data from Fig. 5(a), for the studies, where 10, 50 and 100 digitally generated spectra were used, the mean ED values obtained were: 0.817, 0.652 and 0.658 with the G/E method; 0.527, 0.404, and 0.418 with the E/G method; and 0.474, 0.341, and 0.241 with the AT method.

In the studies performed with the KNN algorithm, the mean ED values obtained with 10, 50 and 100 digitally generated spectra were: 0.638, 0.647, and 0.625 with the G/E method; 0.352, 0.343, and 0.360 with the E/G method; and 0.206, 0.048, and 0.067 with the AT method.

The last algorithm used in our study was the RFR. For the studies with this algorithm with 10, 50, and 100 digitally generated spectra, the mean ED values obtained were: 0.701, 0.616, and 0.684 with the G/E method; 0.357, 0.367, and 0.381 with the E/G method; and 0.092, 0.052, and 0.066 with the AT method.

Analyzing all these accuracy values, we see that the G/E method provides the worst results, always above the one obtained with the LOO method. Both the E/G and the AT methods provide better results than the LOO method in all algorithms, but considering all the studies performed, the AT method is the best. Considering this method, the mean ED values obtained both with the KNN and with the RFR algorithms can be considered the best of the whole study.

After evaluating the limitations on the application of ML methods in spectral biophotonics to estimate tissue absorption, we intend to perform other studies in the future with a biological tissue where a large number of measurements is possible. We expect that by performing such studies and obtaining a significant number of R_d and μ_a spectra for a particular tissue, we can use GANs models to generate a high number of artificial spectra that will be added to the experimental data as input to the ML algorithms to recreate $\mu_a(\lambda)$ and obtain precise diagnostic information. We also plan to test different algorithms in the GANs models to check if they bring better accuracy in the generated spectra than the ones used in the present study. After performing such tests and if diseased brain tissues become available for study, we plan to perform similar studies with those tissues to retrieve the pigments, DNA and hemoglobin contents. By comparing those contents between healthy and diseased brain tissues, we can provide precise diagnostic information or even establish a relation between those contents and the progression of the disease for early detection procedures to be developed.

Disclosures

All authors declare that there is no conflict of interests in this paper.

Acknowledgements

The authors of the article knew well and communicated with Alexey Bahskatov for many years, especially Valery V. Tuchin and Luís M. Oliveira. We had many joint research discussions, co-authorship in various publications and cooperation in the past. Plans for the future had already been pointed-out, but due to Alexey's sudden departure, such plans were mercilessly interrupted. We have lost a great scientist and a person with a huge soul, sociable, but at the same time modest and kind. We will always remember our warm meetings and fruitful work with Alexey.

This research was supported by the Portuguese grant FCT-UIDB/04730/2020.

I.S.M. was supported by the Portuguese grant FCT-UIBD/151528/2021.

The work of V.V.T. was supported by the Government of the Russian Federation, Project No. 075-15-2021-615.

References

1. S. Carvalho, I. Carneiro, R. Henrique, V. Tuchin, and L. Oliveira, "Lipofuscin-type pigment as a marker of colorectal cancer," Electronics 9(11), 1805 (2020).
2. L. Fernandes, S. Carvalho, I. Carneiro, R. Henrique, V. V. Tuchin, H. P. Oliveira, and L. M. Oliveira, "Diffuse reflectance and machine learning to differentiate colorectal cancer," Chaos 31, 053118 (2021).
3. L. M. Oliveira. K. I. Zaytsev, and V. V. Tuchin, "Improved biomedical imaging over a wide spectral range from UV есло THz towards multimodality," SPIE Proceedings 11585, 1158503 (2020).
4. D. K. Tuchina, A. N. Bashkatov, A. B. Bucharskaya, E. A. Genina, and V. V. Tuchin, "Study of glycerol diffusion in skin and myocardium ex vivo under the conditions of developing alloxan-diabetes," Journal of Biomedical Photonics & Engineering 3(2), 020302 (2017).
5. D. K. Tuchina, R. Shi, A. N. Bashkatov, A. A. Genina, D. Zhu, Q. Luo, and V. V. Tuchin, "Ex vivo optical measurements of glucose diffusion kinetics in native and diabetic mouse skin," Journal of Biophotonics 8(4), 332–346 (2015).
6. K. Wakamatsu, T. Murase, F. A. Zucca, and S. Ito, "Biosynthetic pathway to neuromelanin and its aging process," Pigment Cell & Melanoma Research 25(6), 792–803 (2012).
7. J. K. Reddy, N. D. Lalwani, M. K. Reddy, and S. A. Qureshi, "Excessive accumulation of autofluorescence lipofuscin in the liver during hepatocarcinogenesis by methyl clofenapate and other hypolipidemic peroxisome proliferators," Cancer Research 42(1), 259–266 (1982).
8. Y. Kakimoto, C. Okada, N. Kawabe, A. Sasaki, H. Tsukamoto, R. Nagao, and M. Osawa, "Myocardial lipofuscin accumulation in ageing and sudden cardiac death," Scientific Reports 9(1), 3304 (2019).
9. G. Zonios, L. T. Perelman, V. Backman, R. Manoharan, M. Fitzmaurice, J. Van Dam, and M. S. Feld, "Diffuse reflectance spectroscopy of human adenomatous colon polyps in vivo," Applied Optics 38(31), 6628–6637 (1999).
10. N. Gomes, V. V. Tuchin, and L. M. Oliveira, "Refractive index matching efficiency in colorectal mucosa treated with glycerol," IEEE Journal of Selected Topics in Quantum Electronics 27(4), 7200808 (2021).
11. N. Gomes, V. V. Tuchin, and L. Oliveira, "UV-NIR efficiency of the refractive index matching mechanism on colorectal muscle during treatment with different glycerol osmolarities," Journal of Biomedical Photonics & Engineering 6(2), 020307 (2020).
12. I. Carneiro, S. Carvalho, R. Henrique, L. Oliveira and V. V. Tuchin, "Measurement of optical properties of normal and pathological human liver tissues from deep-UV to NIR," SPIE Proceedings 11363, 11363G (2020).
13. T. M. Gonçalves, I. S. Martins, H. F. Silva, V. V. Tuchin, and L. M. Oliveira, "Spectral optical properties of rabbit brain cortex between 200 and 1000 nm," Photochem 1(2), 190–208 (2021).
14. I. S. Martins, Caracterização das Propriedades Óticas do Pâncreas e Estudo da Difusão da Glicerina no seu Interior, MsC thesis, Polytechnic Institute of Porto – School of Engineering, Porto, Portugal, June 30 (2021).
15. A. R. Botelho, Determinação das propriedades Óticas de Tecidos e Caracterização de Tratamentos de Transparência em Rim Humano Normal e Patológico, MsC thesis, Polytechnic Institute of Porto – School of Engineering, Porto, Portugal, November 15 (2021).
16. V. V. Tuchin, Tissue Optics – Light Scattering Methods and Instruments for Medical Diagnosis, 3rd ed., SPIE Press, Bellingham (WA), USA (2015).
17. L. Wang, S. L. Jacques, and L. Q. Zheng, "MCML-Monte Carlo modeling of light transport in multi-layered tissues," Computer Methods and Programs in Biomedicine 47(2), 131–146 (1995).
18. S. A. Prahl, M. J. C. van Gemert, and A. J. Welch, "Determining the optical properties of turbid media by using the adding-doubling method," Applied Optics 32(4), 559–568 (1993).
19. L. M. C. Oliveira, V. V. Tuchin, The Optical Clearing Method: A New Tool for Clinical Practice and Biomedical Engineering, Springer, Cham, Switzerland (2019). ISBN: 978-3-030-33055-2.
20. V. Backman, A. Wax, and H. Zhang, A Laboratory Manual in Biophotonics, CRC Press, Boca Raton, USA (2018).
21. P. Pradhan, S. Guo, O. Ryabchykov, J. Popp, and T. W. Blocklitz, "Deep learning a boom for biophotonics?" Journal of Biophotonics 13(6), e201960186 (2020).
22. A. Creswell, T. White, V. Dumoulin, K. Arulkumaran, B. Sengupta, and A. A. Bharath, "Generative Adversarial Networks: An overview," IEEE Signal Processing Magazine 35, 53 (2018).
23. I. Goodfellow, J. Pouget-Abadie, M. Mirza, B. Xu, D. Warde-Farley, S. Ozair, A. Courville, and Y. Bengio, "Generative adversarial networks," arXiv:1406.2661v1 (2014).
24. L. Lan, L. You, Z. Zhang, Z. Fan, W. Zhao, N. Zeng, Y. Chen, and X. Zhou, "Generative adversarial networks and its applications in biomedical informatics," Frontiers in Public Health 8, 164 (2020).
25. GBD 2016 Neurology Collaborators, "Global, regional, and national burden of neurological disorders, 1990-2016: A systemic analysis for the global burden of disease study 2016," The Lancet Neurology 18(5), 459–480 (2019).
26. M. P. Mattson, W. Duan, W. A. Pedersen, and C. Culmsee, "Neurodegenerative disorders and ischemic brain diseases," Apoptosis 6, 69–81 (2001).
27. K. L. Double, V. N. Dedov, H. Fedorov, E. Kettle, G. M. Halliday, B. Garner, and U. T. Brunk, "The comparative biology of neuromelanin and lipofuscin in the brain," Cellular and Molecular Life Sciences 65, 1669–1682 (2008).

28. A. Moreno-García, A. Kun, M. Calero, and O. Calero, "The neuromelanin paradox and its role in oxidative stress and neurodegeneration," Antioxidants 10(1), 124 (2021).
29. V. V. Tuchin, Optical Clearing of Tissues and Blood, SPIE Press, Bellingham (WA), USA (2006).
30. A. Y. Sdobnov, M. Darvin, E. A. Genina, A. N. Bashkatov, J. Lademan, and V. V. Tuchin, "Recent progress in tissue optical clearing for spectroscopic application," Spectrochimica Acta Part A: Molecular and Biomolecular Spectroscopy 197, 216–229 (2018).
31. T. Stewart, "Down the Rabbit Hole: Rabbit Brain vs Human Brain" (Accessed March 2022) [https://prezi.com/nmxefcgdiqq5/rabbit-brain-vs-human-brain/].
32. J. Johansson, "Spectroscopic method for determination of the absorption coefficient in brain tissue," Journal of Biomedical Optics 15(5), 057005 (2010).
33. E. P. Gilissen, L. Staneva-Dobrovski, "Distinct types of lipofuscin pigment in the hippocampus and cerebellum of aged cheirogaleid primates," The Anatomical Record 296(12), 1895–1906 (2013).
34. H. Heinsen, "Lipofuscin in the cerebellar cortex of albino rats: An electron microscopic study," Anatomy and Embryology 115, 333-345 (1979).
35. G. O. Ivy, S. Kanai, M. Ohta, G. Smith, Y. Sato, M. Kobayashi, and K. Kitani, "Lipofuscin-like substances accumulate rapidly in brain, retina and internal organs with cysteine protease inhibition," Advances in Experimental Medicine and Biology 266, 31–45 (1989).
36. J. D. Johansson, K. Wårdell, "Intracerebral quantitative chromophore estimation from reflectance spectra captured during deep brain stimulation implantation," Journal of Biophotonics 6, 435–445 (2013).
37. G. Zonios, A. Dimou, I. Bassukas, D. Galaris, A. Tsolakidis, and E. Kaxiras, "Melanin absorbance spectroscopy: new method for noninvasive skin investigation and melanoma detection," Journal of Biomedical Optics 13, 0140017 (2008).
38. M. B. Różanowska, A. Pawlak, and B. Różanowski, "Products of docosahexaenoate oxidation as contributors to photosensitizing properties of retinal lipofuscin," International Journal of Molecular Sciences 22(7), 3525 (2021).
39. G. D. Fasman, "Ultraviolet spectra of derivatives of cysteine, cysteine, histidine, phenylalanine, tyrosine, and tryptophan," Chapter 17 in Handbook of Biochemistry and Molecular Biology, G. D. Fasman (Ed.), 3rd ed., Volume 1, CRC Press, Boca Raton (FL), 192-199 (2018).
40. D. B. Wetlaufer, "Ultraviolet spectra of proteins and amino acids," Chapter 6 in Advances in Protein Chemistry, C. B. Afinsen Jr. (Ed.), Vol. 17, Academic Press, London, 303_390 (1963).
41. R. K. Narayan, W. E. Heydon, G. J. Creed, and D. M. Jacowitz, "Identification of major proteins in human cerebral cortex and brain tumors," Journal of Protein Chemistry 4(6), 375–389 (1985).
42. Y. Zhou, J. Yao, and L. V. Wang, "Tutorial on photoacoustic tomography," Journal of Biomedical Optics 21(6), 061007 (2016).
43. I.-E. Pralea, R.-C. Moldovan, A.-M. Petrache, M. Ilies, S.-C. Heghes, I. Ielciu, R. Nicoară, M. Moldovan, M. Ene, M. Radu, A. Uifălean, and C.-A. Iuga, "From extraction to advanced analytical methods: The challenges of melanin analysis," International Journal of Molecular Sciences 20(16), 3943 (2019).
44. S. L. Jacques, "Extinction Coefficient of Melanin," (Accessed March 2022) [https://omlc.org/spectra/melanin/extcoeff.html].
45. L. Zhang, X. Zou, B. Zhang, L. Cui, J. Zhang, Y. Mao, L. Chen, and M. Li, "Label-free imaging of hemoglobin degradation and hemosiderin formation in brain tissues with femtosecond pump-probe microscopy," Theranostics 8(15), 4129–4140 (2018).
46. K. Zaghdoudi, O. Ngomo, R. Vanderesse, P. Anoux, B. Myszakhmetov, C. Frochot, and Y. Guiavarch, "Extraction, identification and photo-physical characterization of persimmon (Diospyros kaki L.) carotenoids," Foods 6(1), 4 (2017).
47. A. S. Raja, J. Sathiyabama, R. Venkatesan, and V. Prathipa, "Corrosion control of carbon steel by eco-friendly inhibitor L-Cysteine-Zn2+ system in aqueous medium," Journal of Chemical, Biological and Physical Sciences 4(4), 3182–3189 (2014).
48. C. Hazra, T. Samantha, and V.A. Mahalingham, "A resonance energy transfer approach for the selective detection of aromatic amino acids," Journal of Materials Chemistry C 2(47), 10157–10163 (2014).
49. J. H. Lin, C.-J. Yu, Y.-C. Yang, and W.-L. Tseng, "Formation of fluorescence polydopamine dots from hydroxyl radical-induced degradation of polydopamine nanoparticles," Physical Chemistry Chemical Physics 17(23), 15124–15130 (2015).
50. S. Feng, T. Harayama, S. Montessuit, F. P. A. David, N. Winssinger, J.-C. Martinou, and H. Riezman, "Mitochondria-specific photoactivation to monitor local sphingosine metabolism and function," Elife 7, e34555 (2018).

Theoretical and Experimental Study of the Water-Based Drug Delivery under the Nail Plate by Er-Laser Radiation

Andrey V. Belikov, Anastasia D. Kozlova*, and Sergey N. Smirnov
ITMO University, 49 Kronverksky pr., Saint Petersburg 197101, Russia

*** e-mail:** ntavalin@gmail.com

Abstract. Double-stage active laser drug delivery (DSLADD) of an aqueous solution of methylene blue using Er:YLF laser radiation experimentally was investigated. Model for describe of the delivery of local drugs under a microporated nail plate taking into account the peculiarities of laser radiation exposure, capillary effects in microholes and diffusion in the nail plate was developed. The phenomenon of spreading of the drug consisting in the fact that after laser action drug is distributed in the nail bed not only in the area of the nail bed located directly under the microhole, but also along the border of the nail plate and the nail bed around the microhole was observed for the first time. Calculations performed within the framework of the developed model showed that, taking into account spreading phenomenon, the density of filling the nail area with microholes can be significantly reduced, which can proportionally increase the productivity of laser delivery in general. © 2022 Journal of Biomedical Photonics & Engineering.

Keywords: dual-stage method for active laser drug delivery; drug delivery model; laser microporation; nail; nail permeability coefficient.

Paper #3471 received 05 Dec 2021; revised manuscript received 07 Mar 2022; accepted for publication 08 Mar 2022; published online 31 Mar 2022. doi: 10.18287/JBPE22.08.010305.

1 Introduction

Diseases of the nails, especially fungal infections, are difficult to treat [1]. Peroral drug delivery remains the most popular delivery method due to its ease of implementation, but this delivery method can negatively affect the gastrointestinal tract and liver before the drug enters the systemic circulation. Local drug delivery largely avoids these problems, but has very low efficacy, primarily due to the extremely low permeability of drugs through the nail plate. In addition, drugs for local delivery, as a rule, quickly lose their molecular-diffusible form after application due to the rapid evaporation of the solvent, which prevents them from effectively penetrating the nail [2].

High density and hardness of the nail plate provides excellent protection for sensitive fingertips. Unfortunately, these properties make local drug delivery extremely difficult. The penetration of the drug into the nail plate occurs due to passive diffusion and is limited by the strong cross-link's characteristic of the plate structure. On the other hand, the physicochemical properties of drugs also determine the speed and depth of their penetration into the nail. The permeability of the nail plate is mainly influenced by the active molecular weight of the drug [3]. Currently, in the local treatment of fungal diseases of the nail, antifungal agents of the 2nd generation (imidazoles) and antimycotics of the 3rd generation (triazoles and allylamines) [4, 5], methylene blue (MB) [6] and chlorin-containing photodynamic drugs [7] are used.

To increase the permeability and efficiency of delivery of local drugs, chemical (acids, alcohols, glycols, etc.), physical (microporation, ionophoresis, sonophoresis, electroporation, ultrasonic and laser drug delivery) and mechanical methods (injection, removal, grinding or mechanical perforation biological tissue) can be used [8–11]. Effective laser microporation of the nail is realized using CO_2 and erbium lasers [12, 13]. The radiation of erbium lasers is effectively absorbed by water containing in nail plate and α-keratin which is the main component of the nail [14]. As a result of the transformation of absorbed laser energy to heat, a biological tissue is heated and ablated [13]. Compared to other methods of enhancing the drug penetration, including microneedling and microdermabrasion, laser drug delivery (LADD) through microporation of the nail

demonstrates greater safety, convenience, and effectiveness [15].

The delivery of drugs to the microporated nail plate can be passive or active, that is, it can occur without or as a result of any external influence. With passive delivery, water-based drugs do not penetrate through the microporated nail plate to the nail bed due to the high coefficient of surface tension [16]. With active delivery, external influences, for example, laser-induced hydrodynamic processes, can stimulate delivery and increase the rate of drug penetration [17]. The choice of a laser source for delivery is essential. It is important to exclude the possibility of changing the properties of the drug under the action of laser radiation. In this regard optimal is the impact not on the drug itself, but on the substance in which it is dissolved. It is known that the Er:YLF laser has a wavelength of 2.81 μm and is very effectively absorbed by water [18]. The high value of Er:YLF laser radiation absorption in water provides effective heating and transformation of the laser energy into mechanical energy, which is expressed in the generation of acoustic waves leading to the delivery of drug dissolved in water. In this case, the laser radiation acts on water and not on the drug, excluding the transformation of the latter as a result of the direct action of light. Active laser delivery methods are constantly being improved, for example, in articles [19–21], the capabilities of a new double-stage active laser drug delivery (DSLADD) method are discussed and demonstrated *in vitro* for the first time. DSLADD includes nail microporation using Er:YLF laser radiation through the layer of drug applied to the nail surface and subsequent exposure of this layer to the radiation of the same laser to deliver the drug under the already microporated nail plate. It is obvious that *in vivo* the effectiveness of DSLADD may differ from that *in vitro* due to the anatomically tighter connection of the nail to the underlying tissues *in vivo*. Thus, testing DSLADDs *in vivo* is an actual task.

The peculiarity of the current level of development of technologies for the drug delivery through a microporated nail is that its rate is difficult to predict. This is a serious limitation for the widespread use of the microporation method in clinical practice. An important characteristic that determines the drug delivery after nail microporation is the coefficient of drug penetration through such a nail plate. Obviously, the coefficient of drug penetration when using microporation to improve local drug delivery depends on both the properties of the nail plate and the filling density and the dimensions of the microholes (micropores).

There is a known mathematical model that makes it possible to estimate the rate of drug delivery through microporated skin [22]. This model leads to a relatively simple equation of skin resistance and demonstrates that the approach based on the calculation of the flow proportional to the total perimeter of the microhole predicts significantly higher flows than the approach based on the calculation of the flow proportional to the area of a microhole. The results of calculations based on this model were in good agreement with the experimental data on drug delivery to the skin presented in the literature [23–25]. However, the model assumes that the drug instantly penetrates into the microhole, which is not entirely true for microholes with small dimensions (radius) where capillary effects are present. In addition, this model assumes that the stratum corneum of the skin is completely impervious to topical drugs and thus does not take into account the diffusion of the drug in the skin. Thus, for an adequate description and optimization of the process of local drugs delivery under the nail plate, it is relevant to create a mathematical model to assess the rate of drug penetration through a microporated nail plate, which takes into account the contribution of capillary effects and drug diffusion in the nail plate.

The aim of this study was (1) to investigate of DSLADD of an aqueous solution of methylene blue using Er:YLF laser radiation experimentally, (2) to develop a model for the delivery of local drugs under a microporated nail plate taking into account laser radiation influence on the process of the drug delivery through the micropores in the nail plate created by the laser radiation, capillary effects in microholes and diffusion in the nail plate, (3) to estimate the coefficient permeability of a microporated nail plate for an aqueous solution of methylene blue using this model, and (4) to compare the simulation and experimental results.

2 Materials and Methods

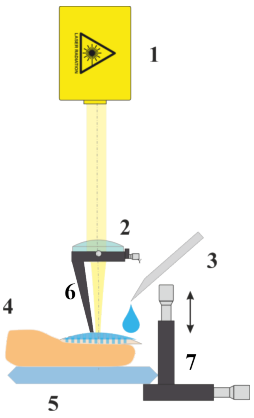
2.1 Experimental Setup for Investigate of DSLADD of a Methylene Blue Aqueous Solution Using Er:YLF Laser Radiation

In an *in vivo* experiment, the distribution of methylene blue (MB) under the nail plate after DSLADD was investigated. For active delivery of MB, an Er:YLF laser radiation ($\lambda = 2.81$ μm) was used. The study used a healthy nail of finger of one volunteer, which was mechanically cleaned of dirt and washed with distilled water before the experiments. The average thickness of the nail plate measured along the free edge of the nail was 365 ± 20 μm. The scheme of experimental setup and the appearance of the experiment are shown in Fig. 1.

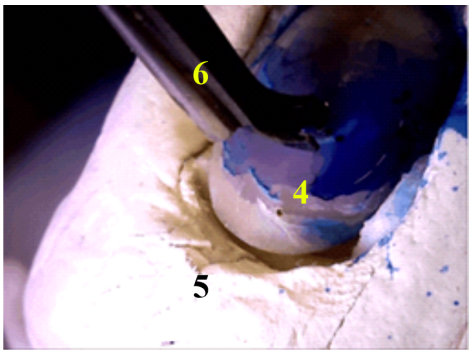
First, according to recommendation of Ref. [19] a microhole was created in the nail plate as a result of *in vivo* exposure the volunteer's nail to ten Er:YLF laser pulses through a layer of aqueous MB solution ($C = 0.001\%$) with a thickness of $h = 100 \pm 10$ μm applied to the nail surface. Laser pulse energy was $E = 4 \pm 0.1$ mJ, and the pulse repetition rate was $f = 30$ Hz. Then, active laser delivery of MB was carried out as a result of exposure the same MB layer to four Er:YLF laser pulses with the same radiation parameters as for microporation. Thus, 14 laser pulses were used for DSLADD through a single microhole. In total, in the experiment, ten microholes located at a distance of about 1 mm from each other were created and analyzed.

After DSLAAD, the appearance of the nail with the results of active laser delivery was recorded using a

microscope “Axio Scope A1” (“Carl Zeiss”, Germany) with a camera “Axiocam ERc 5s” (“Carl Zeiss”, Germany).



(a)



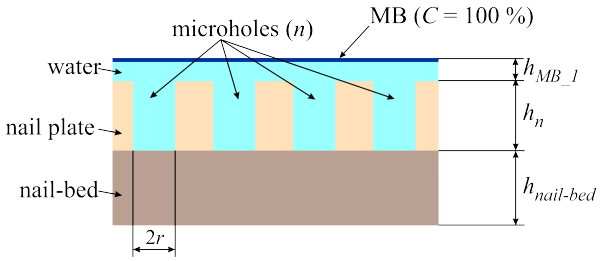
(b)

Fig. 1 Scheme of experimental setup (a) and appearance of the *in vivo* experiment (b) on DSLADD of MB solution using Er:YLF radiation: 1 – Er:YLF laser; 2 – collecting lens (F = 50 mm), 3 – injection needle with MB solution; 4 – volunteer’s finger; 5 – finger fixing device, 6 – focal plane fixator, 7 – XYZ-translator.

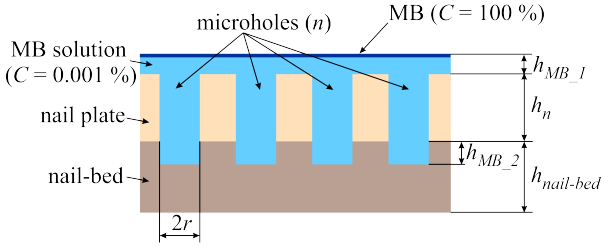
In the course of the study, it was found that with *in vivo* active Er:YLF laser delivery of MB, the effect of laser radiation on the drug leads to its spreading along the surface of the nail bed, i.e. to the fact that it is distributed in the nail bed not only in the area of the nail bed located under the microhole, but also along the border of the nail plate and the nail bed around the microhole. To assess this phenomenon from photographs, the diameter d_{MB} of the area of the nail bed containing MB and the diameter d of the microhole in the nail plate were measured in the “CorelDRAW Graphics Suite” (“Corel”, Canada) software.

2.2 Theoretical Model for the Delivery of Local Drugs under a Microporated Nail Plate

When creating a model describing the process of drug (MB) penetration under a micropore nail, it was assumed that after laser microporation, cylindrical microholes (with a radius of r) are formed in the nail plate, which reach the nail bed. The structural model of a microporated nail illustrating its state before and after drug (MB) penetration into the nail bed is shown in Fig. 2. It is assumed that the microholes are located at equal distances from each other and form a certain density of filling the area of the nail with microholes n_p (number of microholes per cm^2). The concentration of the applied drug (MB) is kept constant and equal to 100 % at a distance of h_{MB_1} = 100 μm above the nail plate. The penetration of the drug to a depth of h_{MB_2} = 100 μm is determined by the diffusion of the drug into the nail bed (nail epidermis). After diffusion, the concentration of drug (MB) in the aqueous solution becomes 0.001%.



(a)



(b)

Fig. 2 Structural model of a microporated nail to describe passive drug (MB) delivery through the nail plate – before (a) and after (b) delivery of drug (MB) through microholes.

We assume that the flow of the drug through the microporated nail plate will be equal to the sum of the flow through the microholes and the flow through the intact nail plate. In addition, the model takes into account the spreading mentioned above (see Section 2.1) of the MB under the nail plate caused by hydrodynamic processes during DSLADD. In this regard, we believe that with such spreading of the drug, the complete filling of the area under the nail plate with the drug, which is obviously necessary for the effective treatment of fungal disease, can be achieved with a smaller number of microholes in the nail plate than without spreading. However, this assumption has not been previously investigated.

According to Ref. [22], for an intact nail plate, the coefficient of drug penetration through the nail bed is defined as:

$$K_{p_o} = \frac{1}{R_0} = 0, \quad (1)$$

where R_0 is the diffusion resistance to the drug penetration through the intact nail plate and the nail bed.

In the absence of a nail plate, the permeability coefficient of the drug through the nail bed is determined as [22]:

$$k_{p_no_nail} = \frac{1}{R_{no_nail}} = \left(\frac{h_{MB_1}}{D_{drug}} + \frac{h_{MB_2}}{K_s \times D_{nail-bed}} \right)^{-1}, \quad (2)$$

where D_{MB} is a coefficient of drug (MB) diffusion in a layer of water with a thickness of 100 μm located on the surface of the nail, $D_{nail\text{-}bed}$ is a coefficient of drug diffusion in the nail bed, K_s is distribution coefficient characterizing the change in the concentration of the drug at the border between the nail bed and water, R_{no_nail} is diffusion resistance to the penetration of the drug through the nail bed, h_{MB_1} is the thickness of the applied drug (methylene blue) in the form of an aqueous solution over the nail plate, h_{MB_2} is the depth of the drug penetration into the nail bed.

Considering the model developed for the skin and presented in Ref. [22], under the assumption that the delivered drug (MB) instantly penetrates into the microhole, and the stratum corneum is completely impervious to local drugs, and replacing the skin model with a nail model (see Fig. 2), we find that the coefficient of drug permeability through the microporated nail and nail bed can be determined as:

$$k_{p_no_tr} = \frac{1}{R_{no_tr}} = 4n_p \times r \times \times \left((1 + \frac{4h_n}{\pi r}) \times \frac{1}{D_{MB}} + \frac{1}{K_s \times D_{nail-bed}} \right)^{-1}, \quad (3)$$

where D_{drug} is a coefficient of drug (MB) diffusion in a layer of water with a thickness of 100 μm located on the surface of the nail and in a microhole initially filled with water, $D_{nail\text{-}bed}$ is a coefficient of drug diffusion in the nail bed, K_s is distribution coefficient characterizing the change in the concentration of the drug at the border between the nail bed and water in microhole, R_{no_tr} is diffusion resistance to the penetration of the drug through the microporated nail and the nail bed, on the assumption that the aqueous solution of drug (MB) instantly penetrates into the microhole and the nail is completely impervious to local drugs, h_n is the thickness of the nail plate, r is the microhole radius, n_p is the density of filling the nail area with microholes.

Considering the model presented in Ref. [22], in the case of the skin, it is assumed that the water into which the drug diffuses instantly penetrates the micropore, and also that the stratum corneum is completely impervious to topical drugs. Therefore, in case of the nail, diffusion of the drugs in the nail plate also is not taken into account. At the same time, the coefficient of permeability of the drug through the nail plate k_{p_nail} depends on the molecular weight MW of the drug as follows [4]:

$$k_{p_nail} = 10^{(-3.11-1.75\times\log(MW))}. \quad (4)$$

In case of MB molecular weight MW = 319 Da [26] and $k_{p_nail} = 3.224\times10^{-8}$ cm/s.

In addition, in Ref. [22], it is assumed that initially the microholes are filled with water and not air, as is usually the case after microporation. Consequently, capillary effects arising at the interface between the solid (nail plate), liquid (water) and gaseous (air in the microholes in the nail plate) phases are not taken into account. At the same time, the movement of liquid in micro-holes with a small radius depends on the surface tension force. With a high coefficient of surface tension, water-based drugs do not penetrate into microholes due to the resistance caused by surface tension forces Δp_σ, which can be estimated by the formula [27]:

$$\Delta p_\sigma = \frac{4\sigma}{d}, \quad (5)$$

where σ is the coefficient of surface tension, $d = 2r$ is the diameter of microhole.

Taking to account the Eq. (5), speed of steady liquid flow $\Delta v = \sqrt{\frac{4\sigma}{\rho r}}$ [28] and nail plate thickness h_n, the resistance R_{CE}, caused by only the forces of the surface tension can be defined as

$$R_{CE} = h_n \times \Delta v = h_n \times \sqrt{\frac{2\Delta p_\sigma}{\rho}} = h_n \times \sqrt{\frac{4\sigma}{\rho r}}. \quad (6)$$

Since the studied MB aqueous solution has a low concentration ($C = 0.001\%$), in calculations it can be assumed that the surface tension of the MB solution at the interface with air in microholes is equal to the surface tension of water at the interface with air in microholes: $\sigma = 72.86\times10^{-3}$ N/m (at temperature T = 20 °C) [29], and the density of aqueous solution of MB is assumed to be equal to density of water $\rho = 997$ kg/m^3.

The coefficient of drug permeability through a microporated nail plate and nail bed, taking into account R_{no_tr} (3) and R_{CE} (6) is determined as:

$$k_{p_with_CE} = \frac{1}{R_{with_CE}} = 4n_p r \times \times \left((1 + \frac{4h_n}{\pi r}) \times \frac{1}{D_{MB}} + \frac{1}{K_S \times D_{nail-bed}} + \frac{1}{h_n \sqrt{\frac{4\sigma}{\rho r}}} \right)^{-1}, \quad (7)$$

where r is the radius of the microhole, R_{with_CE} is the diffusion resistance to the penetration of the drug through the microporated nail and the nail bed considering capillary effects.

The permeability coefficient of the drug through the microporated nail plate and the nail bed considering capillary effects and the coefficient nail plate permeability is determined as:

$$k_p = \frac{1}{R} = 4n_p r \times \left((1+\frac{4h_n}{\pi r}) \times \frac{1}{D_{MB}} + \frac{1}{K_S \times D_{nail-bed}} + \frac{1}{h_n \sqrt{\frac{4\sigma}{\rho r}}} \right)^{-1} + \left(1 - n_p \pi r^2\right) \times k_{p_nail}. \quad (8)$$

The coefficient $1 - n_p \pi r^2$ allows to consider the diffusion only through the part of the nail plate, which does not have micropores. In the absence of micropores ($n_p = 0$), this coefficient is equal to 1, and the permeability coefficient $k_p = k_{p_nail}$. With the maximum possible density of filling the surface of the nail plate with micropores without overlapping, $n_p = n_{p\ max} = 1/(2r)^2$, and k_p reaches the maximum value in this case.

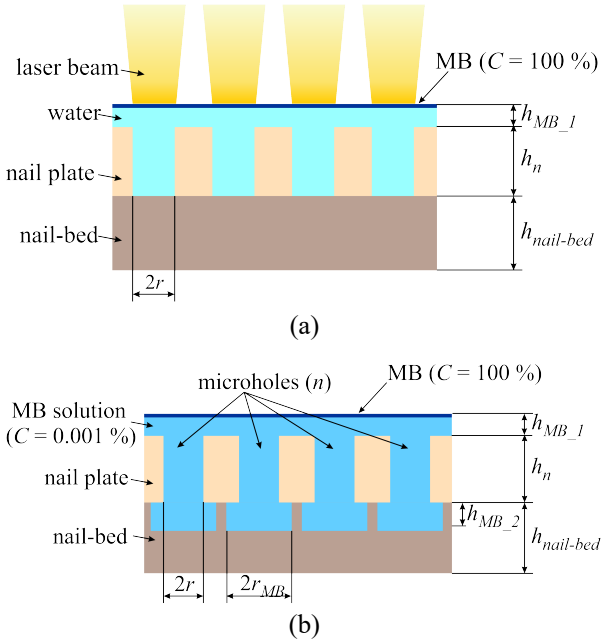


Fig. 3 Structural model of a microporated nail to describe active drug delivery (MB) through the nail plate – before (a) and after (b) delivery of drug (MB) through microholes.

To overcome the resistance caused by the forces of surface tension, laser radiation can be used. It stimulates the acoustic waves and pressure, which can be much greater than the forces of hydraulic resistance. As noted above (see Section 2.1), during *in vivo* active Er:YLF laser delivery of MB, the action of laser radiation on the drug leads to spreading of the drug, i.e. it is distributed in the nail bed not only in the area of the nail bed located directly under the microhole, but also along the border of the nail plate and the nail bed around the microhole (see Fig. 3 (a, b)). To take into account the contribution of this phenomenon to the area from which diffusion into the nail bed occurs, we used the drug distribution coefficient k_d, which is defined as the ratio of the diameter $d_{MB} = 2r_{MB}$ (where r_{MB} is the radius of the nail bed area under the nail plate containing the delivered drug) to the diameter of microhole in the nail plate $d = 2r$ (see Fig. 3b).

The spreading effect of is associated with the action of laser radiation only on the drug in the microholes and therefore does not affect the drug diffusion through the part of the nail plate, which does not have micropores. In this regard, the contribution of the drug distribution coefficient k_d should be taken into account only in the first term of Eq. (8) associated with $k_{p_with_CE}$.

Based on the foregoing, the coefficient of the drug permeability through the laser-microporated nail plate into the nail bed, taking into account capillary effects, the permeability coefficient of the nail plate k_{p_nail} and the drug distribution coefficient k_d, is determined as:

$$k_{p_\Sigma} = \frac{1}{R_\Sigma} = 4n_p r k_d \times \left((1+\frac{4h_n}{\pi r}) \times \frac{1}{D_{MB}} + \frac{1}{K_S \times D_{nail-bed}} + \frac{1}{h_n \sqrt{\frac{4\sigma}{\rho r}}} \right)^{-1} + \left(1 - n_p \pi r^2\right) \times k_{p_nail}, \quad (9)$$

where R_Σ is the diffusion resistance to the penetration of the drug through the microporated nail and the nail bed, taking into account capillary effects, the coefficient of permeability of the nail plate and the coefficient of distribution of the drug.

For the subsequent modeling, the following coefficients were taken: $D_{MB} = 0.38 \cdot 10^{-5}$ cm^2/s [41], diffusion coefficient of the drug (MB) in the nail bed $D_{nail-bed} = 1.98 \cdot 10^{-6}$ cm^2/s [30], coefficient $K_s = 5.58$ [31].

3 Results and Discussion

3.1 Experimental Study of DSLADD of an Aqueous Solution of Methylene Blue Using Er:YLF Laser Radiation. Estimation of the Coefficient of Drug Distribution under the Nail Plate k_d.

In our study, methylene blue was used as the topical drug to be delivered under the nail plate. Methylene blue is a well-known antiseptic, has disinfecting and analgesic effect. The choice of this drug is also often due to the fact that it has a deep blue color and is well visualized. Usually in clinical practice, an aqueous or alcoholic solution of MB with a concentration of $C = 1$–3 % is used [32]. In some cases, including during photodynamic

therapy (PDT), the concentration of MB can be reduced [33]. Methylene blue is a widely used photosensitizer for PDT of fungal diseases [34]. It has a high redox potential and has an absorption maximum in the spectral range 550–700 nm [33]. In photodynamic therapy using MB, radiation is used that corresponds to its maximum absorption. It is known that the concentration of MB in water from the range $C = 0.001 \pm 0.01\%$ is most effective for the generation of singlet oxygen $_1O^2$ during antimicrobial photodynamic therapy with a diode laser with a wavelength of 660 nm [33]. At $C = 0.001\%$ in water, methylene blue is in the monomeric form [35]. It is known that the combined effect of an aqueous solution of MB with $C = 0.001\%$ and laser radiation with a wavelength of 662 nm on lactobacilli, Candida Albicans fungus, and Staphylococcus Aureus bacteria significantly reduces their colonies [36]. In our study, the concentration of MB in an aqueous solution is $C = 0.001\%$.

A typical appearance of the dorsal surface of the nail after an *in vivo* DSLAAD of methylene blue through a single microhole as a result of exposure to 14 pulses of Er:YLF laser radiation with an energy of 4 ± 0.1 mJ is shown in Fig. 4.

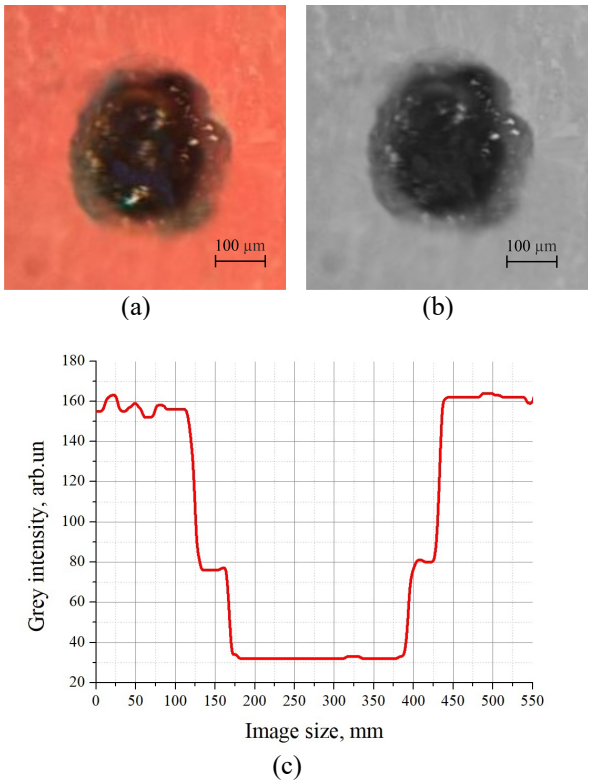


Fig. 4 (a) Typical color photo of a nail plate after an *in vivo* DSLAAD, (b) converted Gray image of the color photo shown in Fig. 4a6 and (c) the Gray intensity distribution along the diameter of the microhole shown in Fig. 4b.

During image processing, a color photograph of the nail plate (Fig. 4a) was converted into a Gray image (Fig. 4b). To estimate the diameter of the MB-containing area under the nail plate in this image, the Gray intensity (*GI*) distribution along the diameter of the microhole was analyzed (Fig. 4c). Gray intensity analysis was carried out using the "Mathcad 14" (PTC, Inc., Canada) software package, where intensity "0" is black and "255" is white. Gray intensity was measured in two mutually orthogonal directions and averaged over 10 photographs of the nail plate obtained after DSLAAD.

As a result of processing the entire array of photographs after DSLAAD, it was found that the image of a microhole in the nail plate corresponds to Gray intensity $GI = 32 \pm 11$. Thus, the average microhole diameter is 220 ± 10 μm, which coincides with the values presented earlier in Ref. [19]. The image of the intact nail plate has $GI = 160 \pm 10$, and the image of the area around the microhole containing the MB has $GI = 76 \pm 16$. Thus, the average diameter of the area of the nail bed under the nail plate containing the delivered drug (MB) is 312 ± 32 μm. Thus, in *in vivo* DSLAAD with Er:YLF laser radiation, the drug distribution coefficient is $k_d = 1.42 \pm 0.22$.

3.2 Theoretical Study of the Delivery of Local Drugs under Microporated Nail Plate

The results of modeling the coefficient of MB permeability through a laser-microporated nail plate into the nail bed depending on the area of microholes formed in the nail plate, obtained at various approximations described above for microhole diameter 220 μm and $k_d = 1.42$ are shown in Fig. 5.

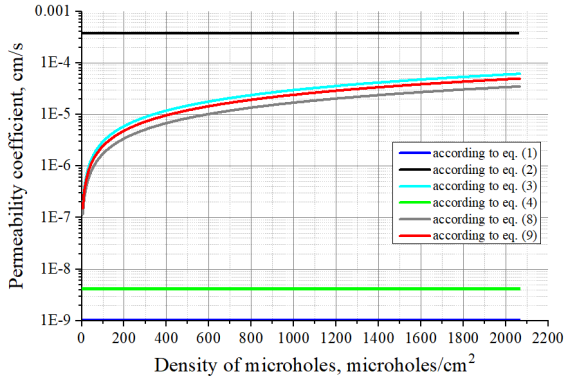


Fig. 5 Dependence of the permeability coefficient k_p on the density of filling the nail area with microholes n_p.

It can be seen that an intact nail plate has a minimum permeability coefficient, according to Eq. (4) (green line) $k_{p_nail} = 3.224 \times 10^{-8}$ cm/s. In the absence of a nail plate, the permeability coefficient, according to Eq. (2) (black line), is maximum and corresponds to $k_{p_no_nail} = 28.61 \times 10^{-5}$ cm/s.

With a microhole diameter of 220 μm, the maximum possible density of filling the nail area with microholes without overlapping of microholes corresponds to 2066 microholes/cm^2. It can be seen that, without taking into account capillary effects and the coefficient of permeability of the nail plate, the coefficient of permeability of the drug through the microporated nail plate and the nail bed, according to Eq. (3) (blue curve)

$k_{p_no_tr} = 6.15\times10^{-5}$ cm/s. The results of calculation the permeability coefficient of the drug taking into account capillary effects, according to Eq. (7), very close to results of calculation taking into account capillary effects and the coefficient nail plate permeability according to Eq. (8) (gray line). The value of the drug permeability coefficient, when taking into account capillary effects and the permeability coefficient of the nail plate, obtained according to Eq. (8) (gray curve) is $k_p = 3.506\times10^{-5}$ cm/s, which is 1.75 times less than the value of permeability coefficient obtained according to the Eq. (3). Obviously, this result is related to the resistance to the penetration of liquid into the microhole in the nail plate caused by the forces of surface tension and diffusion resistance to the penetration of the drug through the nail plate. In this case, the contribution of diffusion resistance to the penetration of the drug through the nail plate is insignificant in comparison with the contribution of the resistance to penetration of liquid into the microhole in the nail plate caused by surface tension forces.

The model, which takes into account the coefficient of distribution of the drug k_d in addition to capillary effects and the coefficient of permeability of the nail plate k_{p_nail}, increases the coefficient of permeability of the drug through the microporated nail plate and the nail bed by increasing the area on which the MB solution diffuses into the nail bed. In this case, with a filling density of 2066 microholes/cm^2 and $k_d = 1.42$, according to Eq. (9) (red curve), the permeability coefficient of the drug through the microporated nail plate and the nail bed increases by 1.42 times relative to the model that takes into account only capillary effects and the coefficient of permeability of the nail plates, and reaches $k_{p_\Sigma} = 4.978\times10^{-5}$ cm/s. This can be explained by the fact that since in this case the second term $(1 - n_p\pi r^2)\cdot k_{p_nail}$ in Eq. (9) is negligible, then the change in k_{p_Σ} is mainly determined by the drug distribution coefficient k_d. That is, due to the effect of drug spreading along the surface of the nail bed associated with the action of laser radiation during DSLAAD the density of filling the nail area with microholes can be significantly reduced (in this case, 1.42 times) without change in k_{p_Σ}, which can proportionally increase the productivity of laser delivery in general.

It should be noted that the values $k_{p_nail} = 3.224\times10^{-8}$ cm/s and $k_{p_\Sigma} = 4.978\times10^{-5}$ cm/s obtained in this work allow to conclude that the effect of Er:YLF laser radiation increases the permeability of the drug (MB) under the nail proportion to the ratio of these coefficients, i.e. 1544 times. It is known [37] that an effective photodynamic therapy of onychomycosis when applying the MB to the surface of a nail plate, which does not contain micropores, takes 8 sessions, separated by interval in 2 weeks (the duration of each session is 480 s including 180 s for drug application and 300 s for photodynamic irradiation). As a result, a significant reduction in the Onychomycosis Severity Index (OSI) was observed, and 70% of patients reached complete cure 12 weeks after the end of therapy. Thus, the laser microporation and delivery of MB under the nail plate by radiation of Er:YLF laser, taking into account the spreading effect, may allow to achieve a similar treatment effect, significantly reducing the duration of drug application to 0.12 s.

4 Conclusion

For the first time, the possibility of a two-stage active laser delivery of a photodynamic drug (MB) under the nail plate by Er:YLF laser radiation has been investigated and demonstrated *in vivo*. The distribution coefficient of the drug k_d was experimentally estimated, which is defined as the ratio of the diameter of the nail bed area under the nail plate containing the delivered drug to the diameter of the microhole in the nail plate. An original, relatively simple analytical model was developed to assess the permeability of a drug through a laser-microporated nail plate. The model considers the contribution of the drug spreading effect under the nail plate caused by effect of laser radiation on the drug during DSLADD and the resistance caused by surface tension forces. As a result of calculations within the framework of the developed model, it was found that for DSLAAD of an aqueous solution of MB with Er:YLF laser radiation with a laser pulse energy of 4 ± 0.1 mJ, the distribution coefficient is $k_d = 1.42 \pm 0.22$, and the density of filling the nail area with microholes is $n_p = 2066$ microholes/cm^2, and the permeability coefficient MB through the microporated nail plate and the nail bed reaches $k_{p_\Sigma} = 4.978\times10^{5}$ cm/s.

Disclosures

All authors declare that there is no conflict of interests in this paper.

Acknowledgements

The research was supported by Russian Science Foundation (project No. 22-25-00468).

References

1. C. C. Lai, C.-K.Tan. Y.-T. Huang, P.-L. Shao, and P.-R. Hsueh, "Current challenges in the management of invasive fungal infections," Journal of Infection and Chemotherapy 14(2), 77–85 (2008).
2. J. C. T. Wang, Y. Sun, "Human nail and its topical treatment: brief review of current research and development of topical antifungal drug delivery for onychomycosis treatment," Journal of Cosmetic Science 50(1), 71–76 (1999).

3. S. Murdan, "Drug delivery to the nail following topical application," International Journal of Pharmaceutics 236(1–2), 1–26 (2002).
4. S. M. Baswan, S. K. Li, and G. B. Kasting, "Diffusion of uncharged solutes through human nail plate," Pharmaceutical development and technology 21(2), 255–260 (2016).
5. A. K. Gupta, F. C. Simpson, "Investigational drugs for onychomycosis," Expert Opinion on Investigational Drugs 23(1), 97–106 (2014).
6. L. W. Figueiredo Souza, S. V. T. Souza, and A. C. C. Botelho, "Randomized controlled trial comparing photodynamic therapy based on methylene blue dye and fluconazole for toenail onychomycosis," Dermatologic Therapy 27(1), 43–47 (2014).
7. A. V. Belikov, Yu. V. Semyashkina, S. N. Smirnov, and A. D. Tavalinskaya, "Investigation of Changes in the Absorption Spectrum of Modern Chlorine-Containing Medicines for Photodynamic Therapy and Methylene Blue as a Result of Exposure to LED Emissions with a wavelength of 656±10 nm," Optics and Spectroscopy 128(7), 980–988 (2020).
8. V. Mathur, Y. Satrawala, and M. S. Rajput, "Physical and chemical penetration enhancers in transdermal drug delivery system," Asian Journal of Pharmaceutics 4(3), 173–183 (2010).
9. S. Mitragotri, J. Kost, "Low-frequency sonophoresis: a review," Advanced Drug Delivery Reviews 56(5), 589–601 (2004).
10. N. A. Monteiro-Riviere, A. O. Inman, and J. E. Riviere, "Identification of the Pathway of Iontophoretic Drug Delivery: Light and Ultrastructural Studies Using Mercuric Chloride in Pigs," Pharmaceutical Research 11(2), 251–256 (1994).
11. D. I. J. Morrow, P. A. McCarron, A. D. Woolfson, and R. F. Donnelly, "Innovative strategies for enhancing topical and transdermal drug delivery," The Open Drug Delivery Journal 1(1), 35–59 (2007).
12. M. T. Tsai, T.-Y. Tsai, S. C. Shen, C. Y. Ng, Y.-J. Lee, J.-D. Lee, and C.-H. Yang, "Evaluation of Laser-Assisted Trans-Nail Drug Delivery with Optical Coherence Tomography," Sensors 16(12), 2111 (2016).
13. J. Neev, J. S. Nelson, M. Critelli, J. L. McCullough, E. Cheung, W. A. Carrasco, A. M. Rubenchik, L. B. Da Silva, M. D. Perry, and B. C. Stuart, "Ablation of human nail by pulsed lasers," Lasers in Surgery and Medicine: The Official Journal of the American Society for Laser Medicine and Surgery 21(2), 186–192 (1997).
14. E. G. Bendit, "Infrared absorption spectrum of keratin. I. Spectra of α-, β-, and supercontracted keratin," Biopolymers: Original Research on Biomolecules 4(5), 539–559 (1966).
15. X. Chen, D. Shah, G. Kositratna, D. Manstein, R. R. Anderson, and M. X. Wu, "Facilitation of transcutaneous drug delivery and vaccine immunization by a safe laser technology," Journal of Controlled Release 159(1), 43–51 (2012).
16. A. V. Belikov, A. V. Skrypnik, A. N. Sergeev, S. N. Smirnov, and A. D. Tavalinskaya, "Er:YLF-laser microperforation of the nail plate for drug delivery," Proceedings of SPIE 10716, 107160X (2018).
17. D. F. Lyons, V. Le, G. L. Bidwell III, W. H. Kramer, E. A. Lewis, D. Raucher, and J. J. Correia, "Structural and hydrodynamic analysis of a novel drug delivery vector: ELP [$V_5G_3A_2$-150]," Biophysical Journal 104(9), 2009–2021 (2013).
18. G. Hale, M. Querry, "Optical constants of water in the 200nm to 200micron wavelength region," Applied Optics 12(3), 555 (1973).
19. A. V. Belikov, A. D. Tavalinskaya, and S. N. Smirnov, "Investigation of the Dual-Stage Method of Active Er:YLF Laser Drug Delivery Through the Nail and Laser-Induced Transformations of the Drug Extinction Spectrum," Lasers in Surgery and Medicine 53(8), 1122–1131 (2021).
20. A. V. Belikov, A. D. Tavalinskaya, S. N. Smirnov, and A. N. Sergeev, "Active Er-laser drug delivery using drug-impregnated gel for treatment of nail diseases," Biomedical Optics Express 10(7), 3232–3240 (2019).
21. A. V. Belikov, S. N. Smirnov, and A. D. Tavalinskaya, "Laser delivery and spectral study of a chlorin-containing drug for the treatment of onychomycosis with sequential laser (λ = 2819 nm) and photodynamic (λ = 656 ± 10 nm) exposure," Optics and Spectroscopy 129(6), 698–706 (2021).
22. A. S. Rzhevskiy, R. H. Guy, and Y. G. Anissimov, "Modelling drug flux through microporated skin," Journal of Controlled Release 241, 194–199 (2016).
23. G. Yan, K. S.Warner, J. Zhang, S. Sharma, and B. K. Gale, "Evaluation needle length and density of microneedle arrays in the pretreatment of skin for transdermal drug delivery," International Journal of Pharmaceutics 391(1–2), 7–12 (2010).
24. S. Zhang, Y. Qiu, and Y. Gao, "Enhanced delivery of hydrophilic peptides in vitro by transdermal microneedle pretreatment," Acta Pharmaceutica Sinica B 4(1), 100–104 (2014).
25. Y. Bachhav, S. Summer, A. Heinrich, T. Bragagna, C. Böhler, and Y. N. Kali, "Effect of controlled laser microporation on drug transport kinetics into and across the skin," Journal of Controlled Release 146(1), 31 – 36(2010).
26. A. K. Saikia, S. Aggarwal, and U. K. Mandal, "Electrically induced swelling and methylene blue release behaviour of poly (N-isopropylacrylamide-co-acrylamido-2-methylpropyl sulphonic acid) hydrogels," Colloid and Polymer Science 293(12), 3533–3544 (2015).

27. K. F. Pavlov, P. G. Romanov, and A. A. Noskov, Examples and tasks in the course of processes and apparatuses of chemical technology, Ripol Classic, Moscow (1987) [in Russian].
28. G. V. Taranenko, "Calculation of the hydraulic resistance of failure-type trays in the mode of a moving gas-liquid layer," ScienceRise 6(2), 23 (2016) [in Russian].
29. M. V. Masterov, M. W. Baltussen, and J. A. M. Kuipers, "Influence of the free surface on hydrodynamics in a bubble column," Chemical Engineering Science: X 8,100077 (2020)
30. E. A. Basco, M. V. Klement'eva, A. N. Bashkatov, V. V. Tuchin, and E. A. Genina, "Diffusion of methylene blue into rat skin ex vivo," Problemy opticheskoy fiziki i biofotoniki. SFM-2017 47 (2017) [in Russian]. ISBN 978-5-98116-224-4.
31. S. Mishra, P. Kumar, "Attenuation of methylene blue dye during riverbank filtration through sandy aquifers," Water and Environment Journal 29(4), 507–514 (2015).
32. I. I. Jack Clifton, J. B. Leikin, "Methylene blue," American Journal of Therapeutics 10(4), 289–291 (2003).
33. C. Komine, Y. Tsujimoto, "A small amount of singlet oxygen generated via excited methylene blue by photodynamic therapy induces the sterilization of Enterococcus faecalis," Journal of Endodontics 39(3), 411–414 (2013).
34. L. W. F. Souza, S. V. T. Souza, and A. C. de C. Botelho, "Distal and lateral toenail onychomycosis caused by Trichophyton rubrum: treatment with photodynamic therapy based on methylene blue dye," Anais Brasileiros de Dermatologia 89(1), 184–186 (2014).
35. W. Spencer, J. R. Sutter, "Kinetic study of the monomer-dimer equilibrium of methylene blue in aqueous solution," Journal of Physical Chemistry 83(12), 1573–1576 (1979).
36. A. A. Selifonov, O. G. Shapoval, A. N. Mikerov, and V. V. Tuchin, "Determination of the diffusion coefficient of methylene blue solutions in dentin of a human tooth using reflectance spectroscopy and their antibacterial activity during laser exposure," Optics and Spectroscopy 126(6), 758–768 (2019).
37. E. Alberdi, C. Gomez, "Efficiency of methylene blue-mediated photodynamic therapy vs intense pulsed light in the treatment of onychomycosis in the toenails," Photodermatology, Photoimmunology & Photomedicine 35(2), 69–77 (2019).